Detecting anaerobic methane oxidation coupled to sulfate reduction in hydrothermal sediments

Master thesis in Earth Sciences

Karen Elisabeth Moltubakk

Department of Earth Science

University of Bergen, March 2022

Abstract

The barite field is a low-temperature vent field, characterized by microbial activity and high fluid values of NH_4, SO_4^{2-}, and CH_4. Geochemical analysis indicates a hydrothermal system with a sedimentary input from the Bear Island Fan that has affected the high-temperature fluids. The diluted version of the high-temperature fluids mixes with a seawater input in the barite field. The mixture intensifies the CH_4 (4nM) production, and when meeting with SO_4^{2-} (28.29 μM) produces high values of H_2S (15.71μM). The barite field offers a unique opportunity to study the AOM-SR in hydrothermal sediments with high production of CH_4 and high concentration of seawater SO_4^{2-} circulation the sediments, and the temperature (20°C) makes it habitable for microorganisms to thrive. The microbial mats consume the oxygen available on the surface sediments; barely any oxygen enters the top sediments, making the sediments in the barite field suboxic and anoxic. The anoxic environment is perfect for the anaerobic methanotrophic archaea ANME since oxygen is toxic for the ANIME. One gravity core and one blade core were sampled in 2014 and 2018, respectively. The SEM pictures display high abundances of framboidal pyrite from the blade core and pyrite octahedrons in the gravity core. The geochemistry from the barite field shows fluctuating CH_4, TOC, and H_2S values indicating that AOM-SR can occur in several sediment horizons. The SO_4^{2-} concentration remains stable through the sediment core, indicating a potential flux of SO_4^{2-} to the sediments. The sulfur isotopes indicate a biogenic origin of the isotopes related to the sediment core. Different sulfate reduction rates lead to more positive values in the blade core with the highest rates. The iron isotopes present a wide range of values from negative to positive for both cores. They indicate an iron limitation in several of the sediment horizons and, for the first time, identify AOM-SR in hydrothermal sediments.

Acknowledgements

I want to thank my wonderful supervisor Desiree Lisette Roerdink for always helping and being available. Thank you for being positive and encouraging. I would also like to thank my co-supervisors, Francesca Vulcano, Ida Steen, and Harald Strauss. An extra thank you to Vulcano for teaching me about microorganisms. I would also like to thank Hildegunn Almelid, Yuval Ronen, Siv Hjorth Dundas, and Irene Heggstad for lab-work assistance, SEM analyses, and geochemical analyses.

Thank you to Lotte Hammer Johannessen, Marie Wold, and Anne-Sofie Ertesvåg for making my five years at the UiB fun and memorable. Thank you for the lunch breaks and the motivation you all have given me. Special thanks to my friend at the "Black Smoker" student office.

Thank you so much to my international friends who proofread my thesis, Hannah Kura Knight, Megan Ruth Babin, and Samuel Truscott. I would also like to thank Kristian Agasøster Haaga for proofreading.

Thank you so much, Ingrid Hornnes, for not only helping me with the biology aspect and proofreading. Also, for always being positive and lessening my stress. Thank you, Gro Nordskog, for being the best roommate, making dinners, and playing video games with me when I needed a break. A huge thank you to my non-geo friends, Rikke Marie Kvalvik, Marie Hepsøe Torpe, Sunisa Somsri and especially my boyfriend Birk Hjellegjerde. Thank you all for always being excited and curious about my thesis, despite it being a foreign topic. Finally, thank you to my family for being my biggest fans and continuously checking in on me and my well-being.

Contents

1 Introduction

Marine sediments are the largest methane reservoir and the major sink of methane. Most of the methane produced is oxidized in the upper layers of the sediment it reaches the hydrosphere. Approximately 90% of the methane produced is oxidized by anaerobic oxidation of methane (AOM) (Lin et al., 2016a; Cassarini, 2017; Turchyn et al., 2018). Methane is an essential and potent greenhouse gas affecting the global environment. It might have been one of the main causes of environmental changes in the past (Lin et al., 2016a; Crémière et al., 2020). Studying the processes involving methane in the sediments can improve the understanding of past environments and predict future changes. To widen the knowledge of methane, it is crucial to study the areas where methane is produced. Methane is produced in marine sediments by methanogenic degradation of organic matter buried in anoxic deep-sea sediments (Eickmann et al., 2020; Crémière et al., 2020). The AOM is restricted to anoxic environments and is usually in the sulfate-methane transition zone (SMTZ).

SMTZ is characterized by low concentrations of methane and sulfate and high concentrations of sulfide. The SMTZ is a depth interval where most of the methane and sulfate is consumed by a consortium of methanotrophic archaea and sulfate-reducing bacteria (Lin et al., 2016a; Crémière et al., 2020). The two main groups for the methanotrophic archaea and sulfate-reducing bacteria are ANME and Deltaproteobacteria (Knittel and Boetius, 2009; Lin et al., 2016a; Crémière et al., 2020). The AOM-SR process was considered an abiological process for a long time, as the energy gain was too low to sustain life. However, the theory was debunked after discovering the methane-oxidizing group named ANME. The ANME oxidizes methane together with their sulfate-reducing partner, and the energy gain related to AOM reaction is ΔG° $-16 kJmol^{-1}$ in room temperature $25^{\circ}C$. The energy produced from the AOM-SR reaction is shared between ANME and SRB. The AOM-SR produces sulfide; the sulfide reacts with iron to form iron sulfide, which is metastable and eventually converted to pyrite.

The thesis's main aim will be to assess whether sulfur and iron isotopes can be used as tracers for the AOM-SR reaction in hydrothermal sediments, for the present and past reactions. Pyrite is used as a tracer for modern and ancient sediments since the isotope signature is mainly preserved from the conversion of H_2S and dissolved Fe to pyrite, meaning it works as an excellent tracer (Lin et al., 2016b; Severmann et al., 2006). The biological fractionation of isotopes is different from abiological fractionation; hence it is possible to track past reactions caused by microorganisms. The primary method for sulfur isotopes is the chromium reduction method (CRS). The CRS method has been used to separate the sulfur isotopes in pyrite from other sulfide-bearing minerals. It is considered a robust method to use when wanting to extract sulfur isotopes from pyrite. On the other hand, only a handful of reports have used iron isotopes as a proxy for the AOM-SR reaction (Lin et al., 2016b).

The AOM-SR process can be detected by identifying the microorganisms present in the sediments. Finding AMNE in the sediments proves that the AOM-SR reaction occurs. However, it is impossible to use ANME to prove the AOM-SR reaction in ancient sediments since the ANME will no longer be active. Studies on marine sediments lead to several geochemical evidence of AOM-SR; the evidence is used to track paleo AOM-SR. However, no one has studied the AOM-SR in hydrothermal sediments. Marine sediments are usually not affected by different input sources of fluids, and the environment is stable regarding geochemical zones and microorganisms. However, that is not the case for hydrothermal systems, which often have seawater circulating with high-temperate fluids. The temperature in hydrothermal systems is also higher than in marine sediments, and the habitat in hydrothermal deposits is different from that in marine sediments.

The thesis will combine geochemcial evidence, microbial data, SEM, and isotopes to distinguish the different geochemical sediment reactions from the AOM-SR in the barite field. The results are compared to previous experiments from different deep-sea settings and studies from the barite field. The main aim of the thesis will be to find geochemical evidence for AOM-SR in hydrothermal systems by addressing how the following aspect affect each other:

- How the pyrite formation is in AOM-SR environments
- How the sediment and pore fluids influence the AOM-SR

- How the microbial community influence the AOM-SR

- Identify the sulfur and iron isotopes fractionation in AOM-SR affected sediments

- Look at the evidence used to distinguish the current AOM-SR from the paleo-AOM

2 Background

2.1 Sulfur cycle

Sulfur (S) is the sixteenth most abundant element in abundance and plays a key role in global biogeochemical cycles. S is redox-sensitive and abundant in all major reservoirs at Earth's surface; the biosphere, geosphere, and the hydrosphere (Stam, 2010; Canfield and Farquhar, 2012*b*). S is emitted into the reservoirs from the deeper mantle by volcanic or magmatic activity as sulfate (SO_2) or sulfide (H_2S). This sulfur is cycled at the Earth's surface between rocks, water and living organisms in three main pathways: 1) volcanic outgassing of SO_2 or H_2S, where the flux varies over time depending on volcanic intensity (Canfield and Farquhar, 2012*a*,*b*), 2) the release of H_2S from hydrothermal systems (Canfield and Farquhar, 2012*a*), and 3) weathering and leaching of S from rocks and sediments (Canfield and Farquhar, 2012*a*; Sievert et al., 2007). When exposed to oxygen, sulfide in the crust oxidize to sulfate (Canfield and Farquhar, 2012*a*), which is subsequently transported by rivers to the ocean where it accumulates and sinks to the ocean floor. Sulfate is an abundant anion in seawater and sediment pore fluids (28 mM), fueling biological sulfur cycling in the marine environment (Canfield and Thamdrup, 2009; Canfield and Farquhar, 2012*a*,*b*).

The biological sulfur cycle is different from the geological sulfur cycle, because the biological cycle encompasses the different organisms, such as Desulfobulbaceae and sulfur oxidizing bacteria (Steen et al., 2016; Eickmann et al., 2020). While the geological cycle determines the vectors between the different reservoirs (Canfield and Farquhar, 2012*a*,*b*). The biological sulfur cycle's starting point is sulfate, as sulfate is being consumed by various sulfate-reducing bacteria in the sediments, the processes is called "dissimilatory sulfate reduction" (DSR). Bottrell and Newton (2006) estimated the global DSR in sediments produced 300 $TgSa^{-1}$ of which 240 $TgSa^{-1}$is reoxidized and 60 $TgSa^{-1}$ is converted into pyrite. The sulfate reducers are either bacteria or archaea, they use sulfate as a terminal electron acceptor for respiration in anoxic environments, and organic carbon or H^+ as electro donor (Bick et al., 2000; Rickard, 2012). First, sulfate is activated by adenylation in a reaction catalyzed by ATP sulfurylase. The adenylation product 5´-adenylysulfate (APS), is reduced to sulfite, which is then further reduced to sulfide (fig.2.1) (Bick et al., 2000). S is used as both electron donor and electron acceptor, making S an element involved in many microbial metabolisms.

Some of the metabolisms are ancient and some contribute to the modern geochemical cycle (Bick et al., 2000; Canfield and Farquhar, 2012*b*).

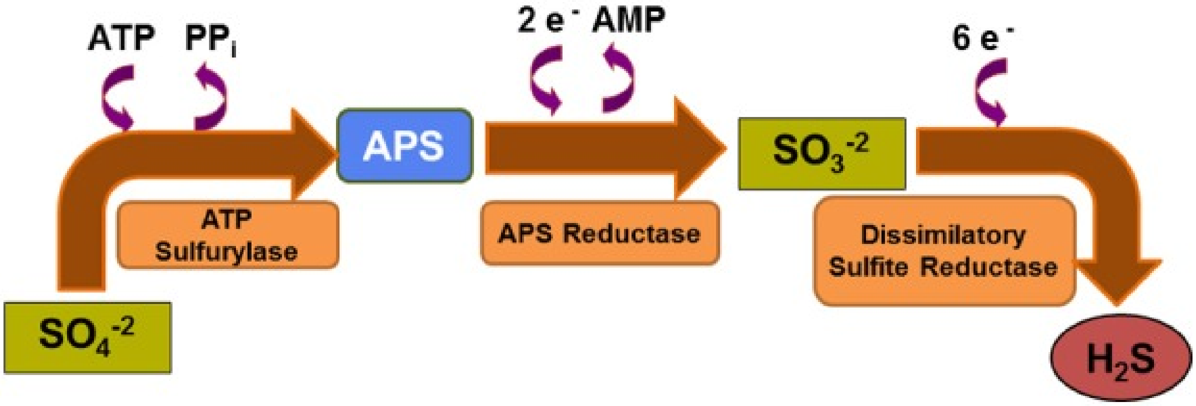

Figure 2.1: The dissimilatory sulfate reduction pathway, from sulfate to sulfide. Picture taken from Carbonero et al. (2012).

2.2 Sulfate reduction in deep-sea sediments

Microbial sulfate reduction occurs in deep-sea sediments at depths where thermodynamically more favorable electron donors of oxygen, nitrate, manganese and iron have become depleted (Canfield and Thamdrup, 2009). In this suboxic zone, sulfate reduction is typically coupled to the degradation of organic matter:

$$H^+ + SO_4^{2-} + C_2H_3O_2^- \longrightarrow H_2S + HCO_3^- \tag{1}$$

The zone is known as the "sulfate" zone, and H_2S accumulates in the pore water as a result. Below the sulfate zone, methanogenesis becomes the dominant pathway for organic matter degradation (Canfield and Thamdrup, 2009). The degradation generates methane which diffuses upward to the so-called sulfate-methane transition zone (SMTZ), where the methane can be oxidized anaerobically coupled to the reduction of sulfate (AOM-SR) (Canfield and Thamdrup, 2009; Lin et al., 2016a, 2017, 2016b). AOM-SR happens according to eq.2:

$$CH_4 + SO_4^{2-} \rightarrow HCO_2^- + HS^- + H_2 \tag{2}$$

The sulfate-reducing bacteria (SRB) and the methanotrophic archaea causes the AOM-SR that happens in the SMTZ. The SRB and methanotrophic archaea consumes CH_4 and SO_4^{2-} and the AOM-SR is the main processes behind the burial of S and Fe as pyrite in the deep-sea sediments (Rickard, 2012; Lin et al., 2016a). In the sediments H_2S is produced as a result of AOM-SR (eq.2). Dissolved Fe from pore fulids will react with H_2S. The reacting leads to the precipitation of monosulfide minerals or iron polysulfide minerals (3) (Sato et al., 2012; Lin et al., 2016a,b).

$$Fe^{2+} + H_2S \rightarrow FeS + 2H^- \tag{3}$$

The iron monosulfide minerals or iron polysulfide minerals are not stable in that mineral form and will convert into pyrite (Lin et al., 2016a; Sato et al., 2012). The conversion to pyrite can happen through two possible pathways, the first pathway is with elemental S (eq.4 and eq.5),

$$FeS + S^0_{\text{elemental sulfur}} \rightarrow FeS_2 \tag{4}$$

$$FeS + S^{2-}_{X\text{elemental sulfur}} \rightarrow FeS_2 \tag{5}$$

The second pathway is with dissolved H_2S which happens according to eq.6 (Lin et al., 2016a; Sato et al., 2012). The end product is the mineral pyrite, which can be used as a tracer for detecting AOM-SR in marine sediments.

$$FeS + H_2S_{\text{sulfide}} \rightarrow FeS_2 + H_2 \tag{6}$$

2.3 Detecting AOM-SR in marine sediments

AOM-SR is known for sulfide formation in the sediment (Lin et al., 2016a, 2017). Pore fluids profiles and microorganisms data can help with the detection of AOM-SR in marine sediments. CH_4, SO_4^{2-}, H_2S, Fe^{2+} and TOC are pore fluids affected by the AOM-SR process. The microorganisms ANME and Deltaproteobacteria (sulfate reducing bacteria) use CH_4 and SO_4^{2-}, and produces H_2S (Knittel and Boetius, 2009). During AOM-SR it is expected to detect an increase in H_2S concentrations, while TOC is used to produce methane, therefore the TOC content will decrease during AOM-SR (Lin et al., 2016a,b; Eickmann et al., 2020). Fe^{2+} is redox sensitive and no dissolved Fe^{2+} will accumulate in the presences of H_2S. Fe^{2+} and H_2S would react and form the mineral pyrite.

2.3.1 Pore fluid geochemistry

In deep-sea sediments several reactions occurs abiologically and biologically (fig.2.2) (Canfield and Thamdrup, 2009). The first reaction is between oxygen and electron donors, such as nitrogen, sulfur, and iron. Nitrate reduction will dominate after molecular oxygen is depleted from the sediments (fig.2.2). In deeper sediments the following reactions are manganese reduction, iron reduction, sulfate reduction, and lastly methanogenesis (Canfield and Thamdrup, 2009).

Sulfate reduction have two pathways, one being organiclastic sulfate reduction (OSR) (eq.7) and second being AOM-SR (eq.2). OSR have been considered as the main process behind sulfide formation, though studies such as Lin et al. (2016a, 2017) and have increased the understanding of AOM-SR. Results from Lin et al. (2016a, 2017) indicate that AOM-SR impacts the sulfide formation as much as OSR (Lin et al., 2017, 2016a). Consequently, separating the two diagenetic processes has become an increasingly important subject. Therefore, identifying the SMTZ is of importance, cause AOM-SR mainly happens in the SMTZ while OSR does not. The SMTZ is characterized by almost near-zero concentrations of sulfate and methane, and high values of dissolved H_2S (Lin et al., 2016a). The sulfate penetration depth can indicate how far into the sediments the SMTZ might occur, a shallow sulfate penetration depth means a shallow SMTZ and vise versa. The sulfate penetration depth varies roughly in proportion to the sulfate concentration, and the sulfate concentration changes with salinity (Jørgensen et al., 2004). The sulfate concentration is dependent on microorganism consuming sulfate and the flux of sulfate to the sediments. The SMTZ is also dependent on the methane flux upwards, and the methane concentration is dependent on the organic matter buried (Jørgensen et al., 2004). As sedimentary environment becomes more reducing the H_2S concentration will increase. However, the SMTZ would not exists if methane was not produced in the sediments underneath the sulfate reduction zone.

$$2CH_2O + SO_4^{2-} \rightarrow 2HCO_3^- + H_2S \tag{7}$$

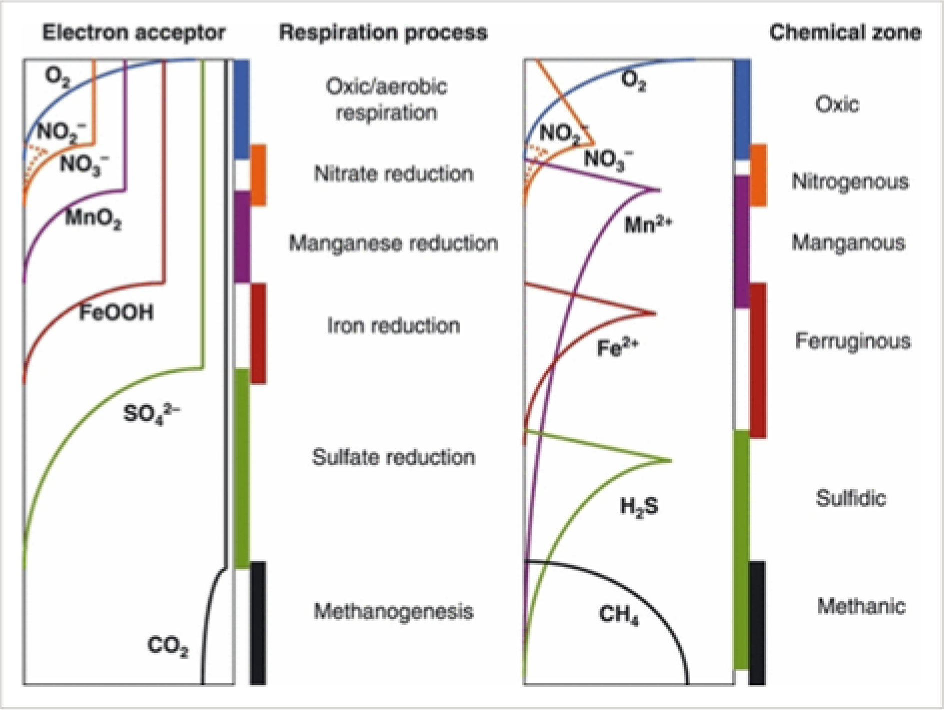

Figure 2.2: Left: illustration of electron acceptors through depth. Middle: the different respiration processes. Right: illustration of chemical zonation and the correlating chemical zones (Canfield and Thamdrup, 2009).

The last zone to occur in deep-sea sediments is the "methanic" zone where methane (CH_4) is the dominating compound, and where methanogenesis occurs (fig.2.2). Two main reaction pathways occur at the top of the "methanic zone": (1) the oxidation of CH_4 to methanol in the presence of molecular oxygen, and (2) in sulfate-rich systems the pore water SO_4^{2-} reacts with CH_4 and

AOM-SR occurs (fig.2.3) (Canfield and Thamdrup, 2009; Lin et al., 2017). In the sulfate-rich system AOM-SR is driven by consortium of microorganisms in the sediments, the two main groups are ANME and Deltaproteobacteria (sulfate reducing bacteria) (Knittel and Boetius, 2009). ANME and the sulfate reducing bacteria (SRB) are connected to each other, their cell aggregates are usually covered in an organic matrix (Knittel and Boetius, 2009). The ANME-1 and ANME-2 are associated to the Desulfosarcina and Desulfococcus (DSS), ANME-3 is associated with Desulfobulbus, and all of the SRB is from the branch Deltaproteobacteria (Knittel and Boetius, 2009). The Desulfobulbus is normally associated with the ANME-3, however DSS have also been identified with ANME-3 in shallow subsurface gas-hydrate sediments (Knittel and Boetius, 2009).

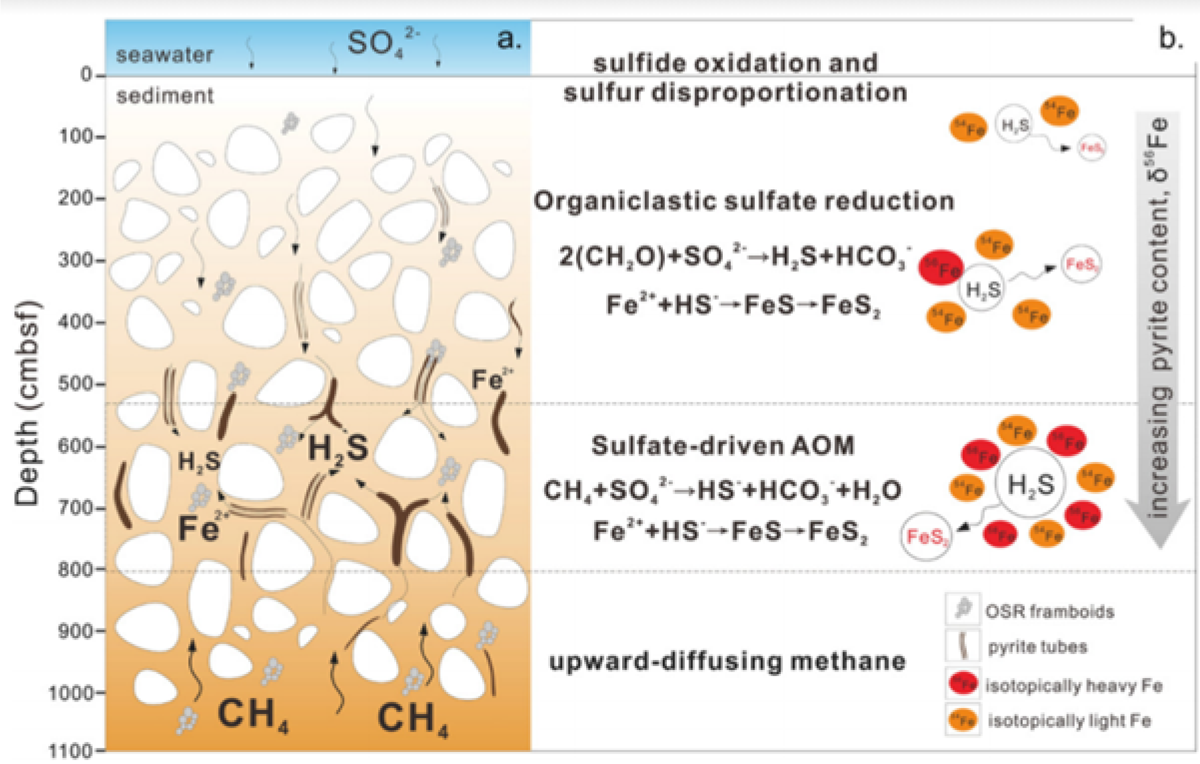

Figure 2.3: OSR and SO_4-AOM in the sediments (Lin et al., 2016a). Left: a drawing showing methane diffusing upward and sulfate diffusing downwards, eventually meeting and reacting with each other creating hydrogen sulfide and eventually pyrite. Right: the stoichiometry of the reactions

2.3.2 Stable sulfur isotopes

Stable isotope fractionation is the separation of heavy and light isotopes. Without fractionation all natural systems would lack variation in the distribution of isotopes (Fry, 2006; Tiwari et al., 2015; Canfield and Farquhar, 2012*b*). Stable isotopes can be separated into two groups: traditional isotopes and non-traditional isotopes. S has four stable isotopes, and they are considered as traditional stable isotope. Traditional stable isotopes have a skewed distribution on Earth, with 95% of the isotopes being light isotopes (Fry, 2006; Teng et al., 2017; Canfield and Farquhar, 2012*b*). Non-traditional isotopes include light isotopes Fe, Li, and M, and heavy isotopes Ti, and U. Non-traditional isotopes have unique geochemical features: 1) Most of them are trace elements, and their concentrations vary from different reservoirs, 2) They vary from highly volatile to refractory, 3) Many of them are redox-sensitive and biologically active, 4) Their bonding is different from the traditional stable isotopes, and 5) They often have more than two stable isotopes as they have high atomic numbers (Teng et al., 2017; Canfield and Farquhar, 2012*b*). S and Fe isotopes makes them prone to different fractionation mechanisms, making them peculiar traces for different processes (Teng et al., 2017; Canfield and Farquhar, 2012*b*),

S is a part of Group 16, and is referred to as the chalcogens (Rickard, 2012). The atomic number of S is 16, and the atomic weight is 32.066 (Rickard, 2012). The atomic weight is the average weight of terrestrial S and is based on S's four stable isotopes. The two most abundant stable isotopes are ^{32}S and ^{34}S with abundances on 92.02% and 4.21%, respectively. The last two are ^{33}S and ^{36}S with abundances on 0.75% and 0.02%, respectively. S also has one radioisotope called 35S with a half-life of 874 days. The $35S$ is commonly used to measure sulfate reduction rates (Rickard, 2012; Canfield and Farquhar, 2012*b*).

S has several valence states and the most abundant forms are sulfide, elemental S, and sulfate (Sievert et al., 2007; Canfield and Farquhar, 2012*b*). Sulfate is the most abundant ion in seawater, with a concentration of 29 mM (Cassarini, 2017). S has the ground state configuration referred to as the neon core. The reduction of two electrons will result in divalent S (or sulfide ion) (Rickard, 2012). The oxidation produces various oxidation numbers up to S(VI). A wide range of reduced and oxidation states are possible since the d-orbitals can be involved with the s- and p- orbitals in the bonding process. S- and p-orbitals make it possible to produce bonds in sulfate ions. The empty orbitals accept electrons from oxygen orbitals to create multiple bonds in sulfate (Rickard, 2012; Canfield and Farquhar, 2012*b*). This leads to a shortening of S-oxygen distance and the considerable chemical stability of the sulfate, making sulfate reduction a kinetically necessary process. The eight-electron addition of S(VI) to S (-II) is critical in sulfide biogeochemistry (Rickard, 2012; Canfield and Farquhar, 2012*b*).

The S isotopic signature is given as delta notation (δ), and the value is reported in parts per thousand (‰). ^{32}S is the most abundant isotope and is used as a reference point against the magnitude of fractionation of the other isotopes (Stam, 2010). The signature is calculated as the isotope ratio Variation between $^{3x}S/^{32}S$ of the sample relative to a standard (Rickard, 2012). The S isotopic composition is calculated as follows (eq.8):

$$\delta^{34}S = 1000 \times \frac{\frac{^{3x}S}{^{32}S}_{sample} - \frac{^{3x}S}{^{32}S}_{standard}}{\frac{^{3x}S}{^{32}S}_{standard}} \tag{8}$$

The standard is the Vienna Cañon Diablo meteorite from Meteor Crater in Arizona. The meteorite contains meteoritic S and represents Earth's bulk S (Stam, 2010; Rickard, 2012). The calculation of the S isotopic composition can be used as a tracer from different abiologically and biologically processes, and one of the common minerals to use is pyrite. Pyrite is the most common mineral in ancient and modern rocks. Sedimentary pyrite can be as old as 3.4 Ga or even older, making it an important tracer for early Earth (Rickard, 2012). The formation of pyrite in any sediment may have taken place over millions of years, even in areas with low sedimentation rates (Lin et al., 2016a).

Pyrite is an iron sulfide with the chemical formula FeS_2 (Stam, 2010; Raiswell and Canfield, 1998). Sulfide in sedimentary record will display $\delta^{34}S$ values that is generally lower than the respective $\delta^{34}S$ of the parental sulfate (Lin et al., 2016a; Jørgensen et al., 2004). When the $\delta^{34}S$ values are consumed by microorganism, the remaining isotopic sulfate pool will be enriched with heavier isotopes, as microorganism prefer the lighter isotopes. Therefore, negative $\delta^{34}S$ values in pyrite have been used as a proxy in both modern and ancient sediments when identifying biogenic origins (fig.2.4) (Lin et al., 2016a; Jørgensen et al., 2004). Borowski et al. (2013)'s studies displayed negative $\delta^{34}S$ values in pyrite and positive $\delta^{34}S$ values from the sulfate in pore fluids (Borowski et al., 2013; Lin et al., 2016a). Borowski et al. (2013) discovered slightly less negative $\delta^{34}S$ values from the sulfide minerals closer to the SMTZ, indicating that sulfide production was increasing and more of the sulfate was consumed. The change in $\delta^{34}S$ is used as a proxy when determining where the AOM-SR begins (Borowski et al., 2013; Lin et al., 2016a). The ANME and SSR prefers isotopically light S, therefore the sulfate in pore fluids will be depleted in isotopically light S and enriched in isotopically heavy S (Jørgensen et al., 2004). Models and experiments lead to various theories about the positive $\delta^{34}S$ values, one of them is Peketi et al. (2012) who observed that the ^{34}S enriched sulfide minerals increased in line with pyrite contents (Peketi et al., 2012). However, the pyrite content is also dependent on the flux of sulfate and methane.

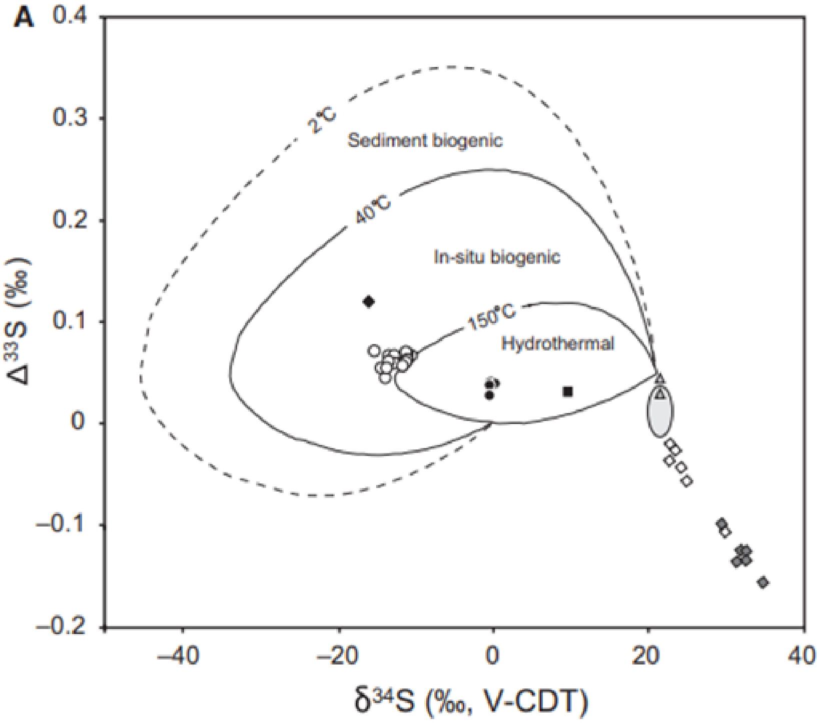

Figure 2.4: $\delta^{34}S$ vs $\Delta^{33}S$ in ‰, the illustration displays how the different isotopes values indicates different origins. Positive $\delta^{34}S$ and slightly negative $\Delta^{33}S$ values indicate hydrothermal activity, while negative $\delta^{34}S$ values display either in-suit biogenic or sediment biogenic origin. The $\Delta^{33}S$ values increase slightly from negative to positive values, from in-situ biogenic to sediment biogenic (Eickmann et al., 2014).

The methane flux will vary over time, and the variation leading to a vertical movement of the SMTZ. The movement generate multiple pyrite generations forming in the sediments at different depths and times, making it a unique tracer for past life (Lin et al., 2016a). Later formed pyrites tend to have heavier $\delta^{34}S$ values than earlier pyrite. It is suggested that the heavier $\delta^{34}S$ values are a result from sulfate reduction in a partly limited system where the later reactant sulfide become isotopically heavier as the lighter fraction is removed and sequestered in pyrite (Lin et al., 2016a). However, in sedimentary rocks, the problem lies with the possibility that late diagenesis happened, or groundwater influenced the S isotopic composition. Therefore, taking a bulk pyrite analysis potentially integrated the S isotopic composition of the sulfide in the sediment over a long time period (Lin et al., 2016a).

2.3.3 Coupled stable sulfur and iron isotopes

The formation of pyrite is dependent on sulfide and Fe available in the sediments. Studies about iron isotopes in pyrite will provide a deeper insight into the biogeochemcial cyle in the sediments (Lin et al., 2016b). Fe is a ubiquitous element with a rich chemical behavior, and can be found in the geosphere, hydrosphere, and biosphere. The atomic number of Fe is 26, and the atomic weight at 55.845(2), the 2 in brackets represents the uncertainty of the measurements (Rickard, 2012). Fe is made up of 31 isotopes. The 31 different iron isotopes, include four stable Fe isotopes, and 27 isotopes with short half-lives, the radioactive isotopes are less important in terrestrial samples. The four stable Fe isotopes consists of ^{54}Fe, ^{56}Fe, ^{57}Fe and ^{58}Fe. The ^{56}Fe has the highest relative abundance with 91.723%, ^{54}Fe with an abundance on 5.81%, ^{57}Fe, and ^{58}Fe with abundances on 2.21%, and 2.81%, respectively (Teng et al., 2017; Rickard, 2012). Only ^{54}Fe and^{57}Fe are of interest in biogeochemistry and for radioactive isotopes the ^{55}Fe and ^{59}Fe are of interest, which disintegrates into ^{55}Mn and ^{56}Co, respectively (Blain and Tagliabue, 2016). Fe's three oxidation states is related to the different isotopes.

Fe has three oxidation states; metallic iron Fe^{0}, ferrous iron Fe^{2+}, and ferric iron Fe^{3+}, the two and three electrons from the Fe atom are easily exchanged making it an important process of the understanding in Fe biogeochemistry (Teng et al., 2017; Blain and Tagliabue, 2016). The Fe being reduced to Fe^{2+} from Fe^{3+} often contains an isotopically lighter signature compared to the parent sources (Rickard, 2012; Severmann et al., 2006). Iron's nucleus consists of 26 protons and 30 neutrons, the binding forces between the protons and neutrons balance the compulsive behavior between protons, making it the most stable isotope in the universe (Blain and Tagliabue, 2016) The distribution of the different Fe oxidation states are markedly stratified, with metallic Fe in the core, ferrous Fe in the mantel and ferric Fe on the surface (Teng et al., 2017). Fe is the third most abundant metal in Earth's crust, despite mainly being concentrated in the core (Blain and Tagliabue, 2016).Fe reacts biologically and abiologically with the electron acceptors. The heterotrophic bacteria and archaea are responsible for most of the remineralization of organic carbon in marine sediments. This remineralization results in particulate Fe being dissolved (Blain and Tagliabue, 2016; Canfield and Thamdrup, 2009). Fe^{2+} is the dominating form of dissolved Fe in the marine sediments and redox reactions are common in the reducing environment (Blain and Tagliabue, 2016). The isotopic signature of Fe can be calculated following the same method as for S.

The isotopic composition of iron isotopes is reported as δ^{56}Fe, which is the deviation in ‰ of the ^{56}Fe/^{54}Fe ratio from a standard (Teng et al., 2017; Rickard, 2012). The reference material is arbitrary, and it is a metallic iron from the Institute for References Materials and Measurement in Belgium named IRMM-014 (Teng et al., 2017; Rickard, 2012). The Fe isotopic composition is calculated as follows:

$$\delta^{5x}Fe = \frac{^{5x}Fe}{^{54}Fe}_{sample} \frac{^{5x}Fe}{^{54}Fe}_{standard} - 1‰ \tag{9}$$

Were $\frac{^{5x}Fe}{^{54}Fe}_{standard}$ is the isotopic ratio of IRMM-014 and $\frac{^{5x}Fe}{54Fe}_{sample}$ is the sample used for the analyses. $\delta^{58}Fe$ is usually never reported as it is related to $\delta^{56}Fe$ through mass dependent fractionation, while $\delta^{57}Fe$ is almost always reported as it ensures that there are no unresolved analytical artifacts left (Teng et al., 2017).

When Fe and S enters the ocean, the S/Fe ratio is approximately 0.5, meaning more S is added to the ocean than Fe. The iron cycle is different from the sulfur cycle, because the supply of Fe to the ocean sediments is mainly in particulates as opposed to S which come as dissolved sulfate. Very little dissolved Fe reaches the ocean, and only 10% of the Fe in the ocean reaches the deep-sea sediments (Canfield and Farquhar, 2012*a*; Rickard, 2012). The supply of dissolved Fe is approximately 1 Tga^{-1}, while the flux of particulate Fe is up to 1000 Tga^{-1}. The particulate Fe is mostly transported in rivers, making the riverine Fe flux important (Rickard (2012)). In anoxic environments the S/Fe ratio play an important role because in these environments Fe^{2-} or H_2S will dominate, and here the formation of pyrite occurs. Fe will be trapped in pyrite minerals together with S, and it is possible to find the isotopic signature of Fe (Canfield and Farquhar, 2012*a*).

There is only a handful of reports regarding Fe isotopic signature in pyrite, however Lin et al.

(2016b) performed a study about Fe isotopes from the Shenhu area in South China Sea. The study suggests that $\delta^{56}Fe$ values increase with depth together with the pyritization and the $\delta^{34}S$ values in pyrite. The correlation is most likely due to the availability of H_2S through OSR and AOM, as isotopically light Fe is first to be consumed during pyritization, leaving behind an enrichment of $\delta^{56}Fe$ in the pore fluids (Lin et al., 2016a; Rickard, 2012; Severmann et al., 2006). Deeper into the sediments, the Fe isotopes change from isotopically light to heavy. An enrichment of ^{56}Fe in pyrite coincided with high sulfide abundances and corresponding positive $\delta^{34}S$values. Lin et al. (2016a) claims that pyrite formation in deeper sediments is a result of AOM and perhaps paleo-SMTZ.

3 Geological Setting

The Arctic Mid-Ocean ridges (AMOR) are ultra-slow spreading ridges located from 66°N to 90°N; AMOR is spreading at less than 20 mm every year and is one of the slowest spreading ridges on the planet. The ridges are a part of the Mid Atlantic Ridge, and the location is above the Arctic Circle hence the name AMOR (Pedersen et al., 2010*a*,*b*). In 1974 the first discovery of hydrothermal activity at the AMOR was reported, the hydrothermal system was situated on the Kolbeinsey ridge (3.1). After discovering the first hydrothermal system, more observations of hydrothermal activity were reported. Both inactive and active fields were discovered (Pedersen et al., 2010*a*,*b*). AMOR reaches 4000 km from the northern shelf of Iceland to the Siberian shelf in the Laptev Sea, and it passes through the Norwegian-Greenland sea (Pedersen et al., 2010*a*). The seafloor spreading in the Norwegian-Greenland sea started from 55 Ma in the early Eocene. 33 Ma later, in the early Oligocene, a change in stress field occurred. The spreading along the Mohns Ridge changed from orthogonal to oblique, and the transform plate motion changed to a divergent plate motion between Greenland and Eurasia (3.1) (Cruz, 2015). The ridges are separated into 6 different segments from south to north: the Kolbeinsey, Mohns, Knipovich, Molloy Ridges, Lena Trough, and Gakkel Ridge (3.1) (Pedersen et al., 2010*a*)

From south to north the AMOR changes from a shallow and magmatically robust ridge to a deep magmatically starved ridge system. The reason for the change is due to the Icelandic hot spot's influence lessening with a decreasing spreading rate and an increasing depth towards the north (Pedersen et al., 2010*a*) . The southernmost ridge, Kolbeinsey ridge, is strongly influenced by the Iceland Hotspot, it reaches a depth at 1000 m and continues to deepen northward. The Knipovich ridge has depths between 2500 m to 3000 m. The northernmost ridge; the Gakkel ridge has a depth of 5300 m. There is a correlation between increasing depth and decreasing crustal thickness. The average thickness of the Atlantic oceanic crust is 7 km, though Kolbeinsey ridge shows an anomalous crustal thickness of 9 to 10 km (Cruz, 2015). One possible explanation of the increase in crustal thickness might be the proximity of the Iceland hotspot. Moving northward, the crustal thickness decreases to 4 km at the central Mohns Ridge and 3.5 km at the Knipovich Ridge. The crustal thickness is at its thinnest at the magmatic areas of the Gakkel Ridge, being 1.5 km thick

(Cruz, 2015).

The AMOR segments are characterized by three main fracture zones from south to north. The fracture zones created two main changes in orientation. The fractcuring resulted in the separation of the Mohns Ridge from the Knipovich Ridge, and the Lena Trough from Gakkel Ridge (3.1) (Pedersen et al., 2010*a*) . On the south, the West Jan Mayen fracture zone defines the boundary between the Jan Mayen platform and the Mohns Ridge (JMFZ, 3.1). Moving northward, the Molloy fracture zone separates the Knipovich Ridge from the Molloy Ridge (MFZ, 3.1). The Spitzbergen fracture zone is the fracture zone located north of the Molly ridge (SFZ,3.1) (Cruz, 2015). The Mohn's ridge hosts hydrothermal systems: Jan Mayen, Loki's Castle, fåvne and Ægir, and the Seven sisters on Kolbeinsey (Pedersen et al., 2010*a*).

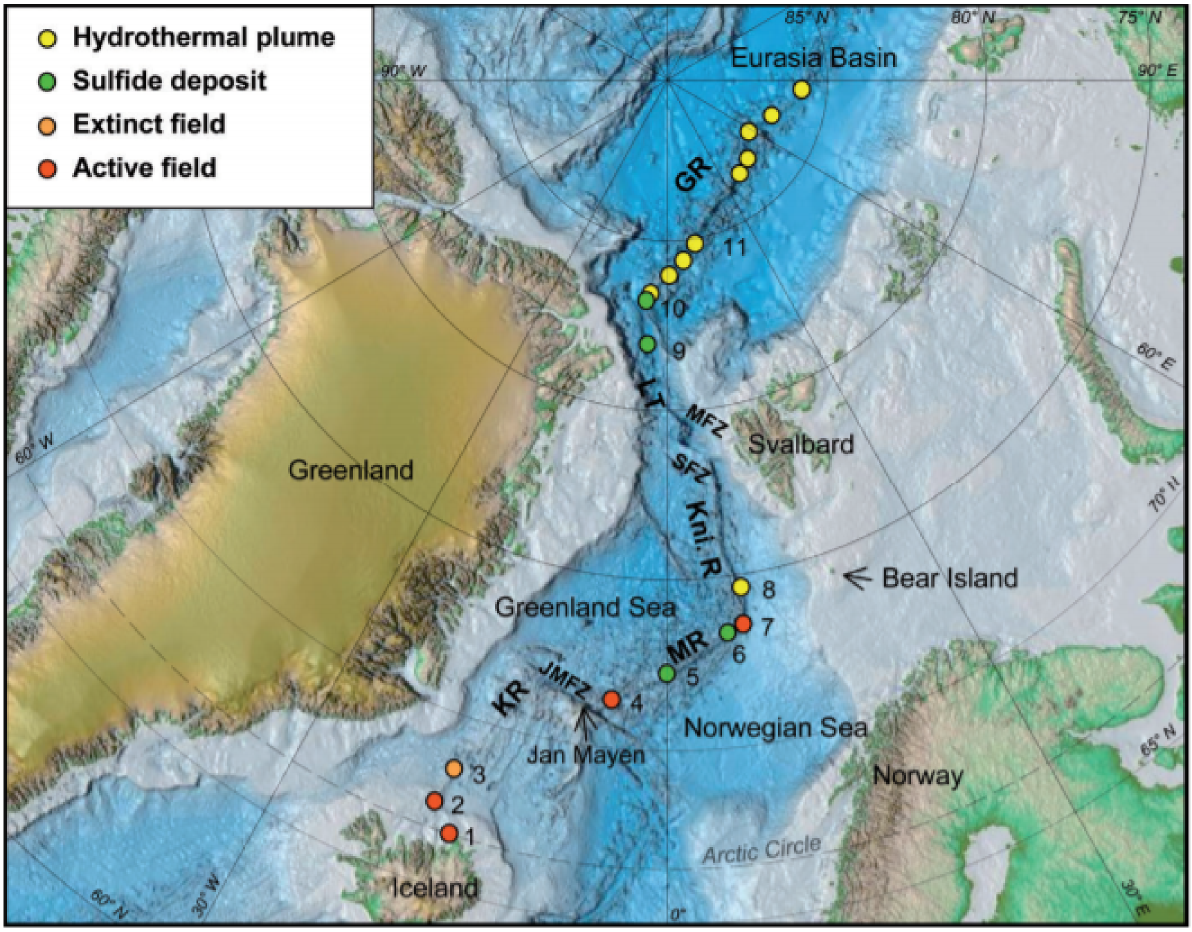

Figure 3.1: An overview of the Arctic mid-ocean ridges, the figure displays both inactive (orange) and active (red) hydrothermal systems. 1. Grimsey; 2. Kolbeinsey; 3. Squids forest extinct vent field; 4. Jan Mayen, Soria Moria, and Troll wall; 5. Copper Hill sulfide mineralized breccia; 6. Mohn's treasure sulfide deposit; 7. Loki's Castle; 8. Hydrothermal plume; 9. Sulfide deposits; 10. Sulfide deposits and shimmering water; 11. Hydrothermal plumes (Pedersen et al., 2010a)

3.1 Loki's Castle

Loki's Castle was discovered in July 2008 by Pedersen et al. (2010*a*,*b*), during the expedition with the R/V G.O. SARS. It is located on the Arctic mid-ocean ridges at 73°30N and 8°E. The vent field is situated where Mohn's ridge transitions to Knipovich Ridge. The transition is characterized by a sharp northward bend in the direction of the spreading axis (Pedersen et al., 2010*a*,*b*). The northward bend leads to an asymmetrical rift, where the western flank is affected by core complexes, while the eastern flank is covered with sediments from the Bear Island fan (Pedersen et al., 2010*a*,*b*; Baumberger, 2011). The deepest part between Mohn's ridge and Knipovic ridge is 2000 m; where a 30 km axial volcanic ridge (AVR) rises 1300 m above the valley floor. Loki's Castle is situated on top of the AVR (3.2). Loki's Castle consists of four high-temperature black smoker vents, the vents reaching a height of 13 m (Pedersen et al., 2010*b*). The black smokers are surrounded with two mounds of hydrothermal sulfide deposits; both mounds are approximately 20-30 m high, 150-200 m across and 150 m apart from each other. The western mound hosts the chimney vents; Sleepy, Menorah and Camel, while the Eastern mound hosts the João vent (3.2) (Pedersen et al., 2010*a*,*b*).

Based on the surface geology around and under Loki's Castle, the vent field is mainly basalt-hosted. The mound is built on basalt flows, and a thin layer of sediments covers the sea-floor surface. However, Loki's Castle is located 5 km away from the Bear Island Fan, where a footwall is exposed (3.2) (Pedersen et al., 2010*a*,*b*). The Bear Island Fan is present in the rift valley northeast of the AVR, while sediments from the fan occur in half grabens both north and northwest; these reach a thickness of 700 m. The distal part of the Bear Island Fan reached the Loki's Castle vent field 1.3-1.5 million years ago, resulting in a sediment-influenced hydrothermal system Pedersen et al. (2010*a*,*b*). The hydrothermal plume is not always detectable due to strong currents in the area. The non-buoyant plume is located between 2000 and 2100 m deep (Cruz, 2015) (Cruz, 2015).

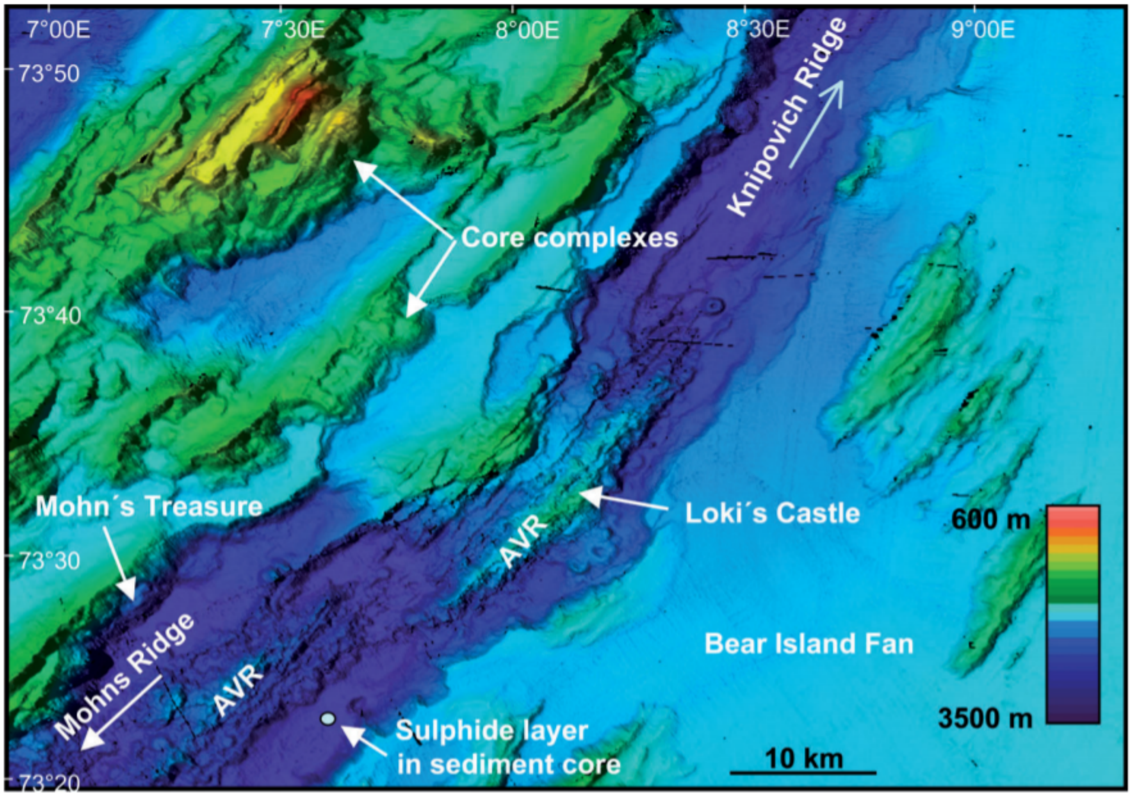

Figure 3.2: A Bathymetry map of AMOR where Mohn's ridge transitions into the Knipovich ridge. The spreading is orthogonal with the AVR oriented parallel to the local orientation of the ridge, The eastern flank is buried under sediments from the bear island fan. Normal faults cut through the western flank. Loki's castle is situated on the AVR as shown on the map (Pedersen et al., 2010a,b)

3.1.1 Barite field

The Northeast of the eastern mound is the location of the Barite field (3.3). The venting is low-temperature, and the area is characterized by 1 m tall small barite chimneys and abundant white bacterial mats. The temperature of the water above the microbial mats has been measured to be 20°C. The barite chimneys and the microbial mats frequently occur along lines that likely reflect the pattern and fluid flow rate. Depending on the chemistry of the vent fluids, sulfate minerals such as barite are commonly found around hydrothermal systems (Eickmann et al., 2014; Baumberger, 2011). Two possible main processes might be behind creating the barite chimneys; the first is hydrothermal leaching of the volcanic crust. The second is the remobilization of barite in sediments because of microbial reduction (Eickmann et al., 2014).

The Barite field consists of both active and inactive barite chimneys; the active chimneys are covered by white microbial mats, resembling white cotton candy (3.4) (Steen et al., 2016). The microbial mats also cover the sediments and siboglinid tubeworms (Eickmann et al., 2014; Steen et al., 2016). The barite field has diluted and chemically modified venting relative to the black smokers (Steen et al., 2016; Eickmann et al., 2020; Baumberger, 2011). Studies of microbial activity display a depletion in the fluids, meaning that the microorganisms in the barite chimneys seem to be related to AOM (Steen et al., 2016).

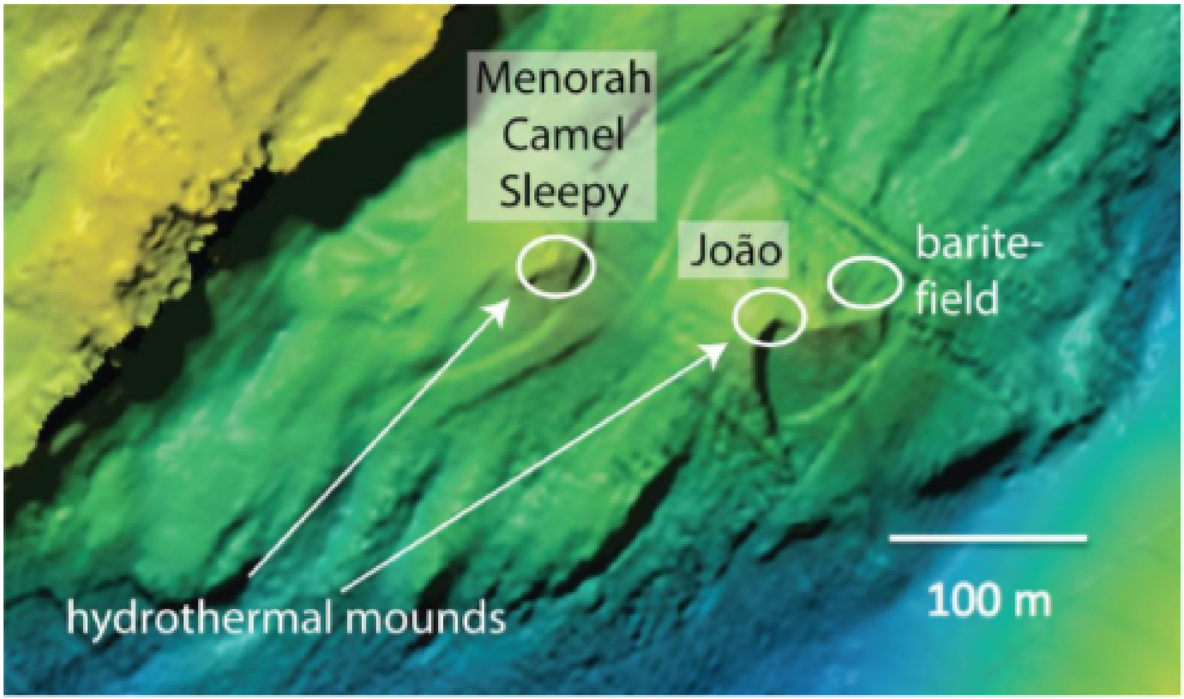

Figure 3.3: A bathymetry map of Loki's Castle vent field, the map displays the two mounds on the western and eastern flank. The western mound hosts the Menorah, camel, and sleepy chimney vents, and the eastern hosts the João chimney vent. The Barite field is located close to the eastern mound. Picture taken from Eickmann et al. (2020)

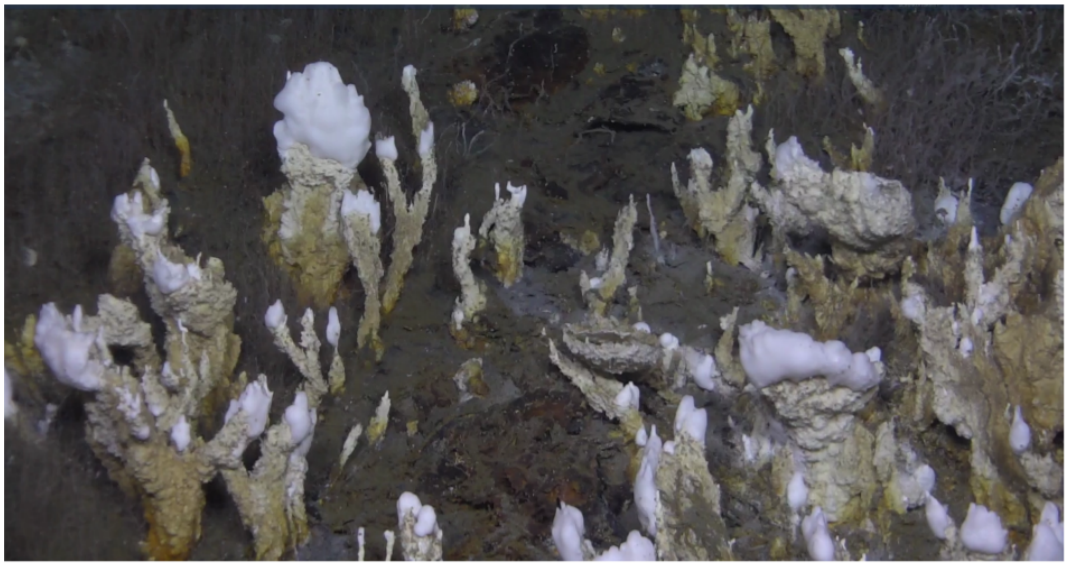

Figure 3.4: The picture taken in 2017 of active barite chimneys. The picture shows the white microbial mats covering the barite chimneys (Viflot, 2019).

4 Method

4.1 Samples

Samples were collected from the Loki's Castle Barite Field in 2014, and 2018 during research cruises with R/V G.O. Sars, and include one gravity core (GS14), BC3 push cores, and BC4 blade core samples. Pore fluids were extracted from sediments on board using Rhizon filters and analyzed for their major and trace element composition, and sediment subsamples were collected for microbiological analysis on shore.

For the current study, subsamples were collected in 2021 for scanning electron microscopy (SEM), bulk geochemical analyses and stable isotope analyses. Sample depths were determined based on pore fluid profiles of the GS14 core (fig.4.1). Cores have been stored at 4°C after collection and their sediment geochemistry can therefore be assumed to be relatively unaffected, as mineral dissolution or isotopic equilibration would be slow at these temperatures. Sampling was done using cleaned plastic spoons to avoid metal contamination and samples were dried at 20°C for several days before further processing.

All samples were collected in the barite field in 2014,and 2018. BC3 J-I are bulk samples, and sediments are mixed together with no specific depth indicator (table 4.2). Eight sediment samples were sampled from the gravity core, the sediment core has since then been stored in the refrigerator at the University of Bergen.

4.1.1 Sampling strategy

The GS14 core was brought from the refrigerator up to the biogeochemistry lab at the University of Bergen. Sampling of the sediment core happened in May 2021, and the sample depths were decided after plotting pore fluids profiles previous measured (table.4.2). The sample areas of interest are marked in grey and were based on the different peaks in the pore fluid concentrations. One horizon was based on the peak of the metals, rest were based on AOM-SR related pore fluids (fig.4.1. The plots were used to determined which parts of the core were of interest, the determination was based on sulfate reduction rates, methane, and sulfate. The pore fluid metal concentrations cobber, nickel, and zinc were plotted to find potential depths of interest. Samples were taken where the sulfate reduction rates, and the concentrations of pore fluids were either high or low. Three of the samples were added spontaneously when working on the sediment core, the horizons stood out in color and textures. The three additional samples were the 15 cbsf horizon, the 92 cmbsf horizon, and the 120 cmbsf horizon (table.4.2. The BC3 samples were provided by *PHD candidate* Francesca Vulcano (table 4.1). The BC3 samples were taken in 2018 and 2019 with a blade core, and does not have a specific depth.

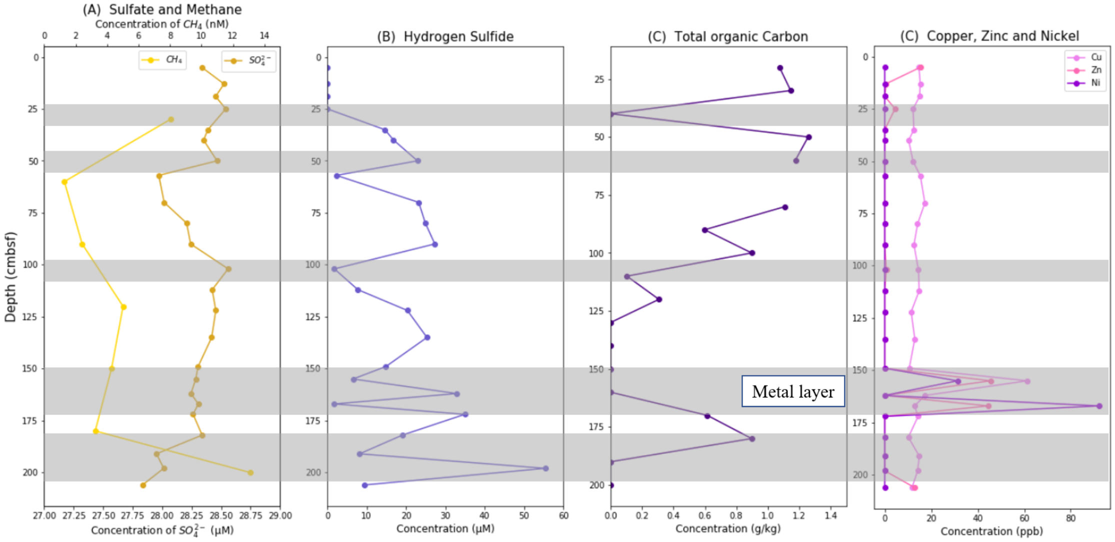

Figure 4.1: The pore fluid profiles selected based on Lin et al. (2016a, 2017)'s papers. The grey areas are sampling areas.

Table 4.1: An overview over the samples from the barite field taken in 2018 and 2019, the coordinates, depth, temperature, porewater sulfide concentration, alkalinity and porewater sulfate.

Samples	**Coordinates (UTM)**	**Depth (cmbsf)**	**Temperatur**
J	662820.33 Easting, 8170750.47 Northing, 31X	16-18	2-3
K	662820.33 Easting, 8170750.47 Northing, 31 X	6-8	0
I	662814.75 Easting, 8170705.18 Northing , 31 X	0-20	0-30

Table 4.2: An overview over the samples and depth collected from the sediment core, and sampled in 2014. The samples listed below were sampled 26.05.2021.

Sample ID	**Depth (cmbsf)**
GS14-GC14 (A)	15
GS14-GC14 (B)	33
GS14-GC14 (C)	54
GS14-GC14 (D)	92
GS14-GC14 (E)	120
GS14-GC14 (F)	156
GS14-GC14 (G)	167
GS14-GC14 (H)	200

4.2 Scanning electron microscope (SEM)

4.2.1 Sample preparation

Approximately one teaspoon of each of the GS14 and BC3 samples were placed in separated petri dishes and dried for several days. GS14 and BC3 samples were either air dried or dried in an oven at 20°C. After drying, the samples was glued to carbon tape and coated with carbon by the *department engineer* Irene Heggstad at the University of Bergen. The instrument used for coating carbon was Agar Turbo Carbon Coater at the ELMILab.

4.2.2 SEM analysis

The samples were placed inside the ZEISS SUPRA 55VP field emission for the SEM analysis. The secondary electron detector was set to optimize pictures and the settings were 5 kW, with a working distance between 3-5 mm and an aperture at 30 μM. For geochemical analysss, the settings were changed to 15 kW, with a working distance at 8 mm and an aperture at 60 μMm. The in-lens secondary electron detector was used on some of the analyses and pictures to optimize the quality where it was needed.

4.3 Bulk geochemistry

Dried sediment samples were dissolved using concentrated hydrofluoric (HF) and nitric (HNO3) acid on a hot plate for several days, before being redissolved into 2% HNO3 for analysis by inductively-coupled plasma optical emission spectroscopy (ICP-OES). A duplicate set of samples were heated at 1000°C for 2 hours before acid digestion to remove organic matter and determine the loss-on-ignition (LOI). Elements analyzed by ICP-OES includes major elements such as; S, Mg, Fe, and Mn, and minor elements such as; Cu, Co, Ni, and Zn. Barite did not dissolve during acid digestion and barium concentrations are therefore not used in this study.

The samples where dried and marked with names before they were given to the Staff Engineer for hydrofluoric (HF) acid digestion at the University of Bergen, before the HF acid digestion the samples were burned at 1000°C for 2 hours to get rid of organic matter and to determine glow loss. The samples are dissolved in hydrofluoric acid digestion and nitric acid, after the acid digestion the samples were transferred to the Chief Research Technician for inductively coupled plasma – optical emission spectrometry (ICP-OPS) at the University of Bergen. Before the analyses of the samples, they are diluted to an appropriate level by 2% w/v HNO3. The samples were analyzed for major and trace elements. The concentration of major and trace elements were determined by using a Thermo Scientific ICap 7600 Inductively Coupled Plasma Atomic Emission Spectrometer (ICP-AES).

A multi element standard solution is prepared from certified single element solutions from SpectraPure. Sc is used for internal standardization before doing quantification by external calibration curve. For quality control the USGS CRM BCR2 (basalt, Columbia River) is used, the BCR2 follows all the same steps as the samples went through.

4.4 Microbial analyses

The microbial analyses were conducted by *Associate Professor* Steffen Leth Jørgensen at The University of Bergen. To separate the microbes from the sediments, and to break apart the microbes; a buffer was added, and the samples went through several centrifugations. The main goal was to amplify the 16S rRNA. To amplify the 16SrRNA the two samples had to go through a PCRs. To avoid false results, a PCR was conducted for a negative control. A master mix for 5 samples were prepared in a 1.5 mL Eppendorf tube. The master mix contained H_2O, 2x Hot star mix, 519 primer $100\mu M$ and 805 primer $100\mu M$. The master mix got distributed into each PCR reaction tube, $2.5\mu L$ of DNA template was added to each PCR tube, expect the blank. The last step was the thermocycler, were the temperature, time, and amount of cycles varied.

4.4.1 Data sequencing and processing

Sequencing was conducted after the PCRs and then processed. The sequencing resulted in a list of every sample which contained the sequences and quality information. The data got processed; first step was to remove the primes and discarded all samples without primers. The second step was to filter through the samples with a maximum expected error at 2σ, and pool together all the samples that were indistinguishable from each other. The third step was to align together the samples with 97% similarity. Then taxonomy got assigned using the SILVA database. All samples that were not

Bacteria or Archaea and singletons got removed. The sorting of taxonomy was processed on Excel; the abundance got pooled for each unique order.

4.5 Sulfur isotope

4.5.1 Sulfide extraction

Sulfide was extracted from the sediments for sulfur isotope analysis using the hot chromium distillation method after Canfield et al. (1986). This method is specific for iron mono-sulfides, pyrite and elemental sulfur and produces silver sulfide (Ag_2S) that is required for high-precision multiple sulfur isotope measurements. A chromium chloride solution was prepared by reducing $CrCl_3$ to $CrCl_2$ in a flask filled with zinc pellets under an anoxic atmosphere (N_2) for 30 minutes (fig.4.2). The change from Cr^{3+} to Cr^{2+} was confirmed by a color change from dark green to bright blue. The reduced solution was extracted from the flask using a 50 ml syringe and stored (without air) in the refrigerator for a maximum of one week (fig.4.2).

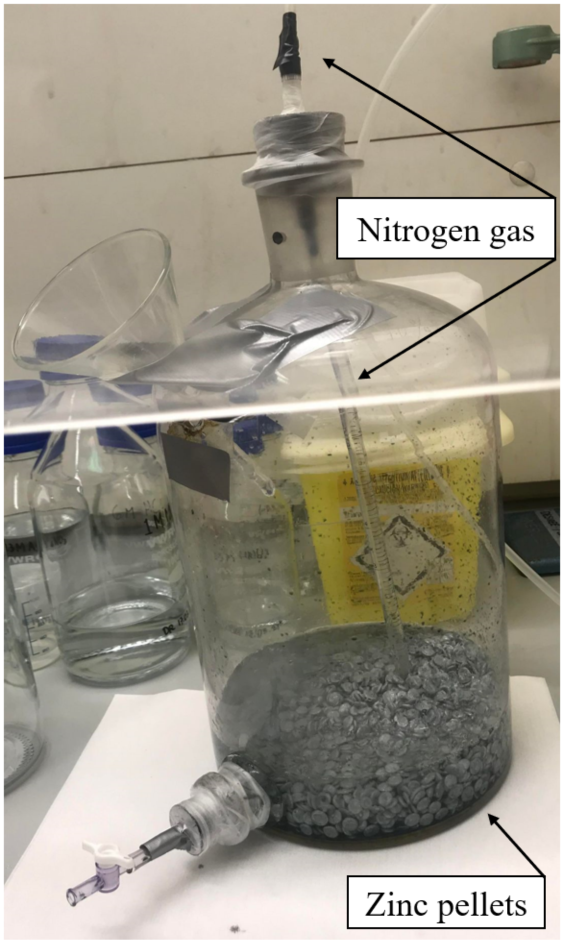

Figure 4.2: Flask filled with zinc pellets in a nitrogen atmosphere, here the chromium chloride solution was reduced. Picture taken by Karen Elisabeth Moltubakk.

To trap the H_2S gas released from the reduced sulfide, a silver nitrate trap ($AgNO_3$) was prepared trap. The silver nitrate trap was designed to create a chemical reaction between silver (Ag) and sulfide (S^{2-}), the reaction's end product was Ag_2S. The sulfide originates from H_2S gas from heating the sediments whilst soaked in $CrCl_3$ and HCl. The $AgNO_3$ trap was prepared by mixing 3 ml of 0.3M $AgNO_3$, 2 ml of 1.5M HNO_3, and 10 ml ultrapure H_2O. The $AgNO_3$ trap was attached to the extraction line setup, and new Pasteur pipettes were connected to the extraction line setup. The pipettes were attached to the condenser and inserted into the $AgNO_3$ traps. The Pasteur pipette was placed without touching the bottom, to prevent silver nitrate forming in the pipette making the cleaning process easier.

Water traps were filled with 30 ml ultrapure H_2O before being attached to the extraction line setup(fig.4.3). The gas inlet tubes were connected to each line of the setup The samples were weighed in 100 ml rounded bottom flasks; the weight ranged between 15 to 20 mg. Before adding 3 boiling stones and 5 ml ultrapure H_2O. The rounded bottom flasks and glass stoppers were attached to the extraction line setup (fig.4.3). The condensers and tubing were connected to the set-up(fig.4.3). Yellow clamps were placed on the joints from the round bottom flask, before turning on the water and N_2 gas to flush the system and remove any oxygen, the flushing lasted 5 minutes. Last step was adding 20 ml of $CrCl_2$ and 10 ml 6M HCl to each round bottom flask, before turning the heating mantles up to 4. The samples were left to react for 2 hours under gentle boiling, with a checkup after 45 minutes in case of leaking.

Filters and plastic trays were weighed before the filters were placed onto a vacuum filtration apparatus, which was connected to an aspirator to the water tap. The silver nitrate solution with Ag_2S was poured over the Bucher funnel and rinsed with ultrapure H_2O and ammonium. The ammonium was poured after the first rinse with H_2O, the ammonium was added to neutralize the acidic Ag_2S, after ammonium, more H_2O was poured over the sample. The filters were stored in a drying box afterwards. The dried samples were weighed and the mass of Ag_2S was calculated, the ideal weight was more than 3 mg for each the sample for it to be analyzed. After weighing, the samples got scraped of the filter paper and carefully transferred to small glass vials and sent to Münster in Germany for sulfur isotope analysis.

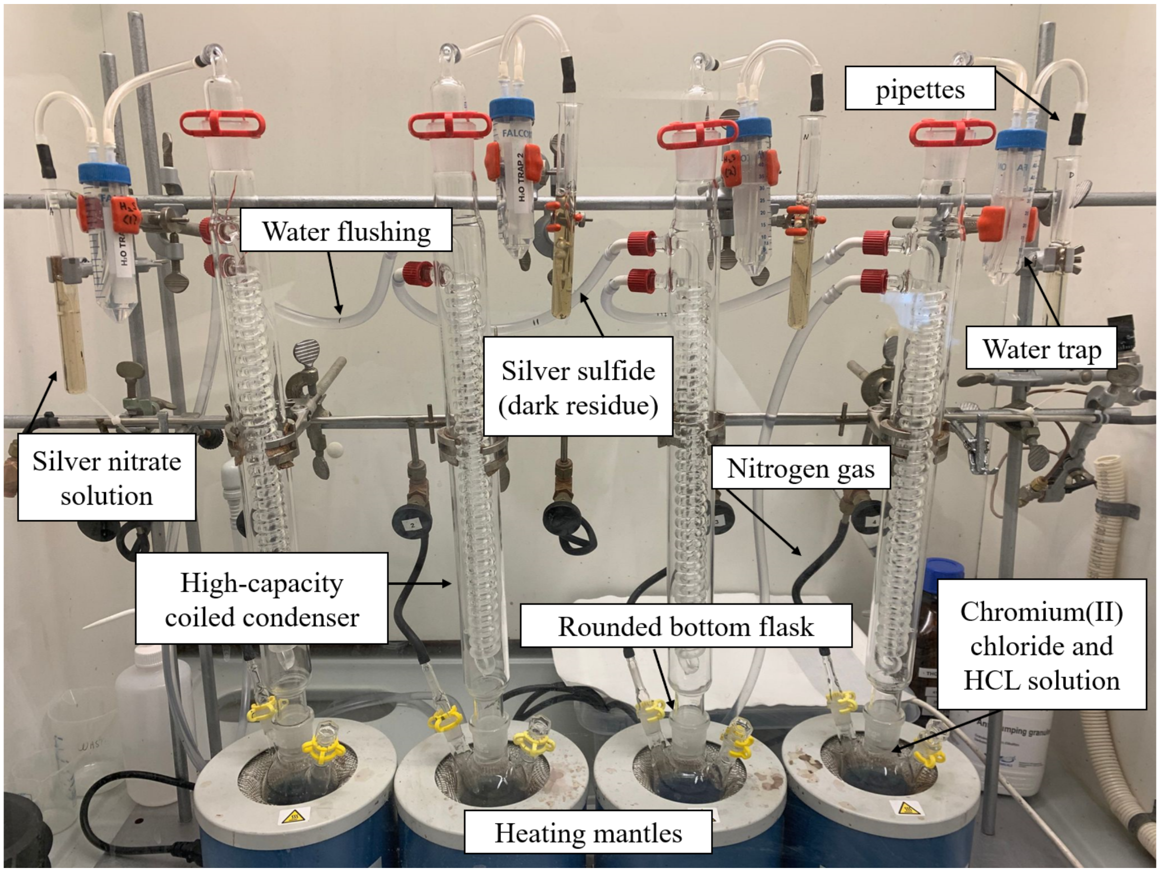

Figure 4.3: The setup for the chromium distillation method. Picture taken by Karen Elisabeth Moltubakk.

4.5.2 Sulfur isotope analyses

Sulfur isotopes were analyzed as SF6 at the University of Münster using a ThermoFinnigan MAT253 mass spectrometer following cryogenic and gas chromatographic purification (Farquhar et al., 2000), with an average external precision of 0.09‰, 0.017‰ and 0.331‰ for δ^{34}S, Δ^{33}S, and Δ^{36}S, respectively. Values of δ^{34}S are calculated as eq.10 and values of Δ^{33}S as eg.11:

$$\delta^{34}S = 1000 \times \frac{\frac{^{3x}S}{^{32}S}_{sample} - \frac{^{3x}S}{^{32}S}_{standard}}{\frac{^{3x}S}{^{32}S}_{standard}} \tag{10}$$

$$\delta^{33}S - 1000 * ((1 + \delta^{34}S/1000)^{X-1} \tag{11}$$

4.6 Iron Isotopes

In addition to sulfur isotopes, iron isotopes were measured in sulfide samples to provide complementary information on the microbial processes leading to pyrite precipitation (Lin et al., 2016b). To extract Fe from pyrite, a sequential extraction method was performed that also provides information on iron speciation in the studied sediments.

4.6.1 Sequential Fe extraction

The sequential iron extraction method used in this study was based on Poulton and Canfield (2005), with modifications from Claff et al. (2010) and Slotznick et al. (2019) to obtain pyrite-Fe.

Reagents were freshly made before starting the sequential Fe extraction, and include 1M Na-Acetate (at pH 4.5) for extraction of carbonate-bound iron and acid-soluble sulfides. 1M Hydroxylamine-HCl for the extraction of iron oxides like ferrihydrite and lepidicrocite. 0,29M Na-dithionate (at pH 4.8) for the extraction of the iron oxides geothite, hematite and akageneite. 0.2M ammonium oxalate (pH 3.2) for the extraction of magnetite. Lastly 14M HNO_3 for the extraction for pyrite.

Table 4.3: Displays the dilution steps for Fe standards for spectrophotometric analysis, with the concentration in ppm of Fe, and extraction solution in ml.

Standard	**µl SPS Fe (1000 ppm)**	**ml extraction solution**
0 ppm Fe	0	5.000
5 ppm Fe	25	4.975
10 ppm Fe	50	4.950
25 ppm Fe	125	4.875
50 ppm Fe	250	4.750
100 ppm Fe	500	4.500
200 ppm Fe	1000	4.000

Approximately 130 mg to 150 mg of sediment samples were weighed in a Falcon tube, the exact weight was written down and each Falcon tube was marked with name of sample, and the current date. First step was to add 10ml of Na-acetate to the Falcon tubes and placed in a water bath with shaking table at 50°C for 48 hours. The Na-acetate was centrifuged for 2 minutes at 5000 rpm in the biochemistry lab at the University of Bergen at the Earth Science department. After centrifugation, the sample liquid was poured into 15 ml Falcon tubes and stored in the refrigerator, the samples were cleaned with ultra-pure H_2O before hydroxylamine-HCl was added, and the samples were left for 48 hours in water bath with shaking table at 26°C Same procedure as above, the hydroxylamine-HCl was centrifuged for 2 minutes at 5000 rpm and poured into 15 ml Falcon tubes, stored until further analyses. The samples were cleaned with ultrapure H_2O, before adding the freshly made Na-dithionate reagent. Samples with Na-Dithionate were placed in water bath with shaking table at 21°Cfor 2 hours before centrifuged for 2 minutes at 5000 rpm, and then the solution was poured into 15 ml tubes and stored in the refrigerator. The samples were cleaned with ultra-pure H_2O. After cleaning they were placed in the refrigerator for two days before further analysis. Two days later, 0.2M ammonium oxalate was added to the sediments and placed in a water bath with shaking table at 21°C for 6 hours, before being centrifuged for 3 minutes at 5000 rpm. The change in centrifuge time is due to the sediment's behavior, two minutes are no longer sufficient at separating the sediments from the fluid and makes it difficult to pour the liquid into the 15 ml Falcon tubes without losing sediments. Increasing the centrifuge time with one minute is enough for the sediments to stick to the bottom. The sediments were cleaned with ultra-pure water, before left in the refrigerator overnight. 5 ml of HNO_3 was added to the 50 ml Falcon tube and left in water bath with shaking table at 21°C for 2 hours before being centrifuged for 3 minutes at 5000 rpm.

4.6.2 Fe concentrations

Matrix-matched standards were prepared for each of the reagents to obtain calibration curves. The HNO_3 was diluted 10 times before making the standards. The standards were made following table 4.3 for dilution steps. The standards were stored in the fridge until the sequential Fe extraction.

Ferrozine reagent was prepared for the analyses of Iron concentration, the reagent consists of 2.4g HEPES buffer with 0.004 g Ferrospectral, 2.0 g hydroxylamine-HCL and ultra-pure H_2O up to 200 ml. Standards with Ferrozine reagent and the Na-acetate matrix was prepared in plastic cuvettes, the cuvettes was shaken and left overnight before analysis of the absorbance of the standards. The same procedure was followed for the samples soaked in Na-acetate the day after and left for 24 hours before being measured in the UV-VIS spectrophotometer. The same procedure for measurements as above was followed for hydroxylamine-HCl, Na-dithionate, and ammonium oxalate, and new standards were made for the different matrixes. The cuvettes were left for 24-48 hours before analyzing the absorbance of standards and the samples. Four samples with Na-dithionate matrix had a higher concentration of Iron than in the highest standard, hence the four samples were diluted. The dilution had a 50/50 ratio of water and sample, while the volume remained the same. The instrument used for the measurement of samples and standards was the UV-VIS spectrophotometer at 562 nm in the biogeochemistry lab at the department of Earth Science at the University of Bergen.

Figure 4.4: The UV-VIS spectrophotometer used for the iron concentration measurements. Picture taken by Desiree Lisette Roerdink.

4.6.3 Iron isotope analyses

Iron extracted by HNO_3 in the last step of the sequential extraction procedure is assumed to reflect pyrite-bound Fe, as nitric acid does not dissolve silicate-bound Fe. This solution was therefore used for Fe isotope analyses in this study. One ml of the extract was dried down in a Teflon beaker on a hot plate at 130°C, and the residue was subsequently taken up in 1 ml of 6M double-distilled hydrochloric acid (HCl). Based on Fe concentrations measured by spectrophotometry, approximately 30-40 mg of Fe was loaded for each sample on a AG1-X8 anion exchange resin (100-200 mesh) in a class A100 laminar flow hood. Matrix elements were eluted using 6 ml of 6M HCl and Fe was subsequently eluted using 2 ml ultrapure water and 4.5 ml 5M double-distilled HNO_3, after Moeller et al. 2014. The eluted sample was dried down overnight and taken up in 0.3M HNO3.

Samples were subsequently analyzed for Fe concentrations using a Nu Plasma II multi-collector inductively coupled plasma mass spectrometer (MC-ICP-MS) with an upgraded Plasma 3 interface.

A blank acid sample that was run over the same anion exchange columns yielded a blank of 4 ng Fe, which corresponds to 0.00001% of the Fe in the samples. Solutions were diluted to 2 ppm Fe in acid-cleaned Teflon vials and analyzed for Fe isotopes in wet plasma mode at pseudo medium-resolution (R5-95% = 9899) with ^{54}Fe in Faraday cup L5, ^{56}Fe in H1 and ^{57}Fe in H4. Zeros were measured by ESA deflection for 30 seconds before each block, and samples were analyzed in 2 blocks of 20 measurements of 8 seconds. Each sample was run in duplicate, and an internal standard (Han Fe) was regularly measured to confirm accurate Fe isotope ratios. Fe isotope ratios ($\delta^{56}Fe$ and $\delta^{57}Fe$) were corrected for mass bias using standard-sample bracketing (SSB) with the bracketing standard IRMM-014, following equation 12:

$$\delta^{56}Fe_{spl}, corr = \frac{\frac{^{56}Fe}{^{54}Fe}_{spl} meas}{[0.5 \times \frac{^{56}Fe}{^{54}Fe}_{std1} meas + 0.5 \times \frac{^{56}Fe}{^{54}Fe}_{std3} meas]} - 1 \times 1000 \tag{12}$$

A plot of $\delta^{57}Fe$ versus $\delta^{56}Fe$ confirmed that all samples and standard fall (within error) on the terrestrial mass-dependent fractionation line with a slope of 1.47. Based on repeated analyses of Han Fe (n = 4), the external precision on $\delta^{56}Fe$ was 0.14 (2s).

5 Results

5.1 Pyrite morphology

Samples from GS14-GC14 (GS14) A to H and GS18 ROV28 BC3 (BC3) I and J contain framboidal pyrite and dispersed euhedral pyrite crystals (fig.5.1 and fig.5.2). The euhedral pyrite crystals occur as octahedrons.

The octahedral crystal habit is distinct for pyrites and the crystal habit is clearly visible on fig.5.1 and fig.5.2. The framboidal pyrite has a variation in size from 4 μM to 10 μM (fig.5.1). The framboidal pyrite consists of uniform microcrystals with a octahedral crystal habit. The dispersed pyrite crystals have a large variation in size from 1 μM to 10 μM (fig.5.2). The dispersed pyrite in the cores GS14 and BC3 varies more in sizes compared to the framboidal pyrite. Analysis to deduce mineral composition on the pyrite shows a composition of S and Fe as the main ions, the expected composition for pyrite.

Some pyrite contained a higher amount of Fe than S, the framboids with a high Fe concentrations differ in appearance (fig.5.1D). The Fe-rich framboidal pyrite does not exhibit the distinct crystal habit, though still occurring as framboids (fig.5.1D). The samples collected from the GS14 core consisted of less framboidal pyrite, and the pyrite from the sediment core occurred mostly as octahedrons shaped pyrites. The BC3 core consisted mainly of framboidal pyrite and with few single octahedrons, compared to the GS14 core which contained less pyrite in general (fig.5.1D). Comparing GS14 and BC3 with each other is difficult. BC3 has no depth indicators, making it difficult to compare the different horizons to the GS14 core. The amount of pyrite varied with BC3 containing more pyrite than GS14.

BC3 contains more barite than GS14, the matrix in BC3 consists of mostly barite and to some degree mineral phases with silica (fig.5.3A, C). GS14 consist of mainly mineral phases with silica and crystallized salt from seawater (fig.5.3B, D).

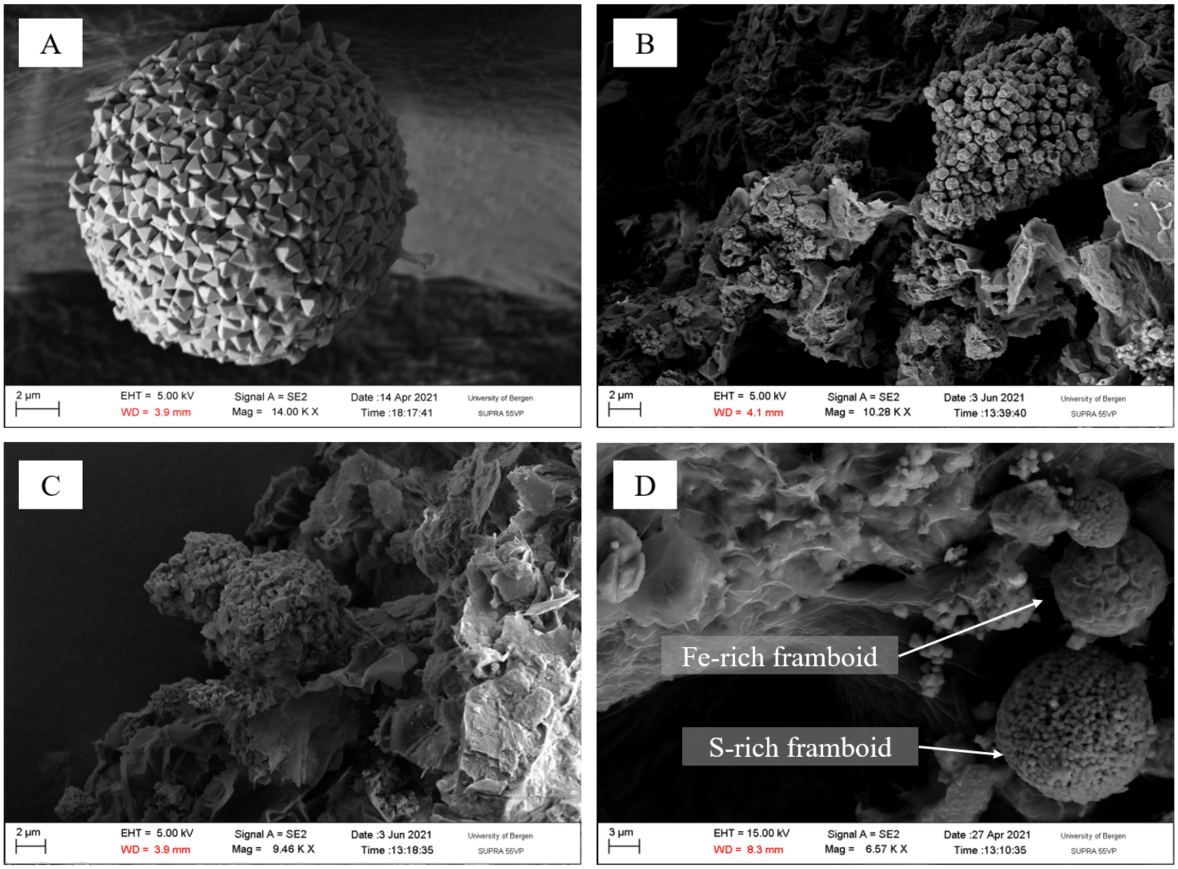

Figure 5.1: Framboidal pyrite either as standalones or in clusters with other framboidal pyrite. A) A framboidal pyrite with octahedral crystals, from the BC3 sample. B) Pyrite in clusters, lacking the distinct rounded shape. The matrix surrounding the pyrite is mainly barium and silica, from the GS14 sample. C) Two framboidal pyrite, covered in biofilm. The matrix consists of barium and silica, from the BC3 sample. D) Clustered framboidal pyrite in varying sizes, the matrix is barium, silica, and salt, from the BC3 sample.

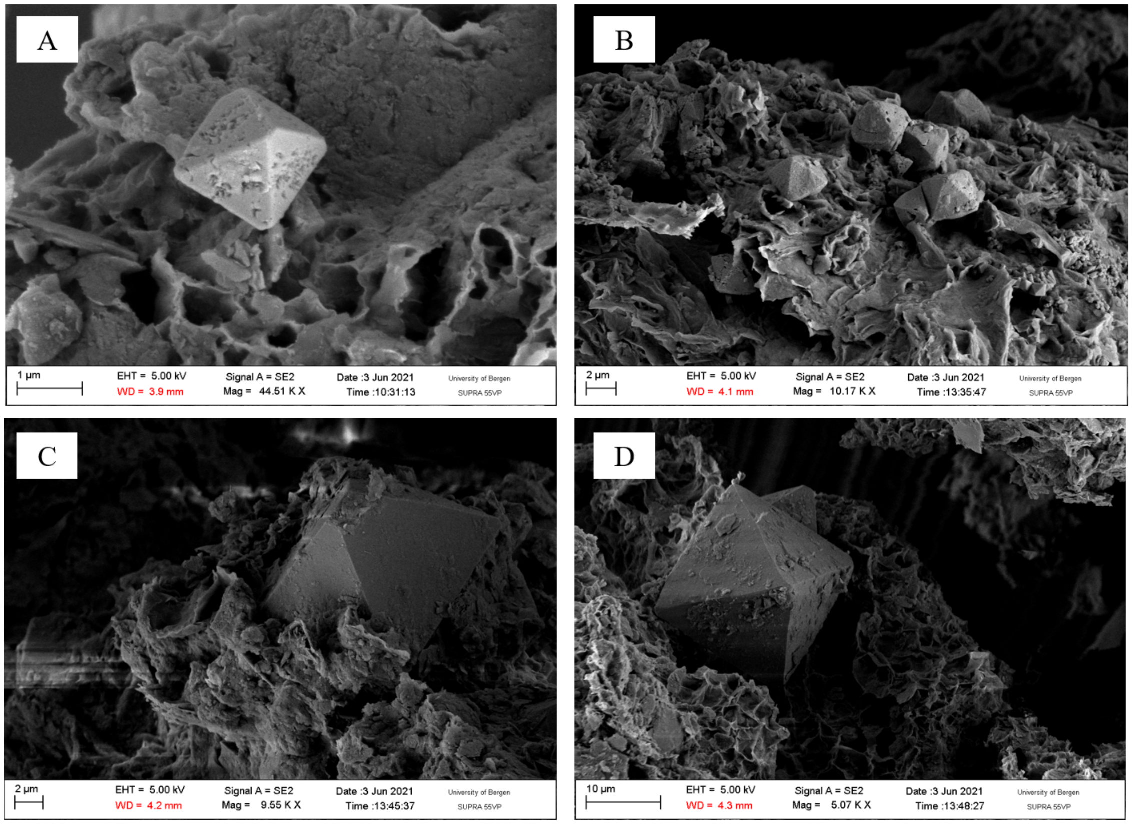

Figure 5.2: Dispersed pyrite crystals in a silica-rich matrix, and all the pcitures are taken from the GS14 core. A) A single pyrite crystal in mainly silica matrix with some barium crystals. B) Four pyrite crystals in silica and salt matrix. C) One pyrite crystal in silica matrix. D) One pyrite crystal in silica and salt crystals. The SEM pictures were taken with the secondary electron lens.

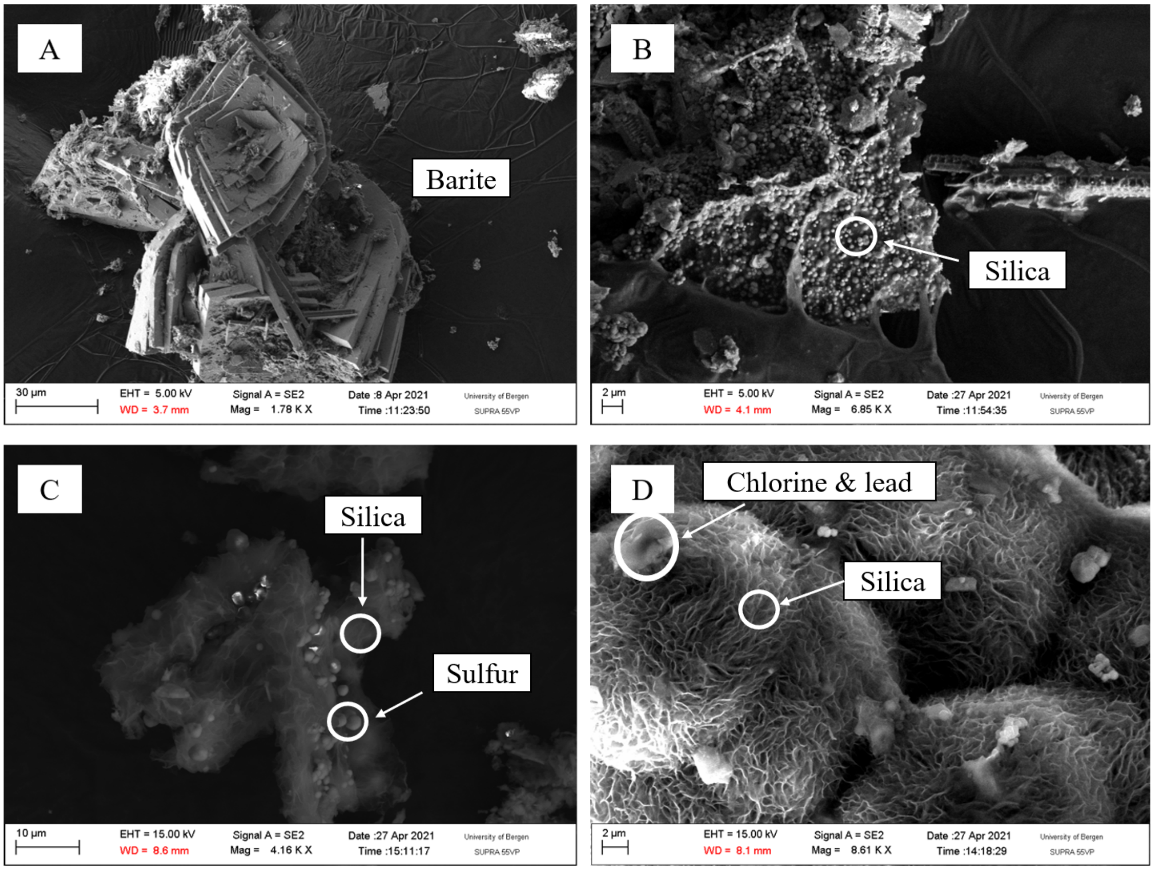

Figure 5.3: GS14 and BC3 contained mainly silica, barium, and salt. A) Twinning barium crystals, the barium crystals vary in size from 5 µ and up to 30µ as seen on the picture, from the BC3 sample. B) Tiny silica crystals, all perfectly rounded and having a smooth surface, from the GS14 sample. C) Predominantly sulfur crystals in a matrix of Silica and magnesium, from the GS14 sample. D) Chlorine and lead in a matrix of silica, magnesium, and aluminum, from the GS14 sample.

5.2 Sediment geochemistry

Selected cation and anion concentrations in the sediment samples were quantified by ICP-OES (tables 4.1 and 4.2). The tables 4.1 and 4.2 include the concentration of the ions in ppm, depth of the GS14 core and sample name. BC3 (J) is a bulk sample and does not have a specific depth, the sample is somewhere between the 0-20 cmbsf horizon. The cations and anions were selected based on several criteria; Fe and Mn is connected to redox, while Fe is also connected to pyrite. S is selected due to its connection with pyrite. Cu, Zn and Ni is connected to hydrothermal processes, and Ti is connected to low-temperature. Ba was selected because of its high concentration in BC3.

Mg is connected to the seawater circulation and zero Mg input from hydrothermal systems.

The concentration of sulfur vary from being not detected to 4000-5000 ppm (table 4.1). The iron concentrations are significantly higher compared to the sulfur, ranging from 140 000 ppm to 34 000 ppm, with one exception being the BC3 core with a concentration of 7202.9 ppm. The copper concentrations are consistent through the GS14 core (457.2 ppm to 1760.5 ppm), with the exception in the 167 cmbsf horizon (21914.5 ppm). The copper concentration in the BC3 core is little compared to the GS14 core. The zinc concentrations have a variation from 525.0 ppm to 8580.4 ppm, before peaking to 41758.6 ppm in 167 cmbsf horizon (table 4.1). Nickel varies from not detected (ND) to 30 ppm with one exception being the 167 cmbsf horizon, where the concentration increases to 194 ppm (table 4.1). The high concentrations of metals in the 167 cmbfs horizon can indicate high-temperature settings.

The barium concentration in the GS14 core have a large variation from 491.0 ppm to 11365.8 ppm. The BC3 core contains significantly higher barium content compared to the GS14, with a concentration of 15300.5 ppm (table 4.2).The difference between BC3 and GS14 can be observed from the SEM pictures, where the BC3 sample contains more visible barium than the GS14 core. The GS14 core contains high concentrations of magnesium, with large variation from 20093.5 ppm to 110044.8 ppm. The BC3 core has magnesium concentrations of 8752.4 ppm which is significantly lower than GS14. The manganese concentrations in the GS14 core vary from 5534.7 ppm to 1392.6 ppm. The manganese concentrations in the BC3 core is 147.5 ppm (table 4.2). The titanium concentrations decrease with depth in the GS14 core. In the 167 cmbsf horizon, the titanium concentrations decrease to 31.0 ppm before increasing in the 200 cmbsf horizon to 968.9 ppm. The BC3 core has a titanium concentration of 571 ppm (table 4.2).

In general, the concentrations of different ions are higher in the GS14 core compared with the BC3 core, except for barium.

Table 5.1: Concentrations in ppm of sulfur, iron, copper, zinc, and nickel from the ICP-OES sediment analyses. Sample ID and depth are listed below, and not detected ions are listed as ND.

Concentration (ppm)						
Sample ID	**Depth (cmbsf)**	**S**	**Fe**	**Cu**	**Zn**	**Ni**
GS14-GC14 (A)	15	4240.3	142993.7	1760.5	8580.4	34.7
GS14-GC14 (B)	33	ND	38409.6	892.1	1388.6	21.0
GS14-GC14 (C)	54	5057.7	85553.8	1048.6	925.4	30.9
GS14-GC14 (D)	90	ND	40453.3	599.1	2872.5	ND
GS14-GC14 (E)	120	4513.3	102030.3	1628.2	821.8	ND
GS14-GC14 (F)	156	5275.4	56966.0	457.3	2055.1	20.9
GS14-GC14 (G)	167	ND	140363.6	21914.5	41758.6	194.5
GS14-GC14 (H)	200	ND	34405.5	1133.4	525.0	ND
GS18 ROV28 BC3	17	ND	7202.9	141.9	88.3	ND

Table 5.2: Barium, magnesium, manganese, and titanium content of samples GS14 A - H and BC3, as determined by ICP-OES analysis. Sample ID and depth are listed below, and not detected ions are listed as ND.

Concentration					
Sample ID	**Depth (cmbsf)**	**Ba**	**Mg**	**Mn**	**Ti**
GS14-GC14 (A)	15	2159.4	42363.3	795.1	1468.3
GS14-GC14 (B)	33	4389.3	71587.5	802.3	1481.4
GS14-GC14 (C)	54	491.0	20093.5	1042.1	2803.4
GS14-GC14 (D)	90	1996.9	73697.1	534.7	207.9
GS14-GC14 (E)	120	2432.4	74770.7	929.5	620.4
GS14-GC14 (F)	156	528.6	98609.4	1392.6	395.5
GS14-GC14 (G)	167	11365.8	51993.5	812.8	31.0
GS14-GC14 (H)	200	5407.4	110044.8	995.9	968.9
GS18 ROV28 BC3	17	15300.5	8752..4	147.5	571.0

5.3 Pore fluid geochemistry

The fig.5.4 and fig.5.5 represent the pore fluid profiles from the GS14 core. No pore fluid analyses have been analysed on the BC3 sediments due to little material available. The pore fluid profiles are presented on fig.5.4 and fig.5.5, the profiles show depth in cmbsf and concentration of SO_4^{2-}, H_2S, CH_4, NH_4, NO_3, Mn, Fe, Cu, Ni, and Zn. Canfield and Thamdrup (2009)'s classification scheme for geochemical environments was used in the selection of which data to present. The classification scheme is an idealized overview of the different geochemical reaction zones in deep-sea sediments. SO_4^{2-}, CH_4 and H_2S profiles were selected based on Lin et al. (2017)'s studies about AOM in the sediments.

SO_4^{2-}, H_2S and CH_4 are plotted next to each other to visualize the trends in fig.5.4. The

SO_4^{2-} pore fluid profile shows an almost linear trend through the sediment core. The SO_4^{2-} concentrations decrease slightly from 28 μM to 27 μM (fig.5.4 A). The CH_4 pore fluid profile has high concentrations in the 30 cmbsf horizon (8.0 nM) and the 200 cmbsf horizon (13.1 nM) in the GS14 core (fig.5.4A). The interval from 60 cmbsf to 180 cmbsf shows stable CH_4 concentrations from 2.4 ppm to 5.0 ppm. The H_2S pore fluid profile has large variations through the GS14 core. The overall trend shows an increase in the H_2S concentration (fig.5.4B). The total organic carbon (TOC) pore fluid profile show a wide range of concentrations from 2.48 g/kg to 0 g/kg. The overall trend of TOC concentration is decreasing with depth (fig.5.4C).

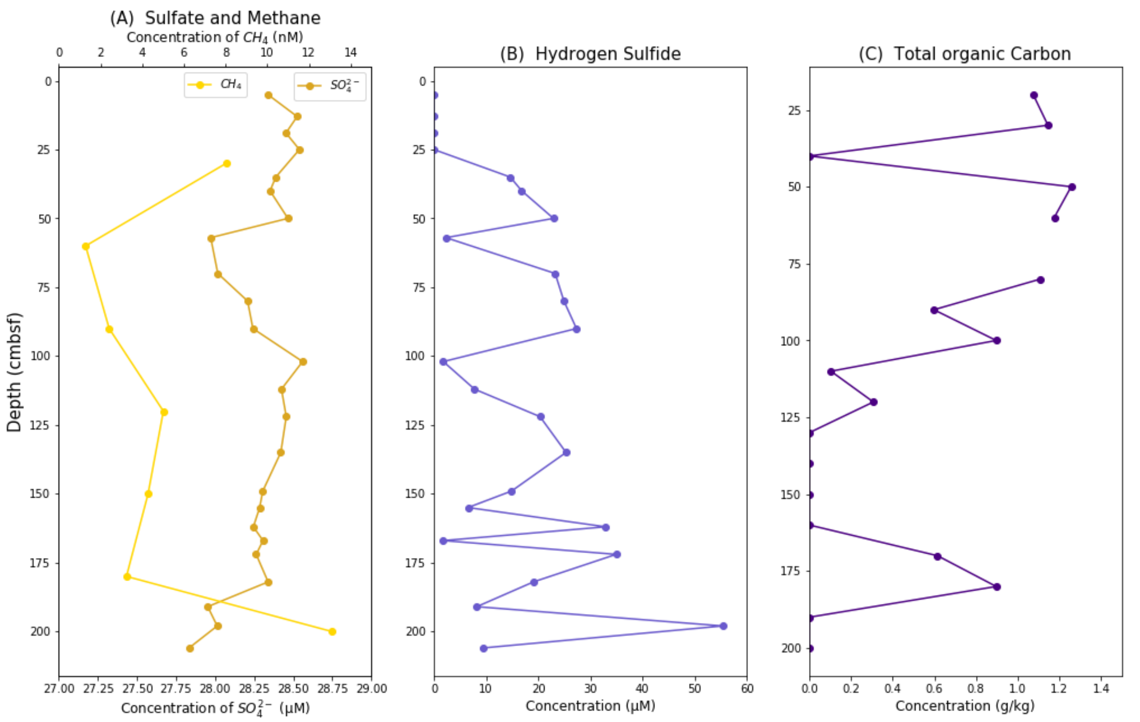

Figure 5.4: Pore fluid profiles are from the GS14 core. A) SO_4^{2-} in dark yellow and CH_4 in light yellow. Concentration of CH_4 in nM is located on the top of the graph, and the concentration of SO_4^{2-} is located at the bottom. The overlap between CH_4 and SO_4^{2-} can be seen at approximately 180 cmbsf. B) Pore fluid profile of H_2S in µm. Despite the change in concentration, the overall trend is increasing downwards. C) TOC in g/kg displays similar changes in concentration as H_2S, though the overall trend is decreasing downwards. The error bars does not exceed the symbols.

Pore fluid profiles for Mn, NH_4, NO_3, Fe, Cu, Ni and Zn are illustrated in fig.5.5. The NH_4

concentration is increasing downwards from 29 μM in the 5 cmbsf horizon to 79 μM in the 206 cmbsf horizon (fig.5.5B). The concentration of NO_3 decreases downwards in the GS14 core, starting at 2.16 μM in the 5 cmbsf horizon and decreasing to below the detection limit in the 13 cmbsf horizon (fig.5.5B). The concentration of Fe remains at 0 ppm with one exception being in the 50 cmbsf horizon. In the 50 cmbsf horizon the concentration of Fe peaks and increases to 0.12 ppm (fig.5.5A). The lack of Fe in the pore fluid profile is expected due to the reducing environment in the barite field (Steen et al., 2016; Baumberger, 2011; Eickmann et al., 2020). The concentration of Mn in the 5 cmbsf horizon is at 0.15 ppm, the Mn concentration decreases afterwards to 0.9 ppm in the 206 cmbsf horizon. The Mn concentration peaks in the 191 cmbsf horizon with a concentration of 0.20 ppm (fig.5.5 A).

The metal pore fluid profiles are showing a similar trend as the sediment geochemistry profiles (fig.5.5C). The pore fluid profiles of Cu, Ni and Zn concentrations show a consistent trend downward until the 155 cmbsf horizon. In the 155 cmbsf horizon the Cu, Ni and Zn concentrations peaks. A second peak in the metal concentrations happens in the 165 cmbsf horizon. The increases in concentrations are supported by the ICP-OES data, where Cu, Ni and Zn occurs in high concentration in the 167 cmbsf horizon. The Ni concentration show consistent 0 ppb values until the two peaks in concentration in the horizons (fig.5.5C). In the 5 cmbsf horizon the Zn concentration is at 15 ppb before decreasing to 0 ppb followed by the peaks. The Zn concentration is increasing in concentration in the 206 cmbsf horizon of the GS14 core (fig.5.5C). The Cu concentrations are higher compared to the Zn and Ni concentrations in the GS14 core. The Cu concentration is consistent from 0 cmbsf to the 155 cmbsf horizon, and vary from 10 ppb to 15 ppb. The concentration in Cu peaks to 61.34 ppb in the 155 cmbsf horizon (fig.5.5 C).

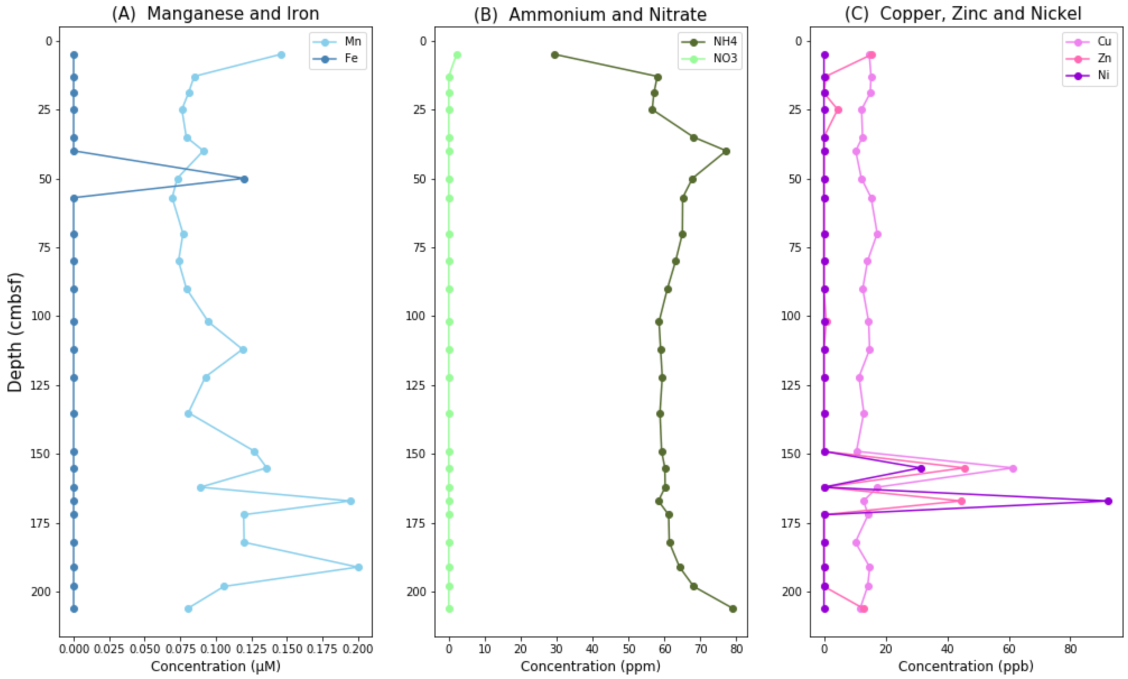

Figure 5.5: Pore fluid profiles are from the GS14 core. A) Concentrations in ppm of Mn and Fe in pore fluid from the sediment core. Mn is represented in lighter blue while Fe is represented in darker blue. B) Pore fluid profile of the concentrations of NH_4 *and* NO_3 *in ppm.* NH_4 *is represented in deeper green while* NO_3 *is represented in lighter green. C) Concentrations of metals in pore fluids, with Cu as the light purple, Zn as pink, and Ni as dark purple. The error bars does not exceed the symbols.*

Pore fluid profiles of magnesium concentration and the sulfate reduction rate (SRR) in the GS14 core is visualized in fig.5.6. The SRR highest rates can be found in the 30 cmbsf horizon and the 90 cmbsf horizon, with rates at 93.0 $pmolcm^{-1}d^{-1}$ and 73.6 $pmolcm^{-1}d^{-1}$, respectively (fig.5.6). The magnesium concentration ranges between from 1200 ppm to 1900 ppm, with an average of 1212 ppm (fig.5.6).

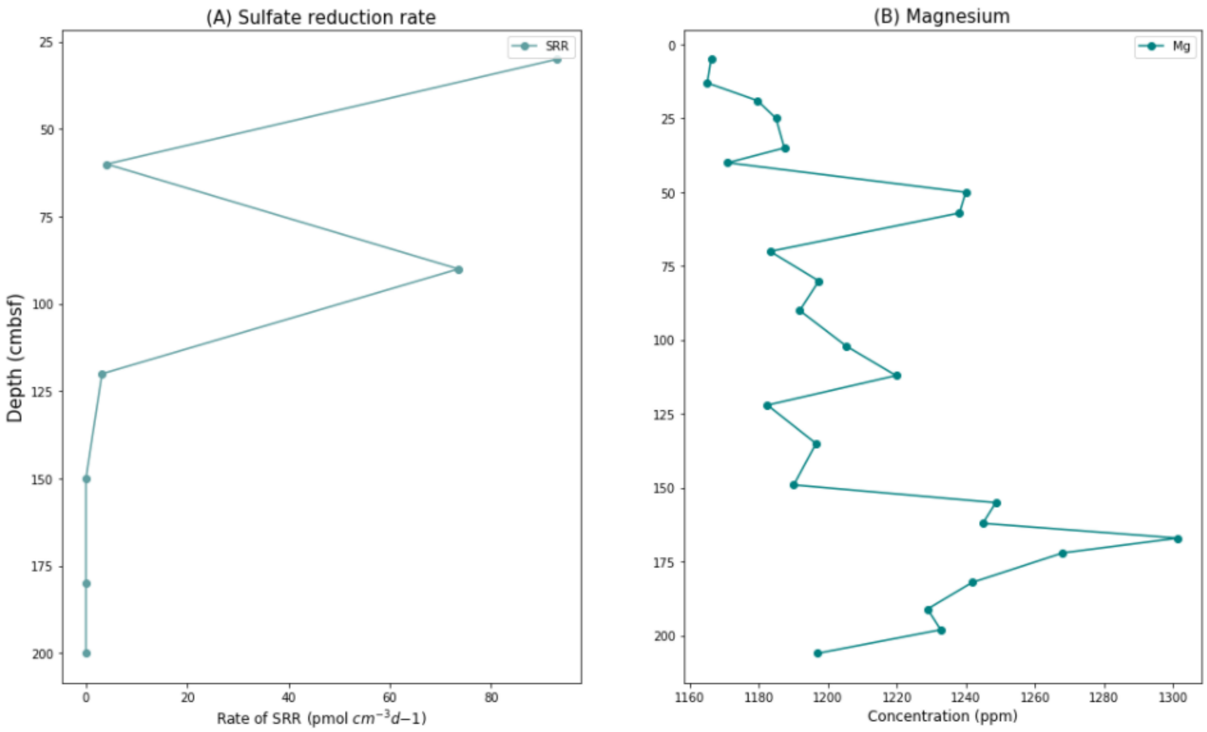

Figure 5.6: Pore fluid profiles are from GS14 core. A) The sulfate reduction rate in the GS14 sediment core. B) the concentration of Mg in pore fluids in the GS14 sediment core. The error bars does not exceed the symbols.

5.4 Relative abundance of microorganisms in GS14

Fig.5.7 and fig.5.8 shows the relative abundance of the microorganism in the sediment core GS14. No microbial data is available from the BC3 core. The SEEP-SRB1 is the dominating genus of the AOM related microorganism (5.7), while bacteria is the dominating domain in the sample overview and Rhodospirillales being the dominating order (5.8).

5.4.1 Overview of SR-AOM related microorganisms in GS14-GC14

Two families and one genus related to the SR-AOM process were detected in the GS14 core. The two families were ANME-1a and Desulfobulbaceae, and the genus was SEEP-SRB1. ANME-1a is weakly present in the 200 cmbsf horizon with a relative abundance of 0.06%. The Desulfobulbaceae was detected in three horizons, the 90 cmbsf, 150 cbmsf and the 180 cmbsf horizons. The relative abundance of Desulfobulbaceae was 0.02%, 0.05% and 0.86%, respectively. The genus SEEP-SRB1 is abundant in the 90cmbsf horizon with a relative abundance of 16.88%. SEEP-SRB1 is the ANME's major partner, and it is expected to find ANME and SEEP-SRB1 together. One potential explanation about the SRB/ANME unbalance is the primers used for amplification missed the ANME-1 sequences. The universal primers used can be prone to target one group over the other, and it is, therefore, unpredictable.

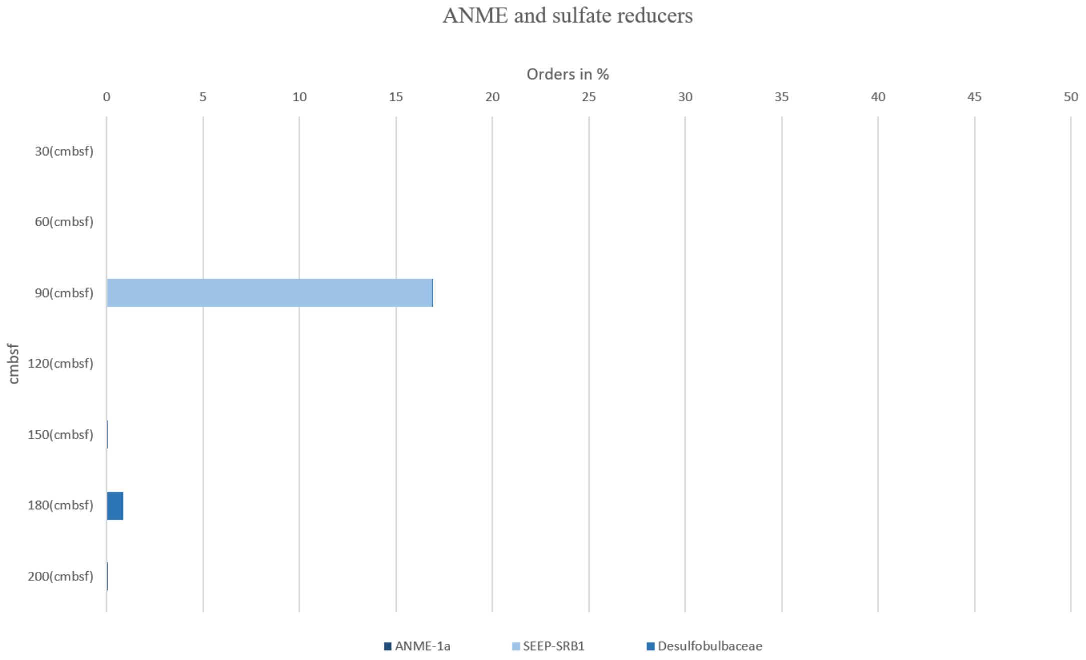

Figure 5.7: ANME-1a and sulfate reducing bacteria present in the GS14-GC14 sediment core. Dark blue is ANME-1A, blue is Desulfobulbaceae, and light blue is SEEP-SRB1.

5.4.2 Overview of microorganisms in GS14

The fig.5.8 below represents an overview of all the microorganisms in the GS14 sample with higher than 5% abundances in one horizon. The microorganisms are in order level. Rhodospirillales is the dominating order through the sediment core, except for in the 90 cmbsf horizon where Burkholderiales is dominating. The Xanthomonadales has a high abundance in the 30 cmbsf and 60 cmbsf horizons, with 14.9% and 16.5%, respectively.

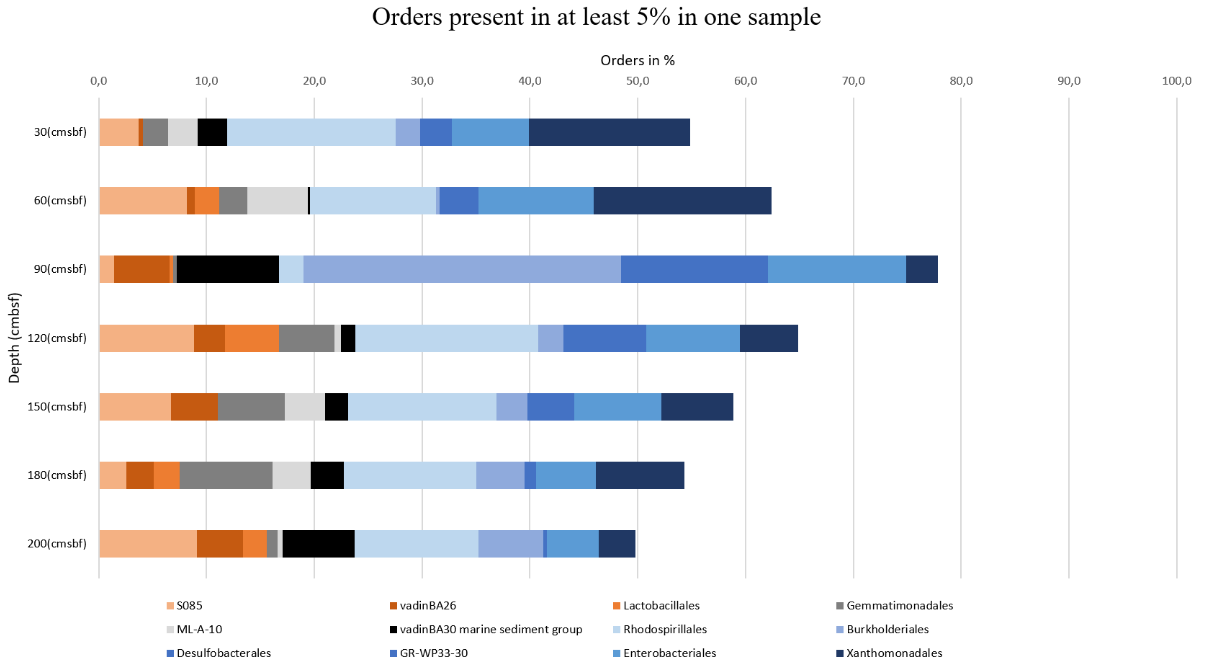

Figure 5.8: An overview over all orders present in at least 5% in the GS14sediment core.

5.5 Sulfur isotope results

For sulfur isotopes, the values are normalized to the IAEA-S1 standard relative to the V-CDT. The IAEA-S1 standards are defined with δ^{34}S = -0.300‰, δ^{33}S = -0.055‰, and δ^{36}S = -1.37‰. δ^{33}S and δ^{36}S are calculated following Ono et al. (2007)'s method, afterwards Farquhar et al. (2000) method was used to determined Δ^{33}S and Δ^{36}S with (eq.13):

$$\delta^{3x}S - 1000 * ((1 + \delta^{34}S/1000)^{X-1}) \tag{13}$$

where X is 0.515 or 1.9, respectively. The uncertainties of 2σ are from the IAEA-S1 measurements; the uncertainties are 0.09‰, 0.017‰, and 0.331‰. The fig. 5.9 and fig. 5.10 show δ^{34}S and Δ^{33}S plotted against each other and δ^{34}S's variation downwards in the sediment core.

5.5.1 Sulfur isotopic composition

Fig.5.9 has Δ^{33}S and δ^{34}S plotted against each other. The isotopes from BC3 is placed to the right side of the y-axis, and the isotopes from the GS14 core is located to the left of the y-axis (fig.5.9). The isotopes from the GS14 core is varying from -3.47‰ to -21.68‰ for δ^{34}S, and from 0.019‰ to 0.090‰ for Δ^{33}S (fig.5.9). The isotopes for the BC3 core is at 6.1‰ and 11.6‰ for δ^{34}S, and 0.040‰ and 0.012‰ for Δ^{33}S (fig.5.9).

In the horizon 0 cmbsf to 33 cmbsf the $\delta^{34}S$ values are characterized from isotopically light values (-14.54‰ and -20.11‰) to isotopically heavy values (6.1‰ to 11.6‰) (fig.5.10). The 54 cmbsf horizon exhibit $\delta^{34}S$ values that slightly vary between -3.47‰ to -7.09‰ down to the 167 cmbsf horizon (fig.5.10). In the 200 cmbsf horizon the δ^{34S} values decrease to -12.68‰ (fig.5.10).

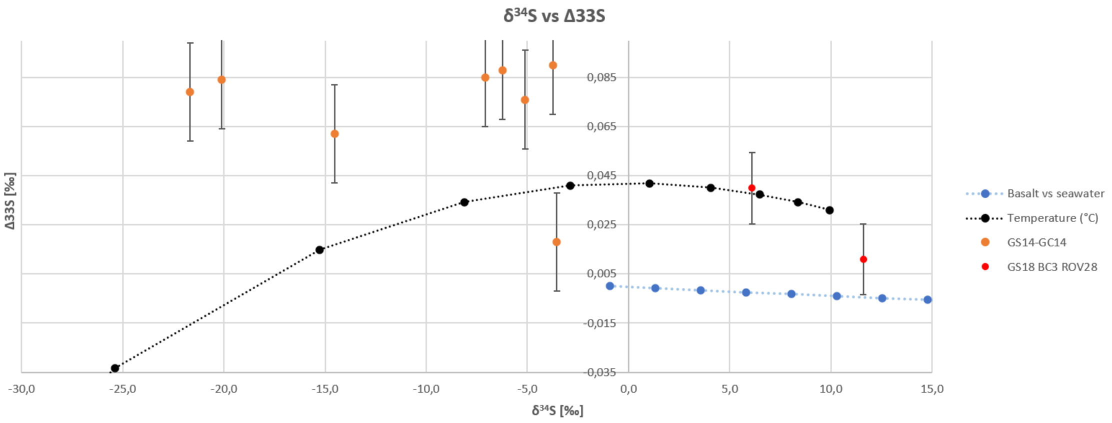

Figure 5.9: The orange dots are the results from the GS14 core, and the red dots are from the BC3 core. The black dashed line is temperature indication, and the blue dashed line is sea water isotopes versus mantle isotopes. The temperature model and two-component mixing model are both copied from Ono et al. (2012) model. The uncertainties (2σ) are taken from the IAEA-S1 measurements and are 0.09‰ for δ^{34}S, the uncertainties is too small to be seen on the figure.

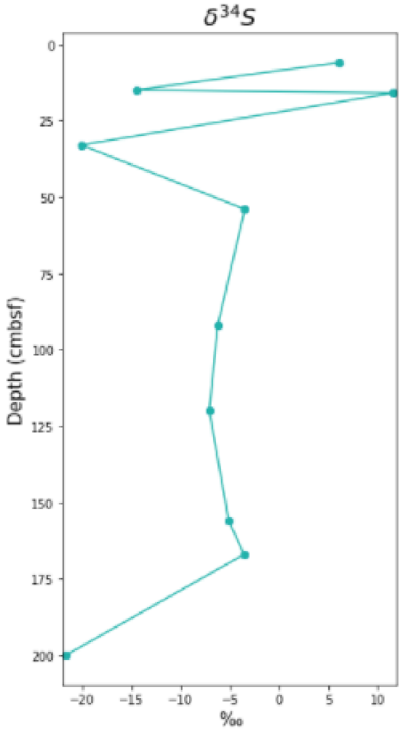

Figure 5.10: Sulfur isotopic composition of $\delta^{34}S$ of pyrite downwards in both GS14 and BC3. The uncertainties (2σ) are taken from the IAEA-S1 measurements and are 0.09‰ for $\delta^{34}S$, the uncertainties is too small to be seen on the figure.

5.6 Iron isotope results

For δ^{56}Fe isotopes, the values are calculated using the IRMM-014 standard. The average is at 0.32‰, the standard deviation with 1σ is 0.07‰, the standard error of mean is 0.04‰ and the 95% confidence interval is at 0.12‰. The uncertainty of 2σ relative to the IRRM-014 is 0.07‰, 0.011‰, 0.012‰, and 0.014‰. The fig.5.11 and fig.5.12 represents the results of iron speciation and iron isotopic composition, respectively. The iron speciation is a visual representation of the different minerals where iron is found and how much iron is extracted from the minerals. The iron isotopic composition represents how δ^{56}Fe values vary downward the GS14 core, except the 10 cmbsf horizon which is from the sample of BC3 core (fig.5.11 and fig.5.12).

5.6.1 Iron speciation

The iron speciation in the GS14 core and the BC3 core, where the 10 cmbsf horizon is from the BC3 core (fig.5.11). The average iron speciation for each species in % are Fe_{carb} = 7%, Fe_{ox} = 27%, Fe_{ox2} = 4%, Fe_{mag} = 3%, and Fe_{py} = 58%. The Fe_{py} is abundant in all horizons with one exception being the 15 cmbsf horizon. The 15 cmbsf horizon contains mostly iron oxides such as ferrihydrite and lepidicrocite (fig.5.11).

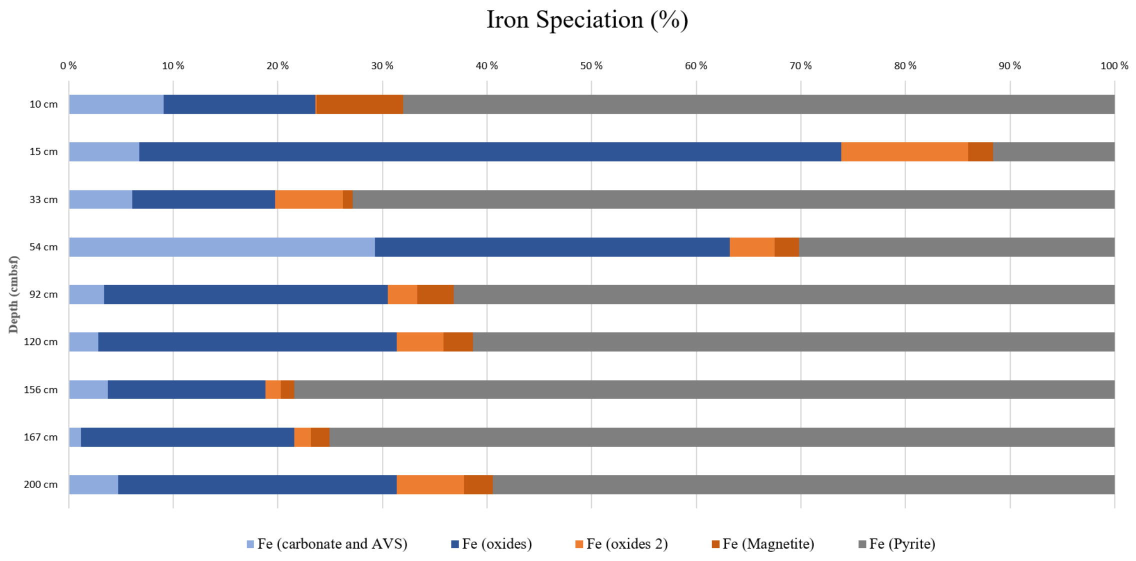

Figure 5.11: The iron speciation through the GS14 core and the BS3 core. Fe_{carb} is Fe in carbonate and AVS and in light blue. Fe_{oxides} is iron from ferrihydrite and lepidicrocite is represented in blue. $Fe_{oxides2}$ is iron from geothite, hematite and akageneite is represented in orange. Fe_{mag} is iron from magnetite, and is represented in dark orange. Fe_{pyrite} is iron from pyrite, and is represented in grey.

5.6.2 Iron isotopic composition

Fig.5.12 shows the isotopic variations of iron through the sediment core GS14 and the push core BC3. The values are ranging from -0.63‰ to 0.96‰ downwards the cores. From the 92 cmbsf horizon there is shift for the iron isotope being at 0.10‰ to more isotopically heavy isotopes at 0.78‰ and 0.68‰ in the 120 cmbsf and 156 cmbsf horizons, respectively fFig.5.12). In the 167 cmbsf horizon the iron isotopes have decreased to isotopically light values at -0.54‰, before increasing in the 200 cmbsf horizon to 0.24‰ (fig.5.12).

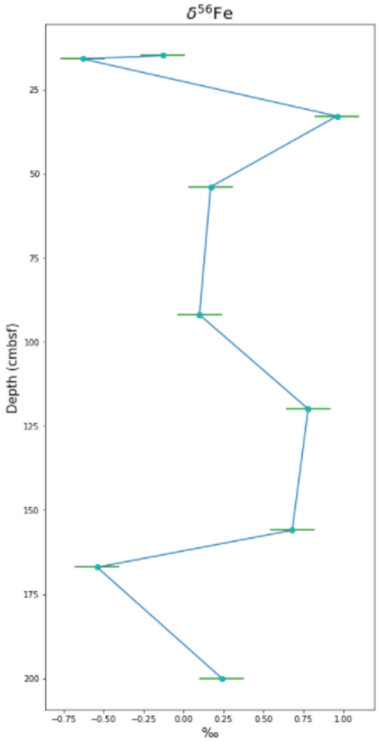

Figure 5.12: Iron isotopic composition of $\delta^{56}Fe$ *of pyrite downwards in both GS14 and BC3. The uncertainties (*2σ*) are taken from the IRMM-014 measurements and are 0.14 for* $\delta^{56}Fe$

6 Discussion

The barite field is characterized with a diluted and chemically modified version of the high-temperature fluids from Loki's Castle (Stam, 2010). The high-temperature fluids are characterized with high values of H_2S, CH_4, CO_2, H_2, and NH_4^+ (Baumberger, 2011). The Bear Island Fan is located in close proximity and contributes with carbon-rich-sediments to the hydrothermal system, causing elevated concentrations of NH_4^+ (Baumberger, 2011; Baumberger et al., 2016). The diluted high-temperature fluids interact with emanating seawater in the barite field sediments. The interaction fuels the microbial community in the sediments, chimneys, and on the surface. The microorganism oxidizes and reduces the different electron donors and acceptors, together with abiotic processes.

The barite field is covered in white "cotton", with hydrothermal chimneys emitting fluids at 20°C (Steen et al., 2016; Eickmann et al., 2020). The temperature makes it possible for many microorganisms to thrive. The white cotton is sulfur-oxidizing bacteria; the chimneys are the habitat for both anaerobic and aerobic microorganisms; and the sediments are the habitat for mainly anaerobic microorganisms (Steen et al., 2016). High values of organic matter are added to the sediments, increasing the intensity of methane production. Sulfate from seawater and the sulfur-oxidizing bacteria is added to circulation in the sediments, making the barite field sediments a good location to study the AOM-SR reaction and possible find a connection to paleo-AOM.

6.1 Pyrite morphology evidence for AOM-SR

The BC3 core contains more pyrite and more framboidal pyrite than the GS14 core, while the GS14 core contains more octahedral pyrite. The GS14 core contains some framboidal pyrites, but the main pyrite morphology is octahedrons. The octahedrons that were found in clusters indicate the start of framboidal pyrite, meaning it could convert to a framboidal pyrite with time (fig.5.2) (Lin et al., 2016b). The amount of pyrite formed in sediments is controlled by three factors; the supply of organic carbon, the amount of reactive iron, and the concentration of dissolved sulfate in pore fluids (Wilkin et al., 1996). The GS14 core contains high amounts of organic carbon, reactive iron and dissolved sulfate, meaning that the environment is suitable for pyrite growth. The BC3 core does not have pore fluid profiles, however, the amount of pyrite from the BC3 core indicates that there were no limitation of organic carbon, reactive iron and dissolved sulfate. The amount of pyrite can perhaps tell us something about the microbial activity. Lots of pyrite indicates a more intense microbial activity, which means that the microbial community in the BC3 is denser than the community in the GS14 core. The amount of pyrite and their crystal habit might be related to the growth time in the sediments.

Well-developed euhedral pyrite crystals indicate slow growth over time which means that the pyrite from both cores have developed slowly over time (fig.5.1 and fig.5.2) (Wei et al., 2016). The pyrite morphology from the BC3 and GS14 samples are limited to framboidal pyrite and octahedron-shaped pyrites. The formation of framboidal pyrite requires more growth time compared to the formation of octahedrons, since the framboidal pyrite is dependent on the merging of crystals to get the rounded shape (Wei et al., 2016; Wilkin et al., 1996). That means the pyrite from the BC3 core have had a longer growth time compared to the GS14 core, since the BC3 core contains more framboidal pyrite. The growth time is dependent on the pyrite formation that happens in four stages: The first is the nucleation of iron monosulfide microcrystals. The second is the reaction of iron monosulfide to the unstable mineral greigite. The third is the merging of the greigite crystals into a densely packed framboidal shape. Forth is the conversion of the greigite to a pyrite framboid (Wei et al., 2016; Wilkin et al., 1996). The conversion and growth of pyrite does not usually stop after the pyrite framboid is made, overgrowth can be an indication of high concentrations of H_2S and organic matter.

No overgrowth was observed in the samples, however, it does not rule out the possibility of overgrowth. Overgrowth is common deeper into the sediments as long as; organic matter, sulfate. and reactive iron is available in the sediment (Wilkin et al., 1996). The pore fluid profiles do indicate that TOC, sulfate, and sulfide are available throughout the whole GS14 core, meaning that overgrowth might have occurred but was not observed (fig.5.4). In the BC3 core it is assumed that TOC, sulfate and sulfide was available due to the amount of pyrite produces, and hence overgrowth might have been observed if a deeper core was studied. Despite no observations of overgrowth, the different pyrite sizes did vary in both cores.

The framboidal pyrite size from the BC3 and GS14 cores varied from $4\mu M$ to $10\mu M$ indicating "anoxic" environment. Pyrite formation happens in oxic and anoxic environments, the different environments can affect the framboidal pyrite size. In an oxic environment, the growth time is longer than in anoxic environment, since the growth time is dependent on the suspension of pyrite because of the hydrodynamic unsteadiness (Wilkin et al., 1996). The pyrite from anoxic environments is smaller and has a narrower size of framboidals compared to pyrite from oxic environments (Wilkin et al., 1996). In "anoxic" environments the maximum size is approximately $15\mu M$, while the framboidal size can be up to $40\mu M$ in "oxic" environments (Wilkin et al., 1996). The framboidal size does correlate to the pore fluid profiles, where oxygen is being consumed above the surface, meaning that the sediments exhibits an "anoxic" environment. The environment is not solely representative for pyrite, but the background sediments might be indicators of the "anoxic" environment.

The background sediment of the BC3 differs from the GS14 (fig.5.3), and the main difference is that the BC3 sediment contains more barite. The difference is visible when using SEM on the BC3 samples and the samples from the GS14 core, the GS14 core contains mostly silica-bearing minerals. The ICP-OES analysis confirmed the higher values of barium in the samples compared to the GS14 core (table.4.2). Comparing the 15 cmbsf and 33 cmbsf horizons to the BC3 horizon at approximately the same depth, the barium concentration is higher in the BC3 core. The barite content indicates that the depth does not affect the barite content and that the barite field is heterogeneous. The difference in mineralogy might, therefore, be explained by the different locations of the BC3 core and the GS14. The BC3 was sampled in the middle of the barite field, while the GS14 core has a GPS uncertainty meaning that the GS14 core might have been sampled at the edge of the barite field. Regardless, the BC3 core and GS14 core is not samples in the same spot, which indicates that the barite field sediment vary through the whole area.

Pyrite is the end product of the sulfur and iron cycling in the sediments, the pyrite is demonstrative of the local environment in the sediments. The environmental conditions are reflected in the pyrite's isotopic composition of iron and sulfide. Very little fractionation occurs in the pyrite formation, so the processes from before are preserved. This makes pyrite an excellent tracer, and combined with isotope data can give an insight into the processes behind the formation of pyrite and possibly the AOM-SR reaction (Lin et al., 2016a).

6.2 Geochemical evidence for AOM-SR

The geochemical evidence for AOM-SR can be found in the pore fluid profiles from the GS14 core, and the data from ICP-OES from the GS14 core and the BC3 core. The BC3 core contains less amount of the different elements than the GS14 core, only barium and strontium have higher values in the BC3 core (table.4.1 and table.4.2). The reason for that might be related to the areas of the barite field where the different cores where sampled. To be able to compare marine sediments to hydrothermal sediments, it is advantageous to start with identifying the geochemcial zones based on Canfield and Thamdrup (2009).

The pore fluid profile of Mn indicates that Mn reduction occurs in the sediments in the barite field. Mn concentrations are detected in small concentrations throughout the GS14 core, as the Mn concentration varies from 0.07 ppm to 0.20 ppm (fig.5.5A). The concentration of Mn is not significant, it is rather small compared to other pore fluids like SO_4^{2-}. The Mn concentration in solids vary slightly downwards the GS14 core, the rather stable concentration in the Mn solids indicates that no impactive Mn reduction is occurring with depth (table.4.2). The geochemcial name of the zone where Mn reduction occurs is the "manganous" zone (fig.5.5A). The "manganous" zone is characterized as the accumulation of Mn in the pore fluids and the pore fluid profiles of Mn shows an increase in the Mn concentration with depth (Canfield and Thamdrup, 2009). The Mn concentration reflects the reducing environment in the barite field sediments, and it was not expected to find high concentrations of dissolved Mn in the pore fluids (Baumberger, 2011; Eickmann et al., 2020). Mn occurs deep into the sediments without being depleted by any reactions occurring deeper (fig.5.5A). the BC3 core contain less Mn compared to the GS14 core, however, the difference is not distinct and it is assumed that little Mn reduction is occurring in the BC3 core. The reducing environment does not solely affect Mn, but other elements such as Fe is affected.

The reducing environment is further proven by the lack of dissolved Fe throughout the GS14 core (fig.5.5A). A peak in Fe concentration can be observed, but the peak of dissolved Fe is not interpreted to represent the "ferruginous" zone. The concentration of dissolved Fe is at 0.12 ppm in the 50 cmbsf horizons, and the concentration is too little to regard as a possible "ferruginous" zone. Regardless, dissolved Fe can not accumulate in the presence of H_2S, and H_2S is present through most of the core (fig.5.4B). The reaction between H_2S and dissolved Fe happens quickly and it should not be possible to detect any accumulation of dissolved Fe (S.L Jørgensen 2022, personal communication, 17 January). The ICP-OES data shows high values of Fe in the 54 cmbsf horizons, and so it would be expected a decrease in Fe concentration if Fe reduction happened in the 50 cmbsf horizons (table.4.1C). The ICP-OES indicates that Fe is present in mineral phases, such as iron sulfides, iron carbonate, and iron phosphates (Canfield and Thamdrup, 2009; Lin et al., 2016b). Hence, the peak might be an analytical artifact, however, it is not possible to conclude or dismiss the peak of Fe. The BC3 core contain less Fe in solids, which can mean that most of the Fe is dissolved and can be found in pore fluids. However, that theory is not likely as it is assumed that H_2S is present in the sediments. Another explanation can be that the BC3 core contain more pyrite, but less other iron-bearing minerals, meaning that the total concentration of Fe in the BC3 core is less than the GS14 core. After the "ferruginous" zone it is expected to find the "sulfidic" and the "methanic" zones.

The "sulfidic" zone and the "methanic" zone are the last zones to occur, and it is difficult to identify either zone based on the pore fluid profiles and ICP-OES data. A "sulfidic" zone would be visible in pore fluids with the depletion of SO_4^{2-}, however a definite depletion does not occur in the GS14 core (fig.5.4A). The SO_4^{2-} is seemingly unaffected by any reactions in the sediments. The ICP-OES data of sulfur shows numerous horizons with non-detectable sulfur (table.4.1). The lack of detectable sulfur can be explained by the acid used in the preparation for ICP-OES analysis. If the samples contain insoluble sulfides, the samples are exposed to Aqua Regia, an acid mixture of HCL and HNO_3. The acids can dissolve sulfide and sulfates, and affect the analyses of sulfur. The sulfide and sulfates will precipitate and therefore it is not possible to detect the sulfur in the ICP-OES analyses. The "methanic" zone in sulfate-rich systems will be defined as the SMTZ. In the SMTZ a consortium of microorganisms will mediate the reaction of methane with sulfate through anaerobic methane oxidation (Canfield and Thamdrup, 2009; Lin et al., 2016a, 2017). The lower bounds of the “methanic” zone can stretch deep into the sediments, as the energy landscape is not favorable for microorganisms and there are no electron acceptors to react with methane (Canfield and Thamdrup, 2009).

Originally, the first zone to be identified is the "oxic" zone, however, that is not the case in the barite field. The "oxic" zone is not possible to identify from the pore fluid profiles as the oxygen is rapidly being removed by the microbial mat of sulfur oxidizers at the surface (F Vulcano 2022, personal communication, 15 February) (Steen et al., 2016). The oxygen is being used in the oxidization of H_2S from the pore fluids, hence most of the oxygen is removed before it enters the surface sediments. Canfield and Farquhar (2012*a*)’s geochemical classification is used as starting point while examining the geochemical data from the cores. The Geochemical classification is an idealized version of the reactions occurring in deep-sea sediments. Based on Canfield and Thamdrup (2009) classification scheme for geochemical environments only the "manganous" zone can be identified. This means that hydrothermal sediments does not follow the "standard" reactions as marine sediments are following, meaning that other processes might vary and the evidence of AOM-SR in hydrothermal sediments is different from marine sediments.

6.2.1 The Bear Island Fan’s influence on AOM-SR

Sediments from the Bear Island Fan affects the hydrothermal input to the barite field with elevated concentrations of NH_4^+, CH_4, Sr (Baumberger et al., 2016; Baumberger, 2011; Eickmann et al., 2020). The pore fluid concentration of NH_4^+ has an average of $61.49\mu M$, the CH_4 has an average concentration of 4.0nM, and the Sr concentration has an average of 7.62ppm. The concentrations indicates elevated values and confirms the sedimentary input from the Bear Island Fan (Baumberger et al., 2016; Baumberger, 2011; Eickmann et al., 2020). The sedimentary input is most likely affecting the geochemistry in pore fluids and solids in the barite field, and potentially intensifying the AOM-SR reaction in the barite field sediments. Elevated concentrations of NH_4^+ is caused by the sedimentary input and affects the barite field sediments.

The ratio between NH_4^+ and SO_4^{2-} from core GS14 indicates that methane is oxidized via sulfate reduction (fig. 6.1). The lower concentration of NH_4^+ from the GS14 core can then be interpreted as a lack or lower rate of decomposition of organic matter. The SO_4^{2-}/NH_4^+ ratio strengths the theory of a lower rate of decomposition of organic matter since the ratio indicates that the AOM-SR reaction occurs as the main process. This discovery contradicts Eickmann et al. (2020) findings, as Eickmann et al. (2020)'s results indicated that degradation of organic matter were the dominant process in the barite field sediments. Eickmann et al. (2020)'s pore fluid profile of NH_4^+ differs from the pore fluid profile of NH_4^+ from the GS14 core. The NH_4^+ from the GS14 core have an average concentration of $61.49\mu M$, and the Eickmann et al. (2020)'s NH_4^+ concentrations averages on $500\mu M$. The high concentration of NH_4^+ is interpreted as a result of decomposition of organic matter due to the interaction between ascending hydrothermal fluids and sub-seafloor sediments (Eickmann et al., 2020). It is not farfetched that different cores lead to different results, however, the huge difference in concentration might not be simply explained by heterogeneous sediments. Other factors such as the rate and intensity of the ascending hydrothermal fluids might affect the sediments together with the circulating seawater, as well as fractures and faults in the barite field. Dissolved Mg from the pore fluid profile can indicate how much the high-temperature fluids affect the sediments.

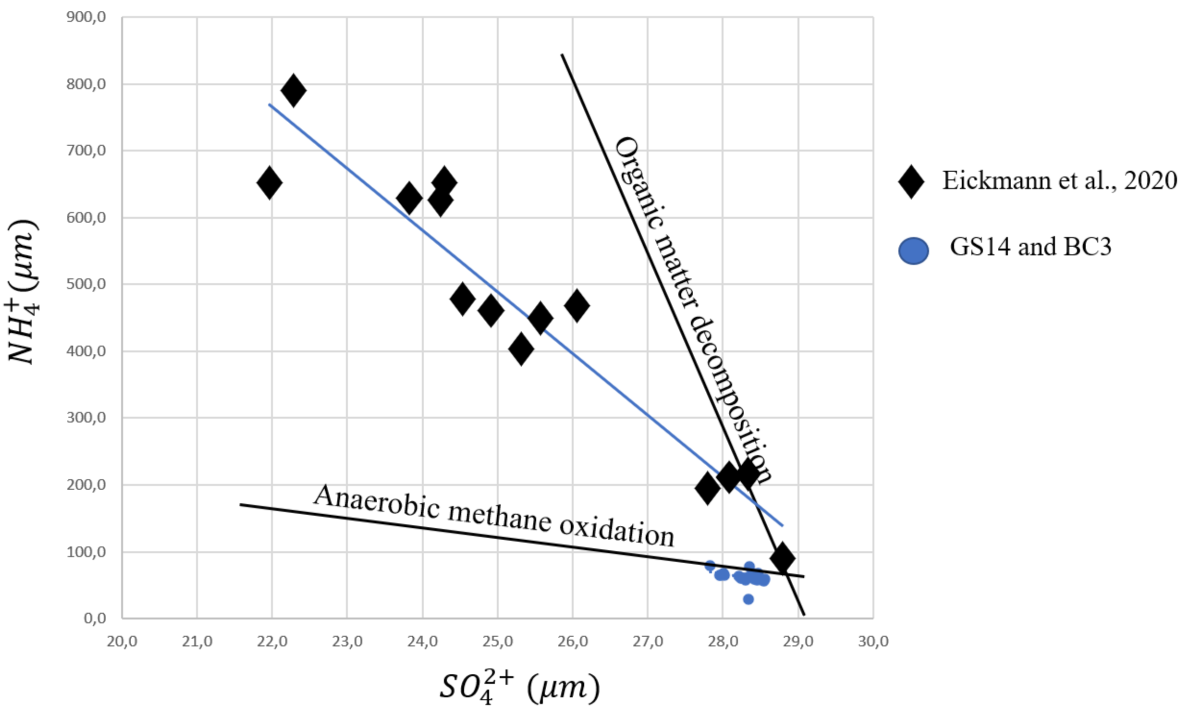

Figure 6.1: The relationship between NH_4^+ and SO_4^{2-} indicates clearly anaerobic methane oxidation in the sediments from the barite field, the samples from GS14 and BC3 is in blue. The model is modified from Greinert et al. (2002) and Eickmann et al. (2020). Black diamonds represents Eickmann et al. (2020)'s result from the barite field.

The concentration of Mg in the pore fluids indicates mixing of ambient seawater with zero Mg from high-temperature vent fluids (Eickmann et al., 2020). The pore fluid concentration of magnesium (Mg) shows near ambient seawater (SW = 52.3 mmol/L or 1271 ppm), but the Mg concentration is slightly below the ambient seawater (GS14 = 49.9 mmol/L or 1212 ppm) (fig5.6 (Eickmann et al., 2020). The Mg circulating in the high-temperature vent field is removed during water-rock interactions, leading to zero Mg from high-temperature black smokers. When the zero Mg from high-temperature vent fluids mixes with seawater the concentration of Mg will be lowered compared to the seawater. The mix of ambient seawater and high-temperate zero Mg fluids matches the result that Eickmann et al. (2020) have, and it strengthen the proof that the barite field is affected by high-temperature vent fluids mixing with ambient seawater. The seawater-rock interactions results in the formation of Mg-OH silicates, and high concentrations of Mg in sediments are as expected (table.4.2) (Baumberger et al., 2016; Eickmann et al., 2020). Another consequence of the high-temperature input is an increase in pH causing a reducing environment in the sediments (Baumberger, 2011).

The low Mn and Fe values in pore fluids is due to the reducing environment, and the pH at Loki's Castle is 7-8. The pH is elevated due to the influence from the sedimentary input source (Baumberger et al., 2016). The pH leads to the reduced solubility of sulfide minerals, which affects the precipitation of sulfides and oxides, and lowers the concentration of Mn and Fe in solution (Baumberger et al., 2016). Fe in pore fluids are non-existent and the Mn concentration in the pore fluid is low (fig.5.5A). However, the concentrations of Fe and Mn in sediments are higher (table.4.1), Fe varies between 7020.9 ppm to 142993.7 ppm and Mn varies between 147.5 ppm to 1042.1 ppm. The concentration in sediments indicates that most of the Fe and Mn are in solid form, such as oxides and silica minerals (fig.5.3).

The Bear Island Fan is situated 5 km northeast of Loki's Castle in the rift valley. The distal part of Bear Island Fan reached Loki's Castle vent field about 1.3-1.5 million years ago (Pedersen, et al., 2013). The hydrothermal system is not directly covered in sediments, with the sediments covering the axial volcanic ridge (AVR). It is believed that the sediments are buried below or within the AVR, and from there interact with the hydrothermal circulation(Baumberger, 2011; Baumberger et al., 2016). Baumberger et al. (2016) studied boron (B) and strontium (Sr) isotopes from the fluids at Loki's Castle. Baumberger et al. (2016) have isotope signatures that cannot be explained by seawater-MORB alone, indicating that sedimentation impacts the hydrothermal circulation and presumably the barite field sediments (Baumberger et al., 2016). B is commonly found in sediments with organic matter, having elevated values of B means that there is the supply of organic matter to the hydrothermal circulation (Baumberger et al., 2016). The supply of organic and inorganic matter will affect the microorganisms and fluids at Loki's Castle. The high-temperature fluids will react with the organic matter in the sediment, causing thermogenic degradation, oxidation of organic matter, and dissolution of $CaCO_3$ (Baumberger et al., 2016). The reaction leads to an enrichment of NH_4^+, CH_4, Sr and Ca compared to sediment starved systems, and elevated concentrations of K, B, alkalinity, and pH (Baumberger et al., 2016). The pore fluids does not follow the same geochemistry profiles as deep-sea sediments, and the sedimentary input source might be one of the reasons why. The difference in geochemistry might affect where in the sediments the AOM-SR occurs and how it affect pore fluids, isotopes and microorganisms.

6.2.2 Pore water-related to AOM-SR

The CH_4 concentration originates from the reduction of organic matter in the sediments. The CH_4 concentration fluctuate through the GS14 core, but the concentration is at its highest in the 200 cmbsf layer before decreasing to the 175 cmbsf layer. The sudden decrease is an indicator of consumption of CH_4 through the AOM-SR. The decrease of CH_4 in pore fluids is interpreted to where the current SMTZ is located. SMTZ starts at approximately the 175 cmbsf horizons and ends at the bottom of the core at the 200 cmbsf horizons (fig.5.4A). It is uncertain if the SMTZ continue downwards, the uncertainty is caused by the lack of proof of a definite decrease of SO_4^{2-} concentration. The identification of the SMTZ is based on Lin et al. (2016a, 2017)'s paper where they identify an overlap between CH_4 and SO_4^{2-} as the current SMTZ. The pore fluid profiles show a definite decrease in CH_4 concentration, but the SO_4^{2-} concentration barely decreases from $28\mu M$ to $27\mu M$ downward. The decrease in SO_4^{2-} concentration is not impactful and it is uncertain if the decrease will continue downwards. Tiny variations in the concentration of SO_4^{2-} are visible through the pore fluid profile and it is not possible to conclude with a definite decrease (fig.5.4A). The decrease in SO_4^{2-} concentrations can reflect consumption of SO_4^{2-} by microbial sulfate reduction, or variations by different mechanisms. The accumulation of CH_4 in the bottom horizon happens accordingly to Canfield and Thamdrup (2009)'s pore fluid profile. The CH_4 defuses upwards and meets the descending SO_4^{2-} from seawater and microorganisms. When the CH_4 meets the descending SO_4^{2-} fluids the AOM-SR reaction starts and a decrease of CH_4 is expected. The reaction between CH_4 and SO_4^{2-} in marine sediments cause an linear trend in SO_4^{2-} and it is expected to find a similar trend in the hydrothermal sediments.

The AOM-SR causes an almost linear trend in SO_4^{2-} concentration (fig.5.4A) (Lin et al., 2016a, 2017). The SO_4^{2-} concentration does fluctuate slightly through the GS14 core, and there is no clear reduction of in SO_4^{2-} concentration. In marine deep-sea sediments the SO_4^{2-} is usually removed from the pore fluids by two possible processes; firstly being reduced by organic matter during OSR, and the second by oxidation of methane. Lin et al. (2016a, 2017) discovered that OSR usually causes a downward concave SO_4^{2-} pore water profile, while AOM causes a linear decrease (Lin et al., 2016a, 2017). OSR can be ruled out as an option as SO_4^{2-} pore fluid profile does not show a concave trend. The linear trend is easier to argue for, as the SO_4^{2-} concentration does decrease slightly with depth. However, it would be necessary to have a deeper sediment core to possibly note a more definite decrease in SO_4^{2-} concentration. Any attempts to plot a linear trend line did result in low R values and was not included in this thesis. AOM-SR is most likely the dominant process in sediments where SO_4^{2-} and CH_4 meet. With the small changes in SO_4^{2-} concentrations, another SO_4^{2-} reduction process is not likely to be occurring (Canfield and Thamdrup, 2009). However, it is possible other input sources supplies with SO_4^{2-} to the sediments. A potential flux of SO_4^{2-} can originate from sibolind tubeworms and sulfide oxidizing bacteria (Steen et al., 2016). The sibolind tubeworms and sulfide oxidizing bacteria are to be found over the surface sediments, and both oxidize sulfide to SO_4^{2-}. The constant concentration of SO_4^{2-} can not explained the fluctuations in CH_4, TOC, and H_2S.

The fluctuation in CH_4, TOC, and H_2S can be related to different processes occurring at the different depths in the GS14 core. The CH_4 is not visible before 30 cmbsf due to not being measured in the sediments above. The reason for not measuring the CH_4 concentration in the upper bounds of the GS14 core is most likely because it is not expected to find CH_4 higher up. Loki's Castle high-temperature vent field is known for high H_2S and CH_4 concentrations (Baumberger, 2011). The black smoker Joao is in close proximity to the barite field and is most likely impacting the barite field with increasing values of CH_4 and H_2S (Baumberger, 2011; Eickmann et al., 2020). However, the influence from the black smoker Joao can not solely explain the fluctuation in concentrations. It is clear that the high-temperature fluids affects the sediments in the barite field, however, the fluctuation in concentration of CH_4, TOC, and H_2S is most likely related to AOM-SR and degradation of organic matter. Meaning that both processes occurs in several sediment horizons, causing the fluctuation in the H_2S concentrations.

AOM-SR is the main cause of the increase in H_2S concentrations in the GS14 core (Lin et al., 2016a, 2017). The H_2S increases and fluctuates throughout the GS14 core, H_2S reaches its maximum concentration in the bottom layer of the core (fig.5.4 B). The H_2S concentrations vary through the GS14 core, which can indicate that the intensity of the AOM-SR reaction varies through the GS14 core. However, the decreases in CH_4 pore fluids together with the increases in H_2S pore fluid concentration most likely means that AOM-SR is occurring in the sediments. The H_2S will lead to the precipitation of iron monosulfide in the presence of microorganisms. Iron monosulfide is not stable and will continue to react to form pyrite (Lin et al., 2017, 2016b). The increase of H_2S in the 200 cmbsf horizon supports the theory of the location of the current SMTZ, combined with the decrease in TOC content. The TOC content is fluctuating through the core, the fluctuation might be a result of the supply of TOC to the sediments from the Bear Island Fan.

The decrease in TOC content indicates production of methane and it is supported by the pore fluid profiles (fig,5.4) (Lin et al., 2016a, 2017). The TOC content displays a similar pattern to the H_2S pore fluid profile. The TOC content fluctuates through the GS14 core, however, the overall trend is decreasing. The TOC content reaches zero concentration in two horizons, the 40 cmbsf and 190-200 cmbsf horizon, in the same horizons that the CH_4 concentration is increasing. This observation leads to the assumption that methane is being produced in these horizons. The H_2S concentration does increase in the bottom sediments, however it does not increase in the 40 cmbsf horizon. What happens above the 40 cmbsf to the surface sediments is unknown. The CH_4 might be consumed before reaching the surface sediments, or it might diffuse upwards into the seawater column. The varying content of TOC in the sediments might indicate that the AOM-SR reaction occurs in different horizons through the GS14 core, supporting the same theory as the H_2S concentrations. In the SMTZ zone, the TOC content is not detectable, indicating that methane is being produced in the SMTZ zone. The production of methane is supported by the high concentration of methane in the same horizon. The decrease is most likely a result of the reaction between TOC and H_2O in the sediments causing the production of methane (Canfield and Thamdrup, 2009). Methane's density is higher than its surroundings, the density will cause an upwards diffusion of methane. It is expected that in areas where the reduction of TOC occurs is where methane is produced.

The AOM-SR process can be identified from pore fluid profiles of SO_4^{2-}, CH_4 and H_2S. Lin et al.

(2016a, 2017) and Eickmann et al. (2020) identify several indications of AOM-SR in pore fluid profiles. Some of the characteristics are based on AOM-SR from deep-sea sediments unaffected by hydrothermal fluids. The first being the depletion of SO_4^{2-} and CH_4 concentration with the increase of H_2S concentrations. The barite field sediments shows fluctuation in the pore fluids CH_4 and H_2S, however the bottom sediments from the GS14 shows clear indications of the AOM-SR evidence similar to marine sediments (Eickmann et al., 2020; Lin et al., 2016a, 2017). The SO_4^{2-} concentration is deviating from expected values from sediments where AOM-SR occurs. Alone, the concentration of SO_4^{2-} points towards sediments unaffected by AOM-SR reaction. However, the SO_4^{2-} concentration might be affected by other input sources than seawater, which leads to the atypical pore fluid profile. The $NH4$ and SO_4^{2-} correlation clearly indicate that AOM-SR is the main process in the GS14 core. To summarize the geochemistry of the barite field, the low-temperature fluids display a diluted version of the high-temperature fluids (Greinert et al., 2002; Baumberger et al., 2016; Steen et al., 2016).

6.2.3 High-temperature related horizon

The 167 cmbsf horizon exhibits high-temperature related metals indicating a hydrothermal origin. The metals copper (Cu), zinc (Zn), and nickel (Ni) increases in concentration in the 167 cmbsf horizon, before decreasing the horizons below. The metals concentration were low and steady through the GS14 core until the 167 cmbsf horizon (fig.5.5C). The ICP-OES values display a similar pattern where the Cu, Zn and, Ni values show increasing concentrations in the 167 cmbsf horizon (table.4.1). Another strong indicator that the metals origin are from high-temperature fluids are the depletion in titanium (Ti). Ti is a metal connected to low-temperate fields, and it is not expected to find high values of titanium in high-temperature vent fields (table.4.2). The Ti values are slightly decreasing downward, but the concentrations suddenly drops in the 167 cmbsf horizon before it increases in the 200 cmbsf horizon. Pore fluids combined with ICP-OES indicates that the 167 cmbsf horizon is original from a hydrothermal chimney or hydrothermal debris. The barite field is a low-temperature area with a temperature of about 25°C (Steen et al., 2016; Eickmann et al., 2020; Baumberger, 2011). In the barite field it is not expected to find elevated values of metals, and since the layers above and below the 167 cmbsf is seemingly unaffected and shows values related to low-temperature area it is natural to conclude that the metals originates from the black smoker.

6.3 Comparison of geochemical and microbiological data

The orders presented in fig.5.8 are mainly anaerobic microorganism, with some orders without any information, which includes ML-A-10, vadinBA30 marine sediment group, and Rhodospirillales. However, since some of the orders are strictly in anoxic environments it is assumed that the unknown orders are anaerobic.

The main microorganisms in the GS14 core are sulfate reducers or nitrate reducers. The Desulfobacterales is mainly sulfate reducers, while Burkholderiales, Xanthomondales and Enterobacteriales are all connected to the nitrogen cycle as nitrate or nitirte reducers (Mandal, 2018; Palleroni and Bradbury, 1993; Lonvaud-Funel, 2014; Imhoff, 2005). The nitrate from the pore fluid profile does become depleted quickly in the top layer of the GS14 core (fig.5.5). The Xanthomonadales and the Rhodospirillales are the most abundant orders in the 30 cmbsf horizon, with Xanthomonadales being abundant in the 60 cmbsf horiozon as well. Indicating that the nitrate and nitrite reduction occurs in the 0 to 60 cmbsf horizon (Mandal, 2018; Palleroni and Bradbury, 1993; Lonvaud-Funel, 2014; Imhoff, 2005). The microbial overview allows a broad picture of the main groups of microorganisms in the GS14 sediments, but the microbial data do not allow coupling ANME to the AOM-SR or ANME's sulfate reducing partners. The identification of the SMTZ is difficult as well, since the ANME present in the bottom sediments core is very dense and lacks SRB. In AOM-SR affected sediments it is excepted to find dense communties of ANME since they are closely related to the oxidation of CH_4 (Steen et al., 2016; Knittel and Boetius, 2009).

The detection of ANME was likely inefficient due to the primers used for the 16S rRNA amplicons generation. This methodological could be be overcome by using other primers prior testing their sensitivity towards microbes of the group ANME. For future studies it can be necessary to use Archaeal and Bacterial specific primers or test different universal primers.

6.3.1 The presence of ANME and sulfate reducing bacteria in 90 cmbsf horizon

The abundance of SEEP-SRB1 in the 90 cmbsf horizon indicates active sulfate reduction (fig.5.7). The geochemistry in the 90 cmbsf horizon indicates AOM-SR due to the presence of the SEEP-

SRB1, an anaerobic sulfate reducer (Steen et al., 2016; Knittel and Boetius, 2009). The sulfate reduction happens despite the lack of consumption of SO_4^{2-} from the pore fluids (fig.5.4A). In the 90 cmbsf horizon the SEEP-SRB1 has a relative abundance of 16.87% (fig.5.7). It is expected an increase in H_2S when SO_4^{2-} is reduced and a decrease in CH_4 concentrations. In the 90 cmbsf horizon the pore fluid profiles of H_2S is increasing and CH_4 is decreasing, both showing signs of sulfate reduction coupled with methane oxidation (fig.5.4A and B). The stable SO_4^{2-} concentrations can perhaps be explained by the mats of sulfide oxidizing bacteria and/or burrowing animals such as sibolinid tubeworm that reside on the surface sediments (Steen et al., 2016; Tarnovetskii et al., 2018). The sibolinid tubeworm releases SO_4^{2-} through their roots planted into the top layer of the sediments, while the sulfide oxidizing bacteria produces SO_4^{2-} through oxidizing sulfide, as follows (eq.14) (Dahle et al., 2015; Steen et al., 2016; Tarnovetskii et al., 2018):

$$H_2S + 2O_2 \rightarrow HSO_4^- + H^+ \tag{14}$$

The hypothetical increase the SO_4^{2-} from the worms and the bacteria to the sediments, means the flux of SO_4^{2-} can be higher than the consumption through AOM-SR. The sulfide oxidizing bacteria called Sulfurimonas, and the sibolind tubeworm has colonized the barite field, affecting the SO_4^{2-} concentration (Steen et al., 2016). The SEEP-SRB1 is important because of its relationship with ANME.

SEEP-SRB1 is a genus of the Deltaproteobacteria (Knittel and Boetius, 2009). SEEP-SRB1 is often associated with ANME-1 and ANME-2 archaea, and ANME-2 is the main partner to SEEP-SRB1 (Knittel and Boetius, 2009; Steen et al., 2016). SEEP-SRB1 form aggregates with the ANME-2, however, it is not possible to say that ANME-2 is the obligated partner to SEEP-SRB1 (Knittel and Boetius, 2009; Schreiber et al., 2010). Since it was impossible from the 16S rRNA survet to determine where AOM-associated microbes were most abundant, the depth of the SMTZ could be indirectly inferred using geochemical data. However, the detection of the SEEP-SRB1 does mean that sulfate reduction is occurring in the same horizon where methane is present, it is then assumed that the main reaction in the 90 cmbsf horizon is AOM-SR.

6.3.2 The presence of ANME and sulfate reducing bacteria in 200 cmbsf horizon

ANME is present in a low abundance in the 200 cmbsf horizon, the abundance of ANME is 0.06% in the bottom horizon (fig.5.7). The geochemistry in the 200 cmbsf horizon suggests CH_4 oxidation and SO_4^{2-} reduction (fig.5.4A). The possibility is based on the decrease of CH_4 concentration upwards and the decrease in the SO_4^{2-} concentrations downwards in GS14 core (fig.5.4A). The possible decrease in SO_4^{2-} concentration can not be detected without a longer sediment core. The SO_4^{2-} concentrations shows tiny variations downward the core, and it is therefore difficult to explain the decrease as evidence for sulfate reduction (fig.5.4A). However, the H_2S reaches its highest concentration in the 200 cmbsf horizon. The high concentrations of H_2S strongly indicates sulfate reduction (fig.5.4B). The 200 cmbsf horizon indicates methanogenesis due to the high concentration of CH_4 and the not detectable TOC values, despite ANME being detected alone (fig.5.4A and C).

Despite the lack of ANME and their partners, previous studies Steen et al. (2016) showed that the sediments in the barite field has growth conditions favorable for anaerobic methane oxidizers instead of aerobic sulfide and methane oxidizers (Steen et al., 2016). This theory is supported by the lack of oxygen in the sediment core and as well as the sulfide oxidizers above the sediments (Steen et al., 2016). ANME has also been detected in the barite chimneys and in the sediments in the barite field, however their sulfate reducing partner SEEP-SRB1 was detected in small amounts (<0.1%). This indicates that ANME-1 might be free-living (Steen et al., 2016). The free-living ANME-1 can be an explanation for the lack of SEEP-SRB1 in the 200 cmbsf horizon. Another explanation can be that the primers excluded the sulfate reducing partner of ANME-1, and therefore might not be indicating any free-living ANME-1 (Steen et al., 2016). However, the possibility of free living ANME is more likely since the primers used did detect SEEP-SRB1 in the 90 cmbsf horizon and indicated small amounts of it in the 150 cmbsf horizon.

ANME is divided into three groups known as ANME-1, ANME-2 and ANME-3, and all three groups are directly associated with the AOM-SR process (Knittel and Boetius, 2009; Steen et al., 2016). ANME can occur from the first decimeters to meters below the sediment surface, depending on the CH_4 and SO_4^{2-} flux into the sediments (Knittel and Boetius, 2009; Steen et al., 2016). Hence, it is not uncommon to find ANME at different depths depending on the area. The sediments needs to be anoxic since oxygen is highly toxic to ANME (Knittel and Boetius, 2009). The oxygen concentration is below the detection limit in the GS14 samples, since mats of sulfide oxidizing bacteria consume most of oxygen before entering the sediments. Due to the presence of ANME in the bottom sediments of the GS14 core, it is assumed that AOM-SR occurs in this horizon. Detecting SRB and ANME in the sediments is important as it can indicate where to expect AOM-SR occurring, and help with the interpretation of the isotopes.

6.4 Isotopic evidence for AOM-SR

Sulfur and iron isotopes can be the key to track paleo-AOM in hydrothermal sediments. The expected results for sulfur will be biological affected isotopes with negative $\delta^{34}S$ values and positive $\Delta^{33}S$ values. However, the iron isotope signature from pyrite is something few others have studied, and hence no expectations were made beforehand for the iron isotopes. Lin et al. (2016b)'s paper about iron isotopes from pyrites showed an enrichment of $\delta^{56}Fe$ with depth. The sediment cores GS14 and BC3 deviate from the cores presented in Lin et al. (2016b, 2017)'s papers, with depth, morphology, and area. Despite the differences, it is interesting to compare the result against each other. A proxy for tracing AOM-SR with iron isotopes has not yet been discovered, a proxy is something that would helpful while studying AOM-SR since AOM-SR is not easily distinguished from OSR. The geochemistry in the area is an indicator for AOM-SR, and sulfur isotopes can be used to determine if S in pyrite originates from abiological and biological processes. However, other processes can affect geochemistry, while pyrites from OSR have a biological background. Finding the proxy for iron can help with the understanding of the AOM-SR.

6.4.1 Sulfur isotopes related to AOM-SR

The isotopes from the GS14 core indicate a typical biological signature. A typical biological signature is characterized with negative $\delta^{34}S$ values and positive $\Delta^{33}S$ values, and based on Eickmann et al. (2014)'s figure the isotopes is mostly placed with in the *in-situ* biogenic area (fig.6.2). The $\delta^{34}S$ values throughout the GS14 core shows variation at the very top from the surface layer to the 35 cmbsf layers before stabilizing and becoming significantly more negative in the 200 cmbsf horizons (fig.5.10). The variation in the sulfur isotopes can be related to the microbial activity in the different horizons, a denser population of sulfate reducers will lead to an enrichment of heavier isotopes. The microorganisms prefer isotopically light isotopes during metabolic processes and will consume the ^{32}S, leaving a pool of SO_4^{2-} enriched in ^{34}S and depleted in ^{32}S isotopes (Eickmann et al., 2020; Jørgensen et al., 2004). However, if the reduction of SO_4^{2-} continues, the isotopic signature will change towards heavier isotopes, due to the light isotopes being consumed already. A heavier isotopic composition is expected in AOM-SR from marine sediments, since most of the ^{32}S isotopes have been depleted from the SO_4^{2-} pool and the SMTZ usually occur deep into the sediments, meaning that OSR have already depleted the ^{32}S relative to the original isotopic composition. Lin et al. (2016a, 2017) figured a higher rate lead to an increase in isotopic composition towards heavier one. In the barite field's hydrothermal sediments, OSR is unlikely to occur, and hence it is not expected to find a similar increase with depth as Lin et al. (2017) found. However, it is expected high sulfate reduction rates (SRR) in the horizons where the heavier $\delta^{34}S$ is located.

The SRR have seemingly not affected the sulfur isotopes from the GS14 core. The SRR is high in two horizons, the first being the 30 cmbsf horizons and the second being the 90 cmbsf horizons (fig.5.6A). The $\delta^{34}S$ isotopes are unaffected by the high SRR in the 90 cmbsf horizons. The isotopes in the 90 cmbsf horizons do not differ from those above or below. In Lin et al. (2017)'s paper, the $\delta^{34}S$ values become increasingly heavier with depth together with an increase of the SRR. However, in the GS14 core the heavier isotopes are located in the middle of the core, from 54 cmbsf to 156 cmbsf, while the SRR increases from 60 cmbsf and have decreased by 120 cmbsf. The enrichment of heavier isotopes can be explained by the higher SRR in the same horizon, however it is not a clear relationship between the heavier isotopes and the SRR. In comparison, the $\delta^{34}S$ isotopes in the 30 cmbsf are very isotopically light, being seemingly unaffected by the high SRR in the same horizon. It is possible that the SRR is not accurate and do not represent the actual SRR from the GS14 core, however, that will remain a speculation. With high SRR it is assumed the presence of a high population of sulfate reducing bacteria (SRB) in the same horizons.

The SRB is present in the 90 cmbsf horizon together with high SRR, indicating active sulfate reduction (fig.5.7 and fig.5.6). The $\delta^{34}S$ isotope in the correlation horizon is at -6.23‰, and it is bordering between *in-situ* biogenic and hydrothermal areas (fig.6.3). It is be expected that the $\delta^{34}S$ isotope from the 90 cmbsf horizon did display a heavier isotopic composition, since the SRR is the highest in this horizon. However, that is not the case for the GS14 core. SRB is not detected in the horizons above or below the 90 cmbsf horizon, which can be explained by the probe not detecting the SRB or ANME in the sediments. The isotopic signature clearly indicates biogenic origin and it is assumed that SRB and ANME is the main cause for the biogenic signature of the sulfur isotopes. The biogenic signature is important due to the connection with the AOM-SR and paleo-AOM, finding SRB and ANME makes it easier to understand the isotopic composition. However, it is a possibility that ANME drives the AOM-SR reaction alone, which would lead to a different isotopic composition of pyrite (Steen et al., 2016).

The lack of SRR and SRB in the 200 cmbsf horizons can indicate that ANME-1 is working without their SRB partner. The 200 cmsbf horizon is characterized with isotopically light $\delta^{34}S$, high concentration of CH_4 and H_2S. Pore fluid profiles and isotopes indicate the AOM-SR reaction; however, it is only possible to identify the ANME-1 in the 200 cmbsf horizons. The SRB is identified in the 90 cmbsf horizons and assuming that no analytical errors occurred, it would be expected to find SRB in the 200 cmbsf horizons. ANME-1 is identified alone and can indicate that Steen et al. (2016) was correct regarding ANME-1 not being dependent on SRB. Again, the problem with the probes can be the main issue and hence the result discussed is not comparable to the actual microbial community in the GS14 core. Moreover, studies have shown that AOM-SR combined with a deep H_2S sink can lead to isotopically heavy $\delta^{34}S$ (Lin et al., 2016a, 2017; Borowski et al., 2013; Peketi et al., 2012). The isotopes in the 200 cmbsf horizons contradict Lin et al. (2017) theory about the enrichment of heavier isotopes downwards; however, it is comparable to Eickmann et al. (2020)'s findings. Eickmann et al. (2020) who studied isotopes from the barite field could also show isotopically light values in the bottom of the core. That means the enrichment of isotopically heavier isotopes might occur in marine sediments not affected by a hydrothermal input such as the barite field. In the hydrothermal sediments the different flux rates of SO_4^{2-} changes the isotopic composition.

The $\delta^{34}S$ isotopes have a high-temperature hydrothermal origin in the 167 cmbsf horizons. A hydrothermal origin normally means positive $\delta^{34}S$ and $\Delta^{33}S$ values, in contrast to the biological affected signature, which shows negative $\delta^{34}S$ values. The $\delta^{34}S$ values in the 167 cmbsf are not positive; however, the values do coincide with Loki's Castle sediments and the hydrothermal affected areas (fig.6.2 and fig.6.3). The $\delta^{34}S$ values from the 167 cmbsf horizons originate most likely from debris from a high-temperature chimney. The isotopic composition combined with the pore fluid profiles and ICP-OES of high-temperature related metals points towards the same conclusion.

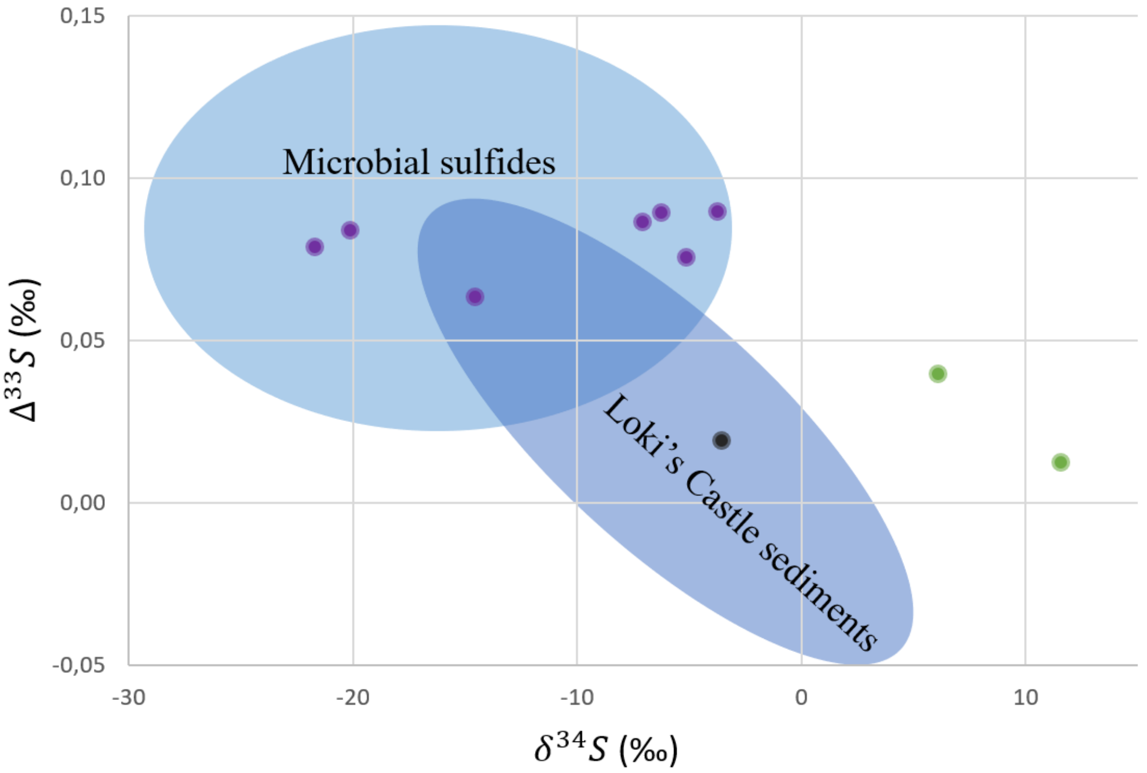

Figure 6.2: Plot of $\delta^{34}S$ versus $\Delta^{33}S$. Purple dots are isotopes from GC14, the black dot is from GC14 167 cmbsf horizon, green dots are isotopes from BC3. The model is modified from Eickmann et al. (2020).

The BC3 isotopes do not match microbial sulfide or Loki's Castle sediments, meaning that intense reduction of SO_4^{2-} is occurring (fig.6.2 and fig.6.3). The positive $\delta^{34}S$ from the BC3 core can indicate an almost total consumption of SO_4^{2-} from the pore fluids. The consumption of SO_4^{2-} can lead to an increase of $\delta^{34}S$ isotopes of the residual SO_4^{2-} if the consumption exceeds the replenishment (Crémière et al., 2020). The $\delta^{34}S$ in sulfide will become isotopically heavier and will trend towards the original isotopic composition of seawater SO_4^{2-} (Crémière et al., 2020), and the positive $\delta^{34}S$ values can be a result of that happening. If it is a high abundance of ANME and SRB in the BC3 horizon, the AOM-SR process will be intensified due to intense methane oxidation and sulfate reduction. The ^{32}S isotopes will be consumed first, and the remaining pool will contain heavier isotopes ^{34}S (Jørgensen et al., 2004). If the consumption continues, the microorganism will mediate from the heavier isotopes. The heavy isotopes will lead the isotope signature towards a more positive composition since it will be enrichment in ^{34}S. A heavier composition is often an indication of a high SRR in the same sediments.

High SRR from the BC3 core indicates an intense reduction of the SO_4^{2-} pool. Data from Vulcano shows rates in 6-8 cmbsf with an average rate at 65270 pmol $SO_4^{2-}/cm/d$. In the second horizon from 14-16 cmbsf, the average rate is at 14828 pmol $SO_4^{2-}/cm/d$. The high SRR rates compared to the GS14 core indicates a more intense microbial reduction, and it is expected that the intense reduction can lead to $\delta^{34}S$ values closer to seawater $\delta^{34}S$ values. Another theory is a hydrothermal origin of the from 6-18 cmbsf horizon, similar to the 167 cmbsf horizons. However, the BC3 (I) sample contains small concentrations of Cu and Zn, and Ni is not detected in the sample (table.4.1). It is therefore unlikely that the $\delta^{34}S$ isotopes from BC3 originate from hydrothermal debris. The last possible explanation is the execution of the CRS method. It is possible that an analytical error happened, or the method was executed poorly. Leaking from the tubes could affect the results. However, since the samples were observed during the experiment, it is unlikely.

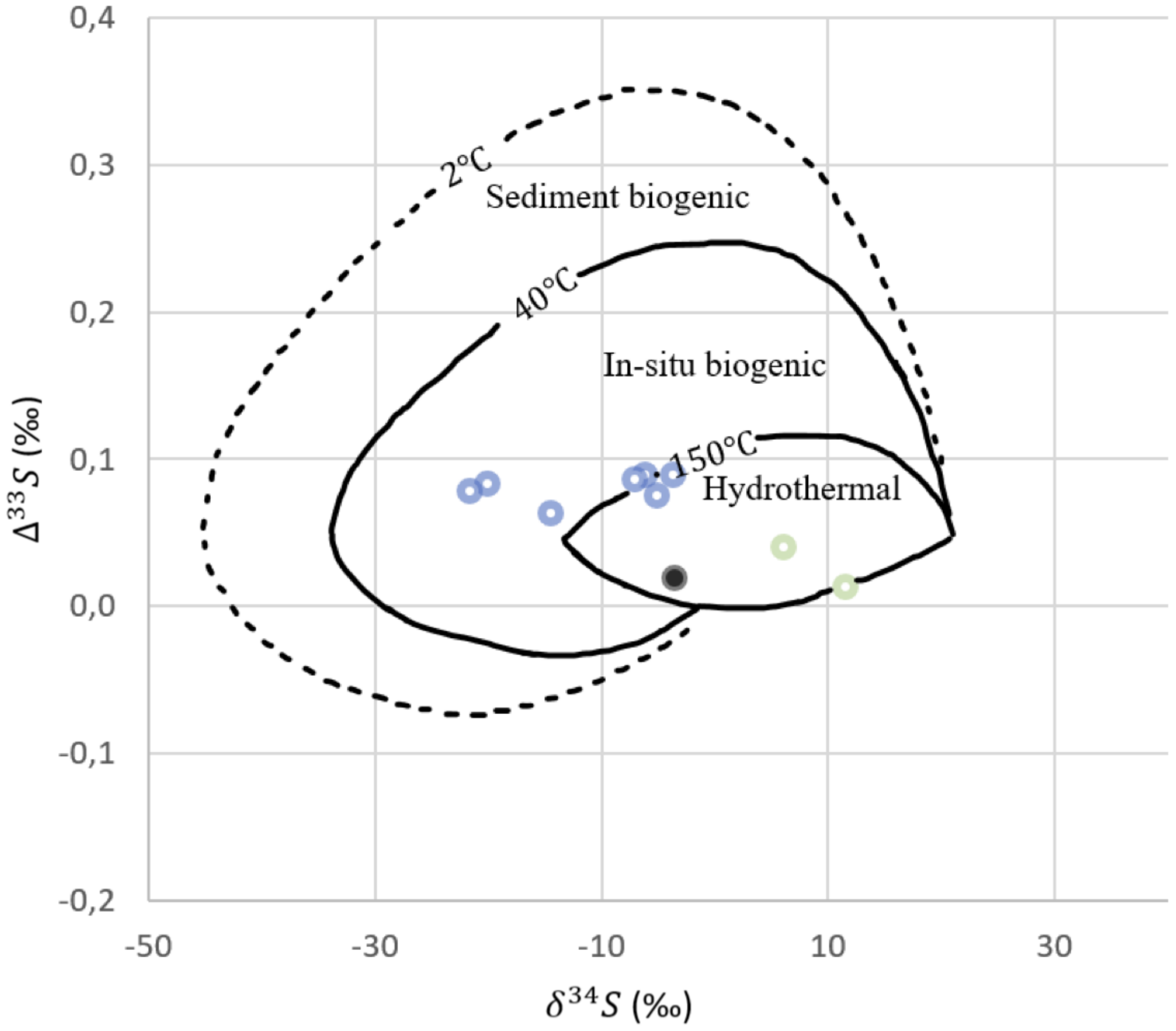

Figure 6.3: Plot of $\delta^{34}S$ versus $\Delta^{33}S$. Green dots represent the isotopes from the BC3 core. Blue dots represent the isotopes from the GS14 core, and the black dot is the 167 cmbsf horizon from GS16. The model is modified from Eickmann et al. (2014).

The $\delta^{34}S$ isotopes are usually enriched in the SMTZ compared to other sediment layers. The enrichment is not observed in the GS14 core, and it might indicate that the SMTZ is not as intense as other studies or that the circulation of SO_4^{2-} is high enough to keep the $\delta^{34}S$ isotopes negative. The SMTZ might occur higher in the BC3 zone from 6 to 20 cmbsf. The top horizon of the BC3 core has high rates of SRR, and the $\delta^{34}S$ isotopes are affected by the high rates. The high rates indicate that ANME and SRB are working together and consuming large amounts of seawater SO_4^{2-}.

However, it is difficult to say anything with certainty without microbial data and pore fluid profiles from the BC3 core. Assuming the pore fluid profiles and the microbial data from the BC3 core are different compared to the GS14 core. The different $\delta^{34}S$ values from the BC3 and GS14 cores indicate that heterogeneous sediments characterize the barite field. The heterogeneous sediments make it pointless to compare the pore fluid profiles and the microbial data from the GS14 core with the $\delta^{34}S$ isotopes from the BC3 core. Hence, comparing isotopes from the BC3 core with the geochemical data from the GS14 core is avoided.

Comparing the BC3 core and the GS14 core would have been beneficial for the sake of finding paleo-AOM, however the different isotopic compositions of the two cores makes it impossible. The barite field is heterogeneous which is affecting the isotopic composition, this indicates that hydrothermal sediments might not be suitable to study plaeo-AOM. However, the barite field is still a suitable area to study the current AOM-SR in the sediments.

6.4.2 Iron Isotopes related to AOM-SR

Any deviations from the igneous rock composition can be considered fractionation during the iron biogeochemical cycle in the marine sediments (Lin et al., 2016b; Rickard, 2012). The $\delta^{56}Fe$ values from GS14 and BC3 show variations from -0.63‰ to 0.96‰. One specific process cannot easily explain the wide range of isotopes. However, the iron isotopic composition is dependent on two things, one is the source of the dissolved Fe, and the second is the mechanisms behind the formation of the pyrite (Lin et al., 2016b). The $\delta^{56}Fe$ values might be a result of iron limitation and different mechanisms.

The source of dissolved Fe is usually isotopically light meaning that Fe in pyrite would mirror more or less the same isotopic composition (Lin et al., 2016b). However, the positive and negative $\delta^{56}Fe$ values occur randomly in the GS14 core. The fractionation factor between Fe in solid form and Fe in aqueous form is -2.10‰ to -3.00‰ (Beard et al., 2010; Johnson et al., 2005). Continuously dissolving Fe from its solid form will lead to an enrichment of heavier isotopes. When the lighter isotopes have been depleted, the heavier will be the subject of fractionation. The amount of dissolved iron in pore fluids can affect the isotopes, and iron limitation can result in heavier isotopic composition (Rickard, 2012; Severmann et al., 2006). Lin et al. (2016b) observed an increase of heavier $\delta^{56}Fe$ with depth and pyritization, but the same increase can not be observed in the GS14 core. The heavier isotopes do not show any specific trend with depth, however, the heavier isotopes might indicate local iron limitation in the sediments. The geochemistry of the GS14 core fluctuates, and it is, therefore, not unlikely that the release of dissolved iron varies in as well. This theory resembles the same theory as the sulfur isotopes from the BC3 core. However, the GS14 core also contains isotopically light Fe.

Negative $\delta^{56}Fe$ values are often related to pyrite formation. Negative values of $\delta^{56}Fe$ are commonly found in pyrite, and the range of values for sedimentary pyrite is usually very narrow (Lin et al., 2016b). The isotopically light Fe composition might reflect an environment where Fe is not an limitation and hence reflect lighter values. The last step that determined the isotopic composition is the formation of the pyrite (Lin et al., 2016b). The fractionation factor of dissolved Fe to mackinawite is +0.33‰ (Guilbaud et al., 2011), leading to a more isotopically heavier composition than the parental composition. If the source Fe is isotopically light in solid form, the dissolved Fe will be even lighter compared. The conversion to mackinawite will continue exhibiting negative $\delta^{56}Fe$ values.The conversion of mackinawite to pyrite will result in a different fractionation factor; however, the fractionation factor remains unknown.

The isotopic compositing varies too much to interpret a specific signature for AOM-SR. The wide range of isotopes can perhaps be explain by iron limitation in some horizons, however it is difficult to connect it to either AOM-SR or paleo-AOM. For the iron isotopes, more research most be done before it is possible to say anything for certain. It is possible that iron isotopes are not suited for the barite field due to the heterogeneous sediments and the reducing environments. However, it might also have been the execution of the iron extraction method, the method could have been executed incorrectly. If the sediments were not cleaned well enough between the steps, there might be some residue from the other dissolved iron species which affects the measurements. Another error can be that not all of the iron from the oxides were dissolved during the first and last steps. An analytical error could have occurred from the photo spectrometer, or a fingerprint/dust/dirt affected the measurements. The iron speciation should be able to detected possible errors.

The amount of pyrite and the $\delta^{56}Fe$ does not occur to be dependent on each other (fig.5.11 and fig.5.12). The sediment layers with an isotopically heavier composition contain approximately the same amount of pyrite as the isotopically light layers, except the 15 cmbsf horizons (fig.5.11). The amount of pyrite from the 15 cmbsf is significantly less compared to other horizons below, and iron oxides have a higher abundance (fig.5.11). Iron oxides are considered a highly reactive mineral, meaning when exposed to reduction, they will dissolve, leaving dissolved Fe in pore fluids. The dissolved Fe can be used to form pyrite if H_2S is present in the sediments. The iron oxides have not been dissolved, and the $\delta^{56}Fe$ values are -0.13‰. The explanation might be related to the lack of H_2S in the same horizon with high values of TOC, meaning that the upper layer of the GS14 core is not as redox-sensitive as the layers under the 15 cmbsf.

The $\delta^{56}Fe$ value from the 167 cmbsf horizons indicates a hydrothermal origin. The $\delta^{56}Fe$ value together with pore fluid profiles and $\delta^{34}S$ value indicates the hydrothermal origin. For iron isotopes, a hydrothermal signature would mean anything between -3.1‰ to +2.2‰ (Rickard, 2012). A specific hydrothermal signature is hard to obtain with only one sample as a reference. However, combined with the other evidence like sulfur isotopes, pore fluid profiles, and ICP-OES analyses, it is assumed that iron isotopes exhibit a hydrothermal signature

Two burned samples were included alongside the iron extraction of the GS14 sediments. These burned samples were provided to me after the ICP-OES analysis and should, in theory, only burn away the organic matter. The idea was to compare the burned and non-burned samples during the iron extraction. Unfortunately, the burned samples rarely provided any detectable iron. The detected iron concentration was little, so the burned samples were not included in the final results. However, calculating the iron speciation and comparing it to the ICP-OES data shows that the iron from the extraction was less than the ICP-OES in most samples. The ICP-OES contains Fe in silica, which was not extracted during the iron extraction. A higher concentration of Fe in ICP-OES is therefore expected. Only two horizons showed iron extraction values more elevated than the ICP-OES. The horizons in question are the 33 cmbsf and the 156 cmbsf, both showing high $\delta^{56}Fe$ values. One explanation can be that it was a user error when extracting the Fe or an analytical error. The second explanation can be that those two horizons had more Fe in the samples used for iron extraction.

Even though the samples were taken from the same petri dish, the content of Fe might not have been the same.

6.5 Limitations and future research

The study includes sulfur and iron isotope analyses, pore fluid analysis, microbial data, and concentration analysis of solid samples. The analyses allow a bigger and more complex picture of the AOM-SR in hydrothermal sediments at the barite field. The sulfur isotopes indicate that microbial sulfate reduction is actively happening in the sediments, and most of the geochemical data confirms it. The iron isotopes give a unique and different viewpoint on how fractionation of iron isotopes is affected by the AOM-SR reaction, however, it is debatable how reliable they are. The sulfur isotopes composition indicates an environment with low temperature and microbial activity. The current SMTZ is located in the bottom horizon of the GS14 core from 200 cmbsf to 175 cmbsf. AOM-SR can occur higher up in the sediments, however, it is not as intense as in the bottom sediments. It is also not possible to conclude with a specific signature of the isotopes related to paleo-AOM.

The main limitation is the constraint of pore fluid analysis and microbial data from the BC3 core. More data from the BC3 core could have led to an easier comparison between the BC3 core and the GS14 core. The pore fluid analysis could have provided an explanation of the positive $\delta^{34}S$ values. From the GS14 core the probes used for the microbial data were biased, and using different probes could have ended in a different result. Overall, more data and time were needed for both cores since the hydrothermal sediments in the barite field is heterogeneous.

Future research should look at microbial data, sulfur isotopes, and iron isotopes from different areas of the barite field. The combination of the isotopes and different areas could possibly provide a deeper understanding of the mechanisms of the barite field. Iron isotopes with the AOM-SR process are still a rather untouched subject. A comparison of iron from the ICP-OES analysis and iron extraction data did not suffice, and hence a different approach could be necessary. It would be optimal to have measured the diameters of the framboidal pyrites directly when using the SEM

(Wei et al., 2016; Wilkin et al., 1996; Lin et al., 2016a). Measuring the diameter would have made it easier to track the sizes of the pyrites in the samples, as well as calculate the median in the different horizons. Finding the median could have shown a hypothetical trend in sizes with depth. The framboidal diameter is a robust proxy for the past and present, as the frambodial growth does not progress with depth, and it is resistant towards weathering (Wilkin et al., 1996; Wei et al., 2016; Lin et al., 2016a). Adding $\delta^{13}C$ isotopes to the study could also be important for future research. The $\delta^{13}C$ isotopes will be enriched in the SMTZ, and the $\delta^{12}C$ isotopes would be enriched in the methane (Eickmann et al., 2020). The isotopically light $\delta^{13}C$ would indicate the presence of ANME and the oxidation of organic matter (Eickmann et al., 2020). Would also argue that understanding the fractures and faults near and under the barite field could provide an explanation of the heterogeneous sediments.

7 Conclusion

The main aim of the thesis was to identify geochemical evidence for the AOM-SR and the paleo-AOM in hydrothermal sediments. In this thesis, we looked at the geochemistry in the barite field, the pyrite morphology, microorganisms, and the isotopes of sulfur and iron. Based on the results and discussion, we conclude:

- The pyrite morphology is mainly framboids or octahedrons, the abundance of pyrite is connected with the intensity of AOM-SR.

- Pore fluid profiles of CH_4, H_2S, and TOC can be used to determine horizons where AOM-SR is occurring.

- The concentration of seawater SO_4^{2-} indicates an additional flux of SO_4^{2-} to the sediments.

- The SMTZ is located in the lower bounds from 175 to 200 cmbsf in the GS14 core, while it is not possible to conclude with a specific depth of the SMTZ in the BC3 core.

- The δ^{34}S values (-3.47‰ to -21.68‰) from the GS14 core is consistent with biological fractionation of sulfur. The δ^{34}S values (6.1‰ and 11.6‰) from the BC3 core is consistent with high sulfate reduction rates and total consumption of seawater SO_4^{2-}.

- Because of the opposite sulfur isotopes values it is not possible to find a specific paleo-AOM signature.

- The δ^{56}Fe values (-0.63‰ to 0.96‰) from the GS14 core is too inconsistent to interpret any reactions.

- The hydrothermal sediments in the barite field could not determine a specific AOM-SR isotope signature, and it is therefore not possible to track paleo-AOM.

References

Baumberger, T. (2011), Volatiles in marine hydrothermal systems.

Baumberger, T., Früh-Green, G. L., Dini, A., van Zuilen, C. B., Thorseth, I. H. and Pedersen, R. B. (2016), 'Constraints on the sedimentary input into the Loki's Castle hydrothermal system (AMOR) from B isotope data', *Chemical Geology* **443**, 111–120.

Beard, B., Handler, R., Scherer, M., Wu, L., Czaja, A., Heimann, A. and Johnson, C. (2010), 'Iron isotope fractionation between aqueous ferrous iron and goethite', *Earth and Planetary Science Letters - EARTH PLANET SCI LETT* **295**.

Bick, J., Dennis, J., Zylstra, G., Nowack, J. and Leustek, T. (2000), 'Identification of a New Class of 5'-Adenylylsulfate (APS) Reductases from Sulfate-Assimilating Bacteria', *Journal of bacteriology* **182**, 135–42.

Blain, S. and Tagliabue, A. (2016), *Iron Cycle in Oceans*, John Wiley Sons.

Borowski, W. S., Rodriguez, N. M., Paull, C. K. and Ussler, W. (2013), 'Are 34S-enriched authigenic sulfide minerals a proxy for elevated methane flux and gas hydrates in the geologic record?', *Marine and Petroleum Geology* **43**, 381–395.

Bottrell, S. H. and Newton, R. J. (2006), 'Reconstruction of changes in global sulfur cycling from marine sulfate isotopes', *Earth-Science Reviews* **75**(1), 59–83. ISOtopes in PALaeoenvironmental reconstruction (ISOPAL).
URL: *https://www.sciencedirect.com/science/article/pii/S0012825205001388*

Canfield, D. E. and Farquhar, J. (2012*a*), 'The global sulfur cycle', *Fundamentals of Geobiology* pp. 49–64.

Canfield, D. E. and Thamdrup, B. (2009), 'Towards a consistent classification scheme for geochemical environments, or, why we wish the term 'suboxic' would go away: Editorial', *Geobiology* **7**, 385–392.

Canfield, D. and Farquhar, J. (2012*b*), *The Global Sulfur Cycle*, pp. 49–64.

Canfield, D., Raiswell, R., Westrich, J., Reaves, C. and Berner, R. (1986), 'The Use of Chromium

Reduction in the Analysis of Reduced Inorganic Sulfur in Sediments and Shales', *Chemical Geology* **54**, 149–155.

Carbonero, F., Benefiel, A., Alizadeh-Ghamsari, A. and Gaskins, R. (2012), 'Microbial pathways in colonic sulfur metabolism and links with health and disease', *Frontiers in physiology* **3**, 448.

Cassarini, C. (2017), Anaerobic oxidation of methane coupled to the reduction of different sulfur compounds in bioreactors.

Claff, S., Sullivan, L., Burton, E. and Bush, R. (2010), 'A sequential extraction procedure for acid sulfate soils: Partitioning of iron', *Geoderma* **155**, 224–230.

Cruz, M. I. F. S. d. (2015), Mineralogy and Geochemistry of contrasting hydrothermal systems on the Arctic Mid Ocean Ridge (AMOR): The Jan Mayen and Loki's Castle vent fields, PhD thesis.
URL: *https://www.proquest.com/dissertations-theses/mineralogy-geochemistry-contrasting-hydrothermal/docview/2013316826/se-2?accountid=8579*

Crémière, A., Pellerin, A., Wing, B. A. and Lepland, A. (2020), 'Multiple sulfur isotopes in methane seep carbonates track unsteady sulfur cycling during anaerobic methane oxidation', *Earth and Planetary Science Letters* **532**.

Dahle, H., Økland, I., Pedersen, R. B., Thorseth, I. H. and Steen, I. H. (2015), 'Energy landscapes shape microbial communities in hydrothermal systems on the Arctic Mid-Ocean Ridge', *The ISME Journal* **9**.
URL: *https://doi.org/10.1038/ismej.2014.247*

Eickmann, B., Baumberger, T., Thorseth, I. H., Strauss, H., Früh-Green, G. L., Pedersen, R. B. and Jaeschke, A. (2020), 'Sub-seafloor sulfur cycling in a low-temperature barite field: A multi-proxy study from the Arctic Loki's Castle vent field', *Chemical Geology* **539**.

Eickmann, B., Thorseth, I. H., Peters, M., Strauss, H., Bröcker, M. and Pedersen, R. B. (2014), 'Barite in hydrothermal environments as a recorder of subseafloor processes: A multiple-isotope study from the Loki's Castle vent field', *Geobiology* **12**, 308–321.

Farquhar, J., Jackson, T. and Thiemens, M. (2000), 'A 33S enrichment in ureilite meteorites: Evidence for a nebular sulfur component', *Geochimica et Cosmochimica Acta* **64**, 1819–1825.

Fry, B. (2006), *Stable Isotope Ecology*, Springer, New York, NY.

Greinert, J., Bollwerk, S. M., Derkachev, A., Bohrmann, G. and Suess, E. (2002), 'Massive barite deposits and carbonate mineralization in the Derugin Basin, Sea of Okhotsk: precipitation processes at cold seep sites', *Earth and Planetary Science Letters* **203**, 165–180.

Guilbaud, R., Butler, I. B., Ellam, R. M., Rickard, D. and Oldroyd, A. (2011), 'Experimental determination of the equilibrium Fe isotope fractionation between Feaq2+ and FeSm (mackinawite) at 25 and 2°C, journal = Geochimica et Cosmochimica Acta', **75**(10), 2721–2734.
URL: *https://www.sciencedirect.com/science/article/pii/S0016703711001025*

Imhoff, J. F. (2005), *Enterobacteriales*, Springer US, Boston, MA, pp. 587–850.
URL: *https://doi.org/10.1007/0-387-28022-7*$_1$3

Johnson, D. C., Dean, D. R., Smith, A. D. and Johnson, M. K. (2005), 'STRUCTURE, FUNCTION, AND FORMATION OF BIOLOGICAL IRON-SULFUR CLUSTERS', *Annual Review of Biochemistry* **74**(1), 247–281. PMID: 15952888.
URL: *https://doi.org/10.1146/annurev.biochem.74.082803.133518*

Jørgensen, B. B., Böttcher, M. E., Lüschen, H., Neretin, L. N. and Volkov, I. I. (2004), 'Anaerobic methane oxidation and a deep H2S sink generate isotopically heavy sulfides in Black Sea sediments 1 1Associate editor: D. E. Canfield', *Geochimica et Cosmochimica Acta* **68**(9), 2095–2118.
URL: *https://www.sciencedirect.com/science/article/pii/S0016703703005660*

Knittel, K. and Boetius, A. (2009), 'Anaerobic Oxidation of Methane: Progress with an Unknown Process', *Annual Review of Microbiology* **63**(1), 311–334. PMID: 19575572.
URL: *https://doi.org/10.1146/annurev.micro.61.080706.093130*

Lin, Z., Sun, X., Peckmann, J., Lu, Y., Xu, L., Strauss, H., Gong, J., Lu, H. and Teichert, B. M. (2016b), 'The enrichment of heavy iron isotopes in authigenic pyrite as a possible indicator of sulfate-driven anaerobic oxidation of methane: Insights from the South China Sea', *Chemical Geology* **449**, 15–29.

Lin, Z., Sun, X., Peckmann, J., Lu, Y., Xu, L., Strauss, H., Gong, J., Lu, H. and Teichert, B. M. (2017), 'Multiple sulfur isotope constraints on sulfate-driven anaerobic oxidation of methane: Evidence from authigenic pyrite in seepage areas of the South China Sea', *Geochimica et Cosmochimica Acta* **211**, 153–173.

Lin, Z., Sun, X., Peckmann, J., Lu, Y., Xu, L., Strauss, H., Zhou, H., Gong, J., Lu, H. and Teichert, B. M. (2016a), 'How sulfate-driven anaerobic oxidation of methane affects the sulfur isotopic composition of pyrite: A SIMS study from the South China Sea', *Chemical Geology* **440**, 26–41.

Lonvaud-Funel, A. (2014), 'Leuconostocaceae Family', pp. 455–465.
URL: *https://www.sciencedirect.com/science/article/pii/B9780123847300001853*

Mandal (2018), 'Molecular mechanistic pathway of colorectal carcinogenesis associated with intestinal microbiota', *Anaerobe* **49**, 63–70.
URL: *https://www.sciencedirect.com/science/article/pii/S1075996417302317*

Ono, S., Keller, N. S., Rouxel, O. and Alt, J. C. (2012), 'Sulfur-33 constraints on the origin of secondary pyrite in altered oceanic basement', *Geochimica et Cosmochimica Acta* **87**, 323–340.

Ono, S., Shanks, W., Rouxel, O. and Rumble, D. (2007), 'S-33 constraints on the seawater sulfate contribution in modern seafloor hydrothermal vent sulfides', *Geochimica et Cosmochimica Acta* **71**, 1170–1182.

Palleroni, J. and Bradbury, J. F. (1993), Stenotrophomonas, a New Bacterial Genus for maltophilia (Hugh 1980) Swings et al. Xanthornonas 1983.

Pedersen, R., Rapp, H., Thorseth, I., Lilley, M., Barriga, F., Baumberger, T., Flesland, K., Fonseca, R., Früh-Green, G. and Jørgensen, S. (2010*a*), 'Discovery of a black smoker vent field and vent fauna at the Arctic Mid-Ocean Ridge', *Nature communications* **1**, 126.

Pedersen, R., Rapp, H., Thorseth, I., Lilley, M., Barriga, F., Baumberger, T., Flesland, K., Fonseca, R., Früh-Green, G. and Jørgensen, S. (2010*b*), 'Discovery of a black smoker vent field and vent fauna at the Arctic Mid-Ocean Ridge', *Nature communications* **1**, 126.

Peketi, A., Mazumdar, A., Joshi, R. K., Patil, D. J., Srinivas, P. L. and Dayal, A. M. (2012), 'Tracing the Paleo sulfate-methane transition zones and H2S seepage events in marine sediments: An application of C-S-Mo systematics', *Geochemistry, Geophysics, Geosystems* **13**.

Poulton, S. and Canfield, D. (2005), 'Development of a sequential extraction procedure for iron: Implications for iron partitioning in continentally derived particulates', *Chemical Geology* **214**, 209–221.

Raiswell, R. and Canfield, D. (1998), 'Sources of iron for pyrite formation in marine sediments', *American Journal of Science* **298**.

Rickard, D. (2012), *Sulfidic sediments and sedimentary rocks*, Newnes.

Sato, H., Hayashi, K. I., Ogawa, Y. and Kawamura, K. (2012), 'Geochemistry of deep sea sediments at cold seep sites in the Nankai Trough: Insights into the effect of anaerobic oxidation of methane', *Marine Geology* **323-325**, 47–55.

Schreiber, L., Holler, T., Knittel, K., Meyerdierks, A. and Amann, R. (2010), 'Identification of the dominant sulfate-reducing bacterial partner of anaerobic methanotrophs of the ANME-2 clade', *Environmental Microbiology* **12**(8), 2327–2340.

Severmann, S., Johnson, C. M., Beard, B. L. and McManus, J. (2006), 'The effect of early diagenesis on the Fe isotope compositions of porewaters and authigenic minerals in continental margin sediments', *Geochimica et Cosmochimica Acta* **70**(8), 2006–2022.
URL: *https://www.sciencedirect.com/science/article/pii/S0016703706000342*

Sievert, S., Kiene, R. and Schulz-Vogt, H. (2007), 'The Sulfur Cycle', *Oceanography* **20**.

Slotznick, S., Sperling, E., Tosca, N., Miller, A., Clayton, K., van Helmond, N., Slomp, C. and Swanson-Hysell, N. (2019), 'Unraveling the Mineralogical Complexity of Sediment Iron Speciation Using Sequential Extractions', *Geochemistry, Geophysics, Geosystems* **21**.

Stam, M. C. (2010), *Sulfur isotopes as a tracer for biogenic sulfate reduction in natural environments: a link between modern and ancient ecosystems*, [s.n.].

Steen, I. H., Dahle, H., Stokke, R., Roalkvam, I., Daae, F.-L., Rapp, H. T., Pedersen, R. B. and Thorseth, I. H. (2016), 'Novel Barite Chimneys at the Loki's Castle Vent Field Shed Light on Key Factors Shaping Microbial Communities and Functions in Hydrothermal Systems', *Frontiers in*

Microbiology **6**.
URL: *https://www.frontiersin.org/article/10.3389/fmicb.2015.01510*

Tarnovetskii, I. Y., Merkel, A. Y., Kanapatskiy, T. A., Ivanova, E. A., Gulin, M. B., Toshchakov, S. and Pimenov, N. V. (2018), 'Decoupling between sulfate reduction and the anaerobic oxidation of methane in the shallow methane seep of the Black sea', *FEMS Microbiology Letters* **365**(21). fny235.
URL: *https://doi.org/10.1093/femsle/fny235*

Teng, F.-Z., Dauphas, N. and Watkins, J. M. (2017), 'Non-Traditional Stable Isotopes: Retrospective and Prospective', *Reviews in Mineralogy and Geochemistry* **82**(1), 1–26.
URL: *https://doi.org/10.2138/rmg.2017.82.1*

Tiwari, M., Singh, A. K. and Sinha, D. K. (2015), 'Stable isotopes: Tools for understanding past climatic conditions and their applications in chemostratigraphy', *Chemostratigraphy: Concepts, Techniques, and Applications* pp. 65–92.

Turchyn, A. V., Sivan, O., Ono, S. and Bosak, T. (2018), *Microbial Connections Between the Subsurface Sulfur Cycle and Other Elemental Cycles*, Frontiers Media SA.
URL: *https://www.frontiersin.org/research-topics/3846/microbial-connections-between-the-subsurface-sulfur-cycle-and-other-elemental-cycles*

Viflot, T. (2019), Evidence for extensive conductive cooling and microbial carbon transformations in diffuse hydrothermal fluids from the Loki s Castle Vent Field.

Wei, H., Wei, X., Qiu, Z., Song, H. and Shi, G. (2016), 'Redox conditions across the G–L boundary in South China: Evidence from pyrite morphology and sulfur isotopic compositions', *Chemical Geology* **440**, 1–14.
URL: *https://www.sciencedirect.com/science/article/pii/S0009254116303394*

Wilkin, R., Barnes, H. and Brantley, S. (1996), 'The size distribution of framboidal pyrite in modern sediments: An indicator of redox conditions', *Geochimica et Cosmochimica Acta* **60**, 3897–3912.